

# Variability of Planetary Boundary Layer Winds

By

Lee Ray Hoxit

Project Leader

Wm. M. Gray

Department of Atmospheric Science  
Colorado State University  
Fort Collins, Colorado

NSF GA-32589X1



Department of  
Atmospheric Science

Paper No. 199

VARIABILITY OF PLANETARY BOUNDARY LAYER WINDS

by  
Lee Ray Hoxit

Preparation of this report  
has been financially supported by  
NSF Grant No. GA-32589X1

Principal Investigator: William M. Gray

Department of Atmospheric Science  
Colorado State University  
Fort Collins, Colorado  
May, 1973

Atmospheric Science Paper No. 199

## FOREWORD

The principal investigator has long had the conviction that there is much yet to be learned about the planetary boundary layer and that the answers to many of the physical processes occurring in this layer lie buried in the already collected upper-air soundings. If we would perform many statistical data stratifications much of our ignorance of the processes occurring in this layer might be overcome. Realistic numerical modeling could then more confidently proceed. The ready accessibility of upper air information on data tapes has recently made empirical studies of this type very feasible.

This paper represents the research portion of Lee R. Hoxit's Ph.D. thesis. It deals with the characteristics of the planetary boundary layer winds over the eastern half of the U. S. This paper represents part of a continuing observational boundary layer research effort on the author's research projects. Other observational studies have been accomplished over land, ocean, and at deep tropical latitudes. These include:

1. A statistical study of frictional wind veering in the planetary boundary layer---by Bruce R. Mendenhall (CSU Atm. Sci. Report No. 116).
2. A diagnostic study of the planetary boundary layer over the oceans---by William M. Gray (CSU Atm. Sci. Report No. 179).
3. Extensive data stratification of the boundary layer wind veering in tropical latitudes (research not yet completed). This study is finding that the amount of wind veering and its vertical distribution in the deep tropics is only slightly different from the veering occurring in middle latitudes.

The author hopes that other observational boundary layer studies can be made.

William M. Gray  
Colorado State University

## ABSTRACT

### VARIABILITY OF PLANETARY BOUNDARY LAYER WINDS

Systematic stratifications and analyses of low level radiosonde and rawindsonde data are performed for portions of the eastern half of the United States. These procedures are designed to specify the changes in the planetary boundary layer wind profile resulting from variations in baroclinicity, stability, and speed. The observed changes are used to develop an empirical model of the height distribution of the ageostrophic wind.

In baroclinic conditions the angle between the winds and isobars; the ageostrophic wind components; the surface stress and the surface wind speed are all shown to be functions of the orientation of the thermal wind vector relative to the surface geostrophic wind. These variations are consistent with a mixing length model of the additional turbulent momentum transport initiated by the vertical shear of the geostrophic wind.

Observed diurnal variations in the wind profiles for the lowest 2.5-3 km are associated with the typical diurnal variation in stability. For clear conditions, the data indicate that the depth of the Ekman or momentum boundary layer varies by an order of magnitude and an inertial boundary layer exist in the 200-1500 m layer during the night and morning hours. Inertial oscillations in the ageostrophic winds amplify the diurnal variations in the kinetic energy and kinetic energy generation. Only in the afternoon hours does a balance exist among pressure gradient, Coriolis and frictional forces.

Observed wind profiles are stratified according to the magnitude

of the observed speed in the lowest 100 mb ( $\approx 1$  km). The results indicate that the normalized ageostrophic wind components change significantly as the speed increases, especially in the layer 25-150 mb above the surface.

## TABLE OF CONTENTS

	Page
FOREWORD . . . . .	iii
ABSTRACT . . . . .	iv
LIST OF TABLES . . . . .	x
LIST OF FIGURES . . . . .	xiii
LIST OF SYMBOLS . . . . .	xx
1. INTRODUCTION . . . . .	1
1.1 Background . . . . .	1
1.2 Objective . . . . .	3
1.3 Methodology . . . . .	3
2. BASIC PROBLEMS AND CONCEPTS . . . . .	4
2.1 Baroclinic Effects . . . . .	4
Review . . . . .	4
Emphasis of the Present Study . . . . .	5
2.2 Stability Effects . . . . .	5
Review . . . . .	5
Emphasis of the Present Study . . . . .	7
2.3 Speed Effects . . . . .	7
Review . . . . .	7
Emphasis of the Present Study . . . . .	8
2.4 Vertical Motion in the Planetary Bound- ary Layer . . . . .	8
2.5 Working Hypothesis . . . . .	11
3. EXPERIMENT DESIGN AND ANALYSES PROCEDURES . . . . .	13
3.1 Data Sources . . . . .	13

TABLE OF CONTENTS (cont'd)

	Page
Wind Data for Specified Heights (Deck 545) . . . . .	13
Wind and Temperature Data for Specified Pressure Levels (Deck 645) . . . . .	15
3.2 Analyses and Computations . . . . .	18
Vertical Coordinates . . . . .	18
Computation of External Parameters . . . . .	19
Computation of Dependent Parameters . . . . .	24
3.3 Data Stratifications . . . . .	29
Stratification A . . . . .	29
Stratification B . . . . .	31
Stratification C . . . . .	33
Stratification D . . . . .	34
3.4 Analysis of Variance . . . . .	34
Observational Errors . . . . .	35
Local Variations . . . . .	35
Topographical Effects . . . . .	36
Vertical Resolution of Wind Data . . . . .	36
Variability Caused by External Factors . . . . .	37
4. PLANETARY BOUNDARY LAYER WINDS IN BAROCLINIC CONDITIONS . . . . .	40
4.1 Direct Effects of Geostrophic Shear . . . . .	40
4.2 Indirect Effects of Geostrophic Shear . . . . .	43
Variation of Wind Veering . . . . .	43
Variations in Ageostrophic Winds . . . . .	48
Variations in Surface Stress . . . . .	54
Variations in Surface Speed . . . . .	56
Interpretation of Results . . . . .	59
4.3 The Role of Geostrophic Shear in Selected Atmospheric Processes . . . . .	63
Movement of Cold Air Masses . . . . .	63
Transport of Angular Momentum . . . . .	65

TABLE OF CONTENTS (cont'd)

	Page
4.4 Conclusions . . . . .	67
5. EFFECTS OF STABILITY ON PLANETARY BOUNDARY LAYER WIND PROFILES . . . . .	69
5.1 General Effects of Stability . . . . .	69
Variations in Wind Veering . . . . .	69
Variations in Ageostrophic Winds . . . . .	83
5.2 Diurnal Variations. . . . .	87
Variations in Wind Veering . . . . .	87
Variations in Wind Speed. . . . .	88
Diurnal Variations Over the Ocean . . . . .	94
Qualitative Model of Diurnal Wind Variations . . . . .	95
5.3 Conclusions . . . . .	102
6. VARIATIONS IN THE KINETIC ENERGY BALANCE OF THE PLANETARY BOUNDARY LAYER RELATED TO CHANGES IN STABILITY . . . . .	104
6.1 Kinetic Energy Generation Over the U. S. Network . . . . .	104
Method of Computation . . . . .	104
Results . . . . .	105
6.2 Diurnal Variations in the Kinetic Energy Budget . . . . .	108
Method of Computation . . . . .	108
Results . . . . .	112
6.3 Conclusions . . . . .	116
7. EFFECTS OF SPEED ON THE PLANETARY BOUND- ARY LAYER WIND PROFILE. . . . .	117
7.1 Previous Results . . . . .	117

## TABLE OF CONTENTS (cont'd)

	Page
7.2 Significance of the Speed Parameter (S). . .	119
Variations in Wind Veering . . . . .	119
Variations in Ageostrophic Winds. . . . .	120
7.3 Conclusions . . . . .	127
8. EMPIRICAL MODEL OF AGEOSTROPHIC WINDS . . .	128
8.1 Standard Profiles . . . . .	128
8.2 Variations Related to Baroclinicity . . . .	131
8.3 Variations Related to Stability. . . . .	135
General Variations . . . . .	135
Diurnal Variations . . . . .	137
8.4 Variations Related to Speed Changes. . . .	142
8.5 Method for Computing Vertical Motion . . .	145
9. SUMMARY . . . . .	148
9.1 Review . . . . .	148
9.2 Results and Conclusions . . . . .	148
Role of Baroclinicity . . . . .	148
Role of Stability Changes. . . . .	149
Role of Speed Variations. . . . .	150
9.3 Extension of the Present Work . . . . .	151
ACKNOWLEDGEMENTS	
BIBLIOGRAPHY . . . . .	153

## LIST OF TABLES

Table No.	Caption	Page
3.1	Stations included in the specified height wind analyses. . . . .	14
3.2	Stations included in the U. S. network. . . . .	17
3.3	Period of record included in the network analyses . . . . .	18
3.4	Standard deviations (degrees) of the observed wind veering. . . . .	35
3.5	Standard deviations (degrees) for selected categories from Stratification B. (See Section 3.3 for a description of the categories.) . . . . .	39
4.1	Combinations of categories from Stratifications A and B which were used to obtain the values shown in Figs. 4.2 - 4.5, and Figs. 4.7 - 4.10. The number of observations is given for each combination. In obtaining average values for each thermal wind category, the combinations were weighted equally. (See Section 3.3 for a description of the categories.) . . . . .	42
4.2	Average values of $ \vec{V}_T /S$ during the winter season for the nine thermal wind categories. . . . .	44
4.3	Average values of the geostrophic wind speed, and the normalized ageostrophic wind components for eight categories of $\psi$ (or $\beta$ ) and for conditions with negligible thermal winds. Time 00Z. . . . .	51
4.4	Average values of the geostrophic wind speed, and the normalized ageostrophic wind components for eight categories of $\psi$ (or $\beta$ ) and for conditions with negligible thermal winds. Time 12Z. . . . .	52

LIST OF TABLES (cont'd)

Table No.	Caption	Page
4.5	Average values of the surface stress and components of surface stress for 00Z. Included are ratios of the stress values to the average surface geostrophic wind speed. . . . .	57
4.6	Average values of $ \vec{V}_o $ and $ \vec{V}_o  /  \vec{V}_g $ for the nine thermal wind categories. . . . .	58
5.1	Combinations of categories from Stratification B which were used to obtain the values shown in Fig. 5.1. The number of observations is given for each combination. In obtaining average values for each stability category the combinations were weighted equally. (See Section 3.3 for a description of the categories.) . . . . .	71
5.2	Lapse rate combinations from Stratification C which were included in the indicated stability classes. The numbers refer to the lapse rate categories defined in Section 3.3. . . . .	84
5.3	Average normalized ageostrophic wind components at 00Z for three stability classes. . . . .	85
5.4	Average normalized ageostrophic wind components at 12Z for three stability classes. . . . .	85
6.1	Average kinetic energy generation (watts/m <sup>2</sup> ) for the area covered by the 19 interior stations of the U. S. network. . . . .	106
6.2	Average kinetic energy generation (watts/m <sup>2</sup> ) for the Northern Hemisphere as given by Kung (1969). . . . .	107
7.1	Variation of the angle between the surface wind and isobars with speed. Taken from Dobson (1914). . . . .	117

LIST OF TABLES (cont'd)

Table No.	Caption	Page
7.2	List of categories and number of observations in each category (from Stratification B) which are included in the speed analysis (See Section 3.3 for a description of the categories). . . . .	121
7.3	Average values of the geostrophic wind speed, and the normalized ageostrophic wind components at 00Z, for four wind speed categories. . . . .	123
7.4	Average values of the geostrophic wind speed and the normalized ageostrophic wind components at 12Z for four wind speed categories. . . . .	124
8.1	Average conditions associated with the observed deviation shown in Fig. 8.2. . . . .	133

## LIST OF FIGURES

Figure No.	Caption	Page
3.1	Radiosonde Network. Data from stations outside the shaded area were utilized only to calculate the horizontal derivatives of temperature for the 19 interior stations. The superimposed $2^{\circ}$ latitude - $2^{\circ}$ longitude grid was used in all horizontal analyses. . . . .	16
3.2	Eight layer model used in the analyses of wind data for those stations given in Table 3.1. The asterisks indicate elevations above the surface. . . . .	20
3.3	Six layer model used in the network analyses. . . . .	20
3.4	Schematic diagram illustrating the method used to compute the wind shear between levels $l$ and $l + 1$ . (a) Wind vectors and components in the meteorological coordinate system. (b) Wind vectors and components in the natural coordinate system. (c) Wind vectors and components of the wind shear in the natural coordinate system. . . . .	27
3.5	Illustration of procedures employed in constructing hodographs. . . . .	29
3.6	Illustration of how the components of the ageostrophic wind were obtained. . . . .	32
4.1	Schematic diagram defining the angle $\psi$ . . . . .	41
4.2	Comparison of the average veering angles prior to and after the elimination of the geostrophic veering. The angle $\psi$ is measured clockwise from the direction of the wind 100 mb above the surface to the direction of the mean thermal wind in the lowest 100 mb. . . . .	45
4.3	Angle between wind and isobars versus height at 00Z for the nine thermal wind categories. The geostrophic veering has	

LIST OF FIGURES (cont'd)

Figure No.	Caption	Page
	been eliminated from the data. The angle $\psi$ is measured clockwise from the direction of the wind 100 mb above the surface to the direction of the thermal wind vector for the lowest 100 mb. . . . .	46
4.4	Angle between wind and isobars versus height at 12Z for nine thermal wind categories. The geostrophic veering has been eliminated from the data. The angle $\psi$ is measured clockwise from the direction of the wind 100 mb above the surface to the direction of the thermal wind vector for the lowest 100 mb. . . . .	47
4.5	Angle between the surface wind and surface isobars as a function of the angle between the wind vector 100 mb above the surface and the thermal wind vector in the lowest 100 mb. . . . .	49
4.6	Schematic diagram defining the angle $\beta$ . . . . .	49
4.7	Angle between the surface wind and surface isobars as a function of the angle between the surface isobars and the thermal wind. . . . .	50
4.8	Comparison of the normalized ageostrophic wind components for cases of warm and cold air advection. . . . .	53
4.9	Normalized values of the surface stress at 00Z as a function of the angle between the surface geostrophic wind and the thermal wind in the lowest 100 mb. The units are in $(\text{dynes/cm}^2) / (\text{m/sec})$ . . . . .	59
4.10	Normalized values of the surface wind speed as a function of the angle between the surface geostrophic wind and the thermal wind in the lowest 100 mb. . . . .	60

LIST OF FIGURES (cont'd)

Figure No.	Caption	Page
4.11	Schematic examples of how the additional downward momentum transport, resulting from geostrophic shear in the turbulent boundary layer, modifies the surface veering angle from that expected in a barotropic atmosphere. ( $\vec{V}_O(B)$ is the surface wind which would exist in barotropic conditions; $\Delta\vec{V}_g$ represents the geostrophic shear vector in the lowest kilometer; $\vec{V}_O$ is the actual surface wind; $\vec{V}_{gO}$ is the surface geostrophic wind; $\vec{V}_g(1km)$ is the geostrophic wind at one kilometer; and $\alpha_O$ is the angle between the surface wind and surface geostrophic wind.) . . . . .	61
4.12	Surface analysis showing the modification of the angle between the surface winds and surface isobars. Surface pressure in millibars (only the last two digits are plotted) is given by the solid lines. The temperature field ( $^{\circ}F$ ) is given by the dashed lines. The observed winds are plotted for each station. In the stippled area behind the cold front the average value of $\alpha_O$ is $60^{\circ}$ . In the stippled area ahead of the cold front the average value of $\alpha_O$ is $33^{\circ}$ . . . . .	64
4.13	Schematic example showing how the downward momentum transport by the geostrophic shear can systematically increase the westerly component of the surface winds. . . . .	66
5.1	Angle between wind and isobars versus height for three stability categories. . . . .	70
5.2	Veering angle as a function of height for various lapse rate profiles. Time-00Z; Season-Winter. . . . .	73
5.3	Veering angle as a function of height for various lapse rate profiles. Time-12Z; Season-Winter. . . . .	77

LIST OF FIGURES (cont'd)

Figure No.	Caption	Page
5.4	Veering angle as a function of height for various lapse rate profiles. Time-00Z; Season-Summer. . . . .	80
5.5	Veering angle as a function of height for various lapse rate profiles. Time-12Z; Season-Summer. . . . .	81
5.6	Comparison of the normalized ageostrophic wind component for very stable and near adiabatic conditions during the winter season. . . . .	86
5.7	Diurnal variation of the angle between the surface wind and surface isobars. Values based on data from Jackson, Mississippi; Shreveport, Louisiana; and Montgomery, Alabama. . . . .	88
5.8	Diurnal variation of the angle between wind and isobars as a function of height. Values based on data from Jackson, Mississippi; Shreveport, Louisiana; and Montgomery, Alabama. Season-Winter. Times are in Local Time. . . . .	89
5.9	Same as Fig. 5.8. Season-Spring. . . . .	90
5.10	Same as Fig. 5.8. Season-Summer. . . . .	91
5.11	Same as Fig. 5.8. Season-Fall. . . . .	92
5.12	Diurnal variation of the wind speed as a function of height. Values are based on data from Jackson, Mississippi; Shreveport, Louisiana; and Montgomery, Alabama. Times are given in Local Time. . . . .	93
5.13	Diurnal variation of the angle between wind and isobars as a function of height for Weather Ship E (35°N, 48°W). Annual average. Times are given in Local Time. . . . .	96

## LIST OF FIGURES (cont'd)

Figure No.	Caption	Page
5.14	Diurnal variation of wind speed as a function of height for Weather Ship E (35°N, 48°W). Annual average. Times are given in Local Time. . . . .	97
5.15	Schematic profiles illustrating the typical diurnal variation in the potential temperature profile for the lowest 2500 m under basically clear sky conditions. . . . .	99
5.16	Schematic diagram of the diurnal variation in the depths of the momentum and inertial boundary layers. Together these layers make up the planetary boundary layer. . . . .	99
5.17	Schematic diagram showing the change of ageostrophic wind components in the inertial boundary layer. Time of formation assumed to be 1900 LT. Latitude $\approx 35^{\circ}\text{N}$ . . . . .	100
5.18	Comparison of the 00Z (1800 LT) and 12Z (0600 LT) veering profiles for conditions with same lapse rate profiles. . . . .	100
6.1	Average cross-isobaric wind component for the 19 interior stations in the U. S. network. . . . .	106
6.2	Average diurnal variation in the kinetic energy per unit mass for Shreveport, Louisiana. Season-Winter. . . . .	110
6.3	Same as Fig. 6.2. Season-Summer. . . . .	111
6.4	Diurnal variations of kinetic energy generation; kinetic energy dissipation; and change in kinetic energy for the lowest 2.5 km of the atmosphere. Seasons - Winter and Spring. . . . .	113

LIST OF FIGURES (cont'd)

Figure No.	Caption	Page
6.5	Same as Fig. 6.4. Seasons-Summer and Fall. . . . .	114
7.1	Latitude distribution of the angle between the surface wind and isobars over the oceans for four categories of surface wind speed (taken from Gray, 1972). The averages were obtained by combining all available rawinsonde and pibal data for the period 1949-1964. . . . .	118
7.2	Angle between surface wind and isobars as a function of the surface Rossby number. (Taken from Blackadar (1962)). The source of the various observations included Bernstein (1959), Dobson (1914), Jeffries (1920), Lettau (1950, 1957), Sheppard and Omar (1952) and Blackadar. . . . .	119
7.3	Angle between the surface wind and isobars as a function of the average speed in the lowest 100 mb. . . . .	120
7.4	Angle between wind and isobars as a function of height for the four categories of average speed in the lowest 100 mb. . . . .	122
7.5	Comparison of the normalized ageostrophic wind components for conditions of weak and strong winds in the lowest 100 mb. . . . .	125
7.6	Profiles of the average ageostrophic wind component towards lower pressure for four categories of average speed in the lowest 100 mb. . . . .	126
8.1	Observed and model profiles of the normalized ageostrophic flow. The profiles are for barotropic conditions; uniform lapse rate of 5°C/km in the lowest kilometer; and an average speed in the lowest kilometer of 10 m/sec. . . . .	129

LIST OF FIGURES (cont'd)

Figure No.	Caption	Page
8.2	Observed deviations of the normalized ageostrophic wind components related to baroclinicity. . . . .	132
8.3	Model profiles of the deviations of the normalized ageostrophic wind components due to baroclinicity. . . . .	135
8.4	Observed deviations of the normalized ageostrophic wind components related to variations in the stability of the lowest 1500 m. . . . .	138
8.5	Model profiles of the deviations in the normalized ageostrophic wind components due to stability variations. . . . .	138
8.6	Observed deviations of the normalized ageostrophic wind component attributed to inertial oscillations. The profiles are the difference between the 00Z values and 12Z values (00Z minus 12Z) for the same existing lapse rates. . . . .	139
8.7	Schematic diagram showing the ratio of the component amplitudes to their maximum amplitudes for inertial motion at 35°N. . . . .	140
8.8	Model profiles of the deviations in the normalized ageostrophic wind components arising from the formation of an inertial boundary layer at 1900 LT. . . . .	143
8.9	Observed deviations in the normalized ageostrophic wind components related to variations in the average speed in the lowest kilometer. . . . .	143
8.10	Model profiles of the deviation in normalized ageostrophic wind components related to variations in the average speed in the lowest kilometer. . . . .	144

## LIST OF SYMBOLS

### GEOMETRIC VARIABLES

#### Lengths

- n Horizontal axis of a natural coordinate system
- s Horizontal axis of a natural coordinate system
- x Distance in the east-west direction (positive to the east)
- y Distance in the north-south direction (positive to the north)
- z Distance in the vertical (positive upward)

#### Angles

- $\alpha_T$  Angle between the wind direction at the top level and the wind direction at some level below (positive for wind veering with height)
- $\alpha$  Angle between the wind vector and isobars (positive for flow towards lower pressure)
- $\alpha_O$  Angle between the surface wind vector and surface isobars (positive for flow towards lower pressure)
- $\alpha'$  Angle between the wind vector 100 mb above the surface and the surface wind vector
- $\alpha''$  Angle between the wind vector 100 mb above the surface and the surface geostrophic wind
- $\beta$  Angle measured clockwise from the direction of the surface geostrophic wind to the direction of the mean thermal wind in the lowest 100 mb
- $\gamma$  Direction from which wind is blowing ( $0^\circ$ =North wind with values increasing clockwise)
- $\psi$  Angle measured clockwise from the direction of the wind 100 mb above the surface to the direction of the mean thermal wind in the lowest 100 mb

## LIST OF SYMBOLS (cont'd)

### DYNAMIC VARIABLES

#### Winds

$S$	Average speed in the lowest 100 mb
$\vec{V}$	Wind vector
$\vec{V}_o$	Surface wind vector
$\vec{V}_o(B)$	Surface wind vector for barotropic conditions
$\vec{V}_g$	Geostrophic wind vector
$\vec{V}_{g_o}$	Surface geostrophic wind vector
$\vec{V}_T$	Thermal wind in the lowest 100 mb
$\vec{V}''$	Ageostrophic wind vector
$\Delta\vec{V}_g$	Shear of the geostrophic wind

#### Wind Components

##### (1) Meteorological Coordinates

$u$	East-West wind component (west wind positive)
$u_g$	Component of the geostrophic wind in the East-West direction (west wind positive)
$u_{ag}$	Component of the ageostrophic wind in the East-West direction (west wind positive)
$v$	North-South wind component (south wind positive)
$v_g$	Component of the geostrophic wind in the North-South direction (south wind positive)
$v_{ag}$	Component of the ageostrophic wind in the North-South direction (south wind positive)
$w$	Vertical wind component in height reference frame

## LIST OF SYMBOLS (cont'd)

$\omega$  Vertical velocity in a pressure reference frame

### (2) Natural Coordinates

(a) Positive  $s$  axis oriented along the observed wind vector at the lower of two defined levels.

$u'$  Component of the observed wind along the positive  $s$  axis

$v'$  Component of the observed wind along the positive  $n$  axis

$\Delta u'_{\text{T}}$  Component of the observed wind shear along the positive  $s$  axis

$\Delta v'_{\text{T}}$  Component of the observed wind shear along the positive  $n$  axis

$\Delta u'_{\text{g}}$  Component of the geostrophic shear along the positive  $s$  axis

$\Delta v'_{\text{g}}$  Component of the geostrophic shear along the positive  $n$  axis

$\Delta u'$  Component of the wind shear along the positive  $s$  axis after the geostrophic shear is eliminated from the observed shear

$\Delta v'$  Component of the wind shear along the positive  $n$  axis after the geostrophic shear is eliminated from the observed shear

(b) Positive  $s$  axis oriented along the geostrophic wind vector

$u''$  The ageostrophic component of the wind parallel to the geostrophic wind (positive when the wind component along the isobar is less than the geostrophic wind speed)

$v''$  The ageostrophic component of the wind perpendicular to the geostrophic wind (positive for flow towards lower pressure)

(c) Positive  $s$  axis oriented along the surface geostrophic wind vector

$u_s$  Component of the wind parallel to the surface geostrophic wind (positive if in the same direction as the geostrophic wind)

$u_{sg}$  Component of the geostrophic wind parallel to the surface geostrophic wind

$v_n$  Component of the wind normal to the surface geostrophic wind (positive for flow towards lower pressure)

$v_{ng}$  Component of the geostrophic wind normal to the surface geostrophic wind

#### Stress Components

$\tau_{zs}$  Stress component along the  $s$  direction

$\tau_{zn}$  Stress component along the  $n$  direction

$\tau_{zs_0}$  Surface stress component along the  $s$  direction

$\tau_{zn_0}$  Surface stress component along the  $n$  direction

$\vec{\tau}_{z_0}$  Surface stress produced by momentum transfer in the  $z$  direction

#### Others

$C_d$  Drag coefficient

$f$  Coriolis parameter =  $(2 \Omega \sin \phi)$  where  $\Omega$  is the angular velocity of the earth and  $\phi$  is the latitude

$K_m$  Coefficient of eddy diffusivity

$z_0$  The surface roughness parameter

$\epsilon$  Kinetic energy dissipation per unit mass

#### THERMODYNAMIC VARIABLES

$p$  Pressure

LIST OF SYMBOLS (cont'd)

$p_o$	Surface pressure
$T$	Temperature
$T_o$	Surface temperature
$\Delta T_o$	$T_o(1500 \text{ LT}) - T_o(2100 \text{ LT})$ ( $^{\circ}\text{C}$ )
$\Gamma$	Lapse rate ( $^{\circ}\text{C}/100 \text{ mb}$ )
$\bar{\Gamma}$	Average lapse rate in the lowest 100 mb ( $^{\circ}\text{C}/100 \text{ mb}$ )
$\theta$	Potential temperature
$\theta_o$	Potential temperature at the surface
$\Delta\theta$	$\theta_{2000\text{m}} - \theta_o$ ( $^{\circ}\text{C}$ )
$\rho$	Density

CONSTANTS

$g$	Acceleration due to gravity
$R$	Gas constant for dry air
$A$	} Empirically derived amplitudes
$B$	
$A_T$	} Empirically derived amplitudes for the deviations of the ageostrophic wind component perpendicular to the isobars. The subscripts refer to thermal wind deviations (T); general stability deviations (S); diurnal deviations (D); and speed deviations (V)
$A_S$	
$A_D$	
$A_V$	

LIST OF SYMBOLS (cont'd)

$B_T$	}	Empirically derived amplitudes for the deviations of the ageostrophic wind components along the isobars
$B_S$		
$B_D$		
$B_V$		
a	}	Empirical constants (symbols used repeatedly to express the general form of equations)
b		
c		
d		
e		
m		
$\pi$		The number Pi -3.14159...

MISCELLANEOUS

KE	Kinetic energy
LT	Local time
$R_o$	Surface Rossby number
t	Time
t'	Elapsed time after formation of inertial boundary layer
Z	Symbol for Greenwich Meridian Time



## 1. INTRODUCTION

### 1.1 Background

The planetary boundary layer (PBL) is here defined as that portion of the atmosphere in which the wind deviates from gradient or geostrophic flow as a result of the retarding influence of surface friction. This layer plays a vital role in the exchange of momentum, sensible heat and water vapor between the earth's surface and the "free" atmosphere above. Recent computations by Kung (1969) suggest that about 40 percent of the kinetic energy generation and dissipation in the earth's atmosphere occurs in the PBL. Friction induced vertical motions provide the triggering mechanism for both large scale and meso-scale vertical exchange processes between the PBL and the atmosphere above.

Though meteorologists know in general that the processes mentioned above exist, adequate descriptions and explanations of the actual cause and effect relationships are not known in many instances. This lack of knowledge is due to the extreme complexity of the PBL. This layer, more than any other region of the atmosphere, is characterized by motions and physical processes with many different scales, and a continuous interaction between these scales. Yet, a description and understanding of the processes in the PBL will be necessary before physically complete models can become a reality.

Even if the problem is restricted to specifying the mean PBL wind profiles in terms of observed meteorological parameters, present knowledge is incomplete--both in terms of a description of the variations expected and the cause of the variations.

The pioneering efforts of Ekman (1905), Åckerblom (1908), and Taylor (1915) formulated mathematically the general spiral characteristics of the PBL wind profile. However, these models were based on several simplifying assumptions including barotropic, steady-state, homogeneous flow over uniform terrain, neutral temperature stratification, and an eddy diffusivity constant with height.

In the mid-latitudes, the synoptic scale systems give rise to large space and time variations in the baroclinicity, stability, speed and horizontal accelerations. This is especially true during the winter season over land areas. Under these conditions, the profile of the mean wind in the PBL cannot be adequately modeled by Ekman type theory or by strict use of similarity concepts. One or more of the assumptions which lead to the simplified theories are invalid in a majority of situations. This is especially true when there exist strong and rapidly moving synoptic scale pressure systems, or when the vertical exchange processes are inhibited as in the case of low level temperature inversions. If accurate models of the PBL wind profiles are to be developed for these conditions, they must be based on less restrictive assumptions.

## 1.2 Objective

The objective of this study is to obtain a description of the variations in the PBL wind profile due to changes in baroclinicity, stability, and magnitude of flow. Once the variability associated with each factor is determined, an empirical model is developed to specify the ageostrophic winds and the mean vertical motions in the PBL under a wide range of atmospheric conditions.

## 1.3 Methodology

The objectives of the study are sought utilizing the inductive approach. Parameters are selected to define the variation in each of three external factors--baroclinicity, stability, and magnitude of flow. Large quantities of operational radiosonde and windsonde data, available on magnetic tape, are processed to obtain sufficient data samples for all combinations of these parameters. Data defining the characteristics of the mean wind profile are then categorized according to the values of the external parameters. Interpretations and conclusions concerning physical processes are based on the results of these data stratifications.

## 2. BASIC PROBLEMS AND CONCEPTS

This chapter presents a brief review of the fundamental findings of previous investigators with regard to the effects of baroclinicity, stability and speed variations on the PBL wind profiles. The emphasis of the present study is outlined. Next, the importance of vertical motions in the PBL is demonstrated. It is argued that the difficulty in specifying these vertical motions arises from the lack of a realistic model of the ageostrophic winds in the lower atmosphere. Finally, the sequence of events which produce a change in the PBL wind profile is outlined. The working hypothesis (that valid cause and effect relationships can be obtained without defining the intermediate processes in this sequence) is discussed.

### 2.1 Baroclinic Effects

Review. The modification of the basic Ekman spiral in baroclinic conditions has been realized by numerous investigators. Several of these including Blackadar (1965), Ching (1964), Kovetz et al. (1963), Lettau (1967), Cattle (1971), Ellison (1956), MacKay (1971), Utina (1962) and Zaitsev (1966) have modified the theory of the basic Ekman spiral to include baroclinic effects. Bernstein (1959), Mendenhall (1967), Utina (1966) and Gray (1972) have investigated the effects of baroclinicity on observed wind veering profiles. The thermal wind relationship indicates that the magnitude of the modification depends on the relative magnitude of the temperature gradient while the sign depends on the orientation of this gradient relative to the surface isobars.

Basically, the thermal wind reduces the observed wind veering in cases of cold air advection and increases the observed veering in cases of warm air advection.

Emphasis of the Present Study. A second and potentially more important effect in baroclinic flow has been suggested by Sheppard et al. (1952). The baroclinicity modifies the vertical shears of the horizontal winds in the PBL. This in turn modifies the turbulent transports of momentum and the stress profiles.

The present study examines in detail the effects of this modified momentum transport on the PBL winds. Specifically, we seek to define the variations in the wind profiles from those expected in barotropic conditions. It is postulated that the momentum transport due to the geostrophic shear (like the change in the pressure gradient with height) is a linear function of the magnitude of the thermal wind, and is dependent on the orientation of the thermal wind relative to the low level winds.

In this study, the direct thermal wind effects (change of pressure gradient with height) are subtracted from the observed data. The remaining dependence of the wind profiles on the magnitude and orientation of the thermal wind is attributed to the momentum transport initiated by the geostrophic shear.

## 2.2 Stability Effects

Review. The amount of mixing or momentum transfer in the boundary layer is also dependent on the thermal stratification. In a stable

atmosphere mixing due to buoyancy is not present. Moreover, the vertical mixing due to mechanical turbulence is suppressed. Thus, the height at which the stress becomes negligible is reduced while the vertical gradient of the stress is increased. The opposite conditions exist in an unstable atmosphere, with buoyant air parcels providing a second mechanism for vertical momentum transfer. Recent numerical studies by Deardorff (1972), indicate that in unstable conditions, eddies produced by buoyancy becomes the dominant mixing mechanism in all but the surface layers. Stronger vertical mixing increases the depth of the boundary layer but weakens the vertical stress gradient.

The variation of the PBL wind profile for different thermal stratifications has been treated observationally by Mendenhall (1967) and Clark (1970) for land areas and by Gordan (1952), Findlater et al. (1966), Mendenhall (1967) and Cattle (1971) for ocean areas. Theoretical or modeling studies have been conducted by Kurosaki (1968) and Yamamoto et al. (1968). All these studies suggest that the angle between the surface wind and surface isobars increases with increasing stability while the depth of the Ekman layer decreases.

An additional problem exists when the thermal stratification changes rapidly with time. Most obvious is the diurnal heating and cooling, typically giving rise to adiabatic lapse rates in mid-afternoon and temperature inversions at night in the lowest few hundred meters. This provides a mechanism for oscillatory changes in the PBL wind

profile even when the synoptic flow is steady-state. Blackadar (1957) and Blackadar and Buajitti (1957) have developed theoretical models of the diurnal oscillation in winds above the first few hundred meters. They suggest that the oscillations in the ageostrophic winds in the 300-1500 m region are inertial oscillations resulting from the change of eddy viscosity with stability.

The special case of diurnal variations over a sloping terrain has been examined by numerous investigators. These include Lettau (1964, 1967), Holton (1967), Hsueh (1970), Sangster (1967), Jehn and Durie (1963) and Bonner and Paegle (1970). In the Great Plains region, the terrain slopes downward to the east and often gives rise to a day-night reversal in the direction of the thermal wind. This amplifies the general oscillation due to stability changes producing what is termed the "low level jet" during the night hours.

Emphasis of the Present Study. Observational data are selectively stratified in an attempt to confirm the fundamental stability relationships outlined above. In addition, an analysis of the diurnal wind variations is performed to determine the impact of inertial motions on the wind profiles and energy budgets.

### 2.3 Speed Effects

Review. The dependence of the wind profile on the intensity of the flow and on the surface roughness has been demonstrated by Blackadar (1962). His results indicate that the angle between the surface wind and isobars ( $\alpha_0$ ) is inversely proportional to the surface Rossby

number ( $R_o$ ).

$$\alpha_o \propto 1/R_o \propto fz_o / |\vec{V}_{g_o}|$$

Here  $\vec{V}_{g_o}$  is the surface geostrophic wind and  $z_o$  is the surface roughness. This relationship suggests that the value of  $\alpha_o$  increases with increasing roughness, but decreases with increasing values of  $|\vec{V}_{g_o}|$ . Numerous observations have confirmed the first statement. However, Dobson (1914) and recently Gray (1972) found the value of  $\alpha_o$  to increase with increasing speed.

Emphasis of the Present Study. The previous studies have looked only at the dependence of the surface crossing angle on wind speed. The ageostrophic wind vector is, however, the fundamental parameter. For purposes of comparison the dependence of both the wind veering profiles and ageostrophic wind profiles on speed variations will be investigated. We expect that conclusions made from wind veering data about the values of the ageostrophic winds are sometimes invalid.

#### 2.4 Vertical Motion in the Planetary Boundary Layer

One of the critical problems facing atmospheric scientists today is the development of a realistic model of the mean vertical motion in the PBL. Indeed, Charnock and Ellison (1967) suggest that specifying the mean vertical motion at the top of the PBL may be the most crucial problem facing GARP (Global Atmospheric Research Program). For the idealized conditions of barotropic, steady state, horizontally

homogeneous flow where the veering angles and depth of the PBL do not vary horizontally, Charney and Eliassen (1949) showed that the vertical motion was simply proportional to the low level vorticity. Gray (1968) and Williams (1970) found strong correlations between the existence of positive low level vorticity and the formation and maintenance of tropical storms and cloud clusters. The CISK (Conditional Instability of the Second Kind) mechanism of hurricane formation as proposed by Ooyama (1964) and Charney and Eliassen (1964) stresses the importance of upward motion induced by friction.

In mid-latitudes, the high correlation between positive low level vorticity and areas of precipitation again suggest that friction induced vertical motions are a vital part of the exchange processes in synoptic scale systems.

The general expression for computing vertical motion in the atmosphere is the equation of continuity, defining the law of conservation of mass. In pressure coordinates, for a hydrostatic atmosphere, this equation is written as:

$$\frac{\partial \omega}{\partial p} = - \left( \frac{\partial u}{\partial x} + \frac{\partial v}{\partial y} \right) \quad (2.1)$$

where  $\omega$  is the vertical velocity and  $u$  and  $v$  are the wind components in the east-west and north-south directions respectively. The vertical motion is then defined by the height distribution of the

horizontal divergence. In general, the total wind is made up of a geostrophic component and an ageostrophic component:

$$u = u_g + u_{ag} \quad (2.2)$$

$$v = v_g + v_{ag} \quad (2.3)$$

where

$$u_g = -g/f \partial z / \partial y \quad (2.4)$$

$$v_g = g/f \partial z / \partial x \quad (2.5)$$

Substituting Eqs. (2.2 - 2.5) in Eq. (2.1), and making use of the chain rule, the expression becomes:

$$\frac{\partial \omega}{\partial p} = - \left( \frac{\partial u_{ag}}{\partial x} + \frac{\partial v_{ag}}{\partial y} \right) - \frac{v_g}{f} \frac{\partial f}{\partial y} \quad (2.6)$$

Equation (2.6) demonstrates the well known fact that the divergence of the geostrophic wind is non-zero only through the variation of the Coriolis parameter with latitude. If  $v_g = 10$  m/sec at  $45^\circ\text{N}$ , the divergence is  $2 \times 10^{-6} \text{sec}^{-1}$ . If this divergence value existed in the lower 1 km of the atmosphere the resulting upward vertical motion at the 1 km level is 0.2 cm/sec. This is an order of magnitude smaller than the maximum vertical motion values at 1 km associated with mid-latitude synoptic disturbances. In most conditions, the major

contribution to the horizontal divergence in the PBL is the horizontal variation of the ageostrophic wind components.

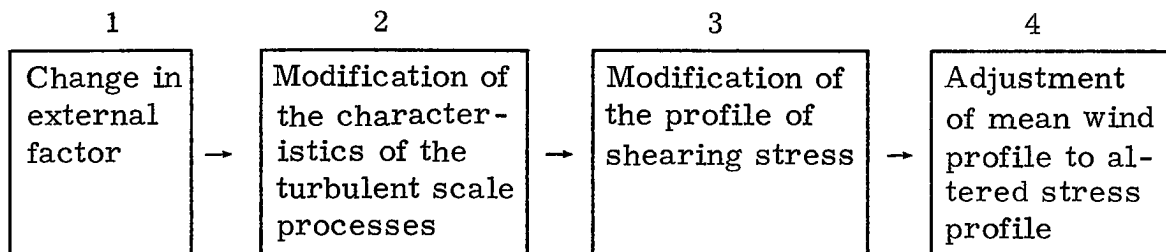
As was shown in the previous sections, the distribution of the ageostrophic wind in the lower atmosphere may be modified by variations in the following factors (referred to in this paper as external factors):

- (1) baroclinicity
- (2) stability
- (3) speed .

To date however, the quantitative aspects of these modifications have not been adequately defined. Rigorous theories exist only for simplified conditions. Most observational studies have tended to look only at the directional changes in the winds and have not considered the total ageostrophic wind vector. In addition, usually only one of the external factors are specified, leaving the remaining factors to possibly bias the results. As a result, a general model of the height distribution of the ageostrophic wind in the PBL does not exist. Until such a model is available, the limitations of assuming the vertical motion to be specified by the low level vorticity cannot be determined.

### 2.5 Working Hypothesis

The sequence of events which occurs due to changes in one or more of the external factors is visualized as follows:



The details of the processes in steps 2 and 3 cannot be defined explicitly due to the closure problems in classical turbulence theory. In seeking alternative methods, it is hypothesized that a model of the role of the external factors can be obtained by ignoring steps 2 and 3, thereby looking only for cause and effect relationships between steps 1 and 4. In this type of approach, the physical processes in step 2 are parameterized in terms of variables defining the change in the external factors.

### 3. EXPERIMENT DESIGN AND ANALYSIS PROCEDURES

As indicated in Chapter 1, this study is based on analyses of large amounts of regular radiosonde and windsonde data. Section 3.1 presents in detail the station locations, times of observation, periods of record, and data formats. Section 3.2 describes the vertical coordinate systems employed in the various analyses. This section also describes the methods used in computing the parameters defining the speed, stability and baroclinicity for each wind sounding; plus a description of the parameters used to define the observed wind profiles. Section 3.3 sets forth the criterion used in the various stratifications of the wind data. Finally, Section 3.4 treats the various factors which contribute to the variability in the observed wind profiles. The advantages and limitations of averaging radiosonde and windsonde data are discussed.

#### 3.1 Data Sources

All wind and temperature data utilized in this study were obtained on magnetic tape from the National Climatic Center, Asheville, North Carolina. The data are the product of the routine observational programs of the meteorological services of the United States (U. S. ) and Canada.

Wind Data for Specified Heights (Deck 545). This deck contains wind data for the surface and for heights of 150 meters (m), 300 m, 500 m, 1000 m, 1500 m . . . The first two levels (150 m and 300 m)

are heights above the surface while the remaining levels are heights above mean sea level.

Prior to June, 1957, the standard times for winds aloft soundings were 0300, 0900, 1500 and 2100 Greenwich Meridian Time (Z). During and after June, 1957, these times have been 0000, 0600, 1200 and 1800 Z. For some stations, data are available in the specified heights format for periods both before and after June, 1957. Combining the periods gives a total of eight times during the day for which wind data are available.

Wind data in the height format were analyzed for 3 stations in the U. S. and for weather Ship E. Table 3.1 lists these stations along with the elevations and periods of available data. The 06Z and 18Z observations for Shreveport were pibal observations during 10/63-12/64. The rest of the data were obtained by electronic tracking of windsondes and radiosondes.

Table 3.1

Stations included in the specified height wind analyses.

<u>Station</u>	<u>Period of Record</u>	<u>Elevation (meters)</u>
Jackson, Mississippi	2/1/56 - 7/30/64	101
Shreveport, Louisiana	1/11/56 - 12/31/64	79
Montgomery, Alabama	1/1/56 - 12/31/64	62
Ship E (35°N, 48°W)	1/1/56 - 12/31/64	0

Wind and Temperature Data for Specified Pressure Levels (Deck 645). One of the factors to be considered, namely baroclinicity, cannot be evaluated from single station analyses. The values of the thermal winds are dependent on horizontal derivatives of temperature. In evaluating these derivatives for the PBL, it is desirable to have a network of stations with relatively high radiosonde station density in an area of fairly smooth terrain. The network which best satisfies these criteria is shown in Fig. 3.1. This network consists of the 41 stations listed in Table 3.2.

The data source for the network analyses was radiosonde data in a specified pressure level format (Deck 645). Data were available for the standard observation times of 0000, and 1200Z. (These times correspond approximately to 1800 and 0600 local time for the network area.) This deck contains winds, temperatures, relative humidities, and heights for the surface and specified pressure levels. For pressures greater than 200 mb, the data are available at 50 mb intervals in the following sequence (1000 mb, 950 mb, 900 mb, 850 mb . . . ).

The data record treated in the network analyses is shown in Table 3.3. The winter analyses utilized a total of 20 months of data. With 19 stations in the interior of the network and approximately 30 days/month, the total data sample (19 x 30 x 20) included approximately 11,400 radiosonde observations for both 00Z and 12Z. Analyses for

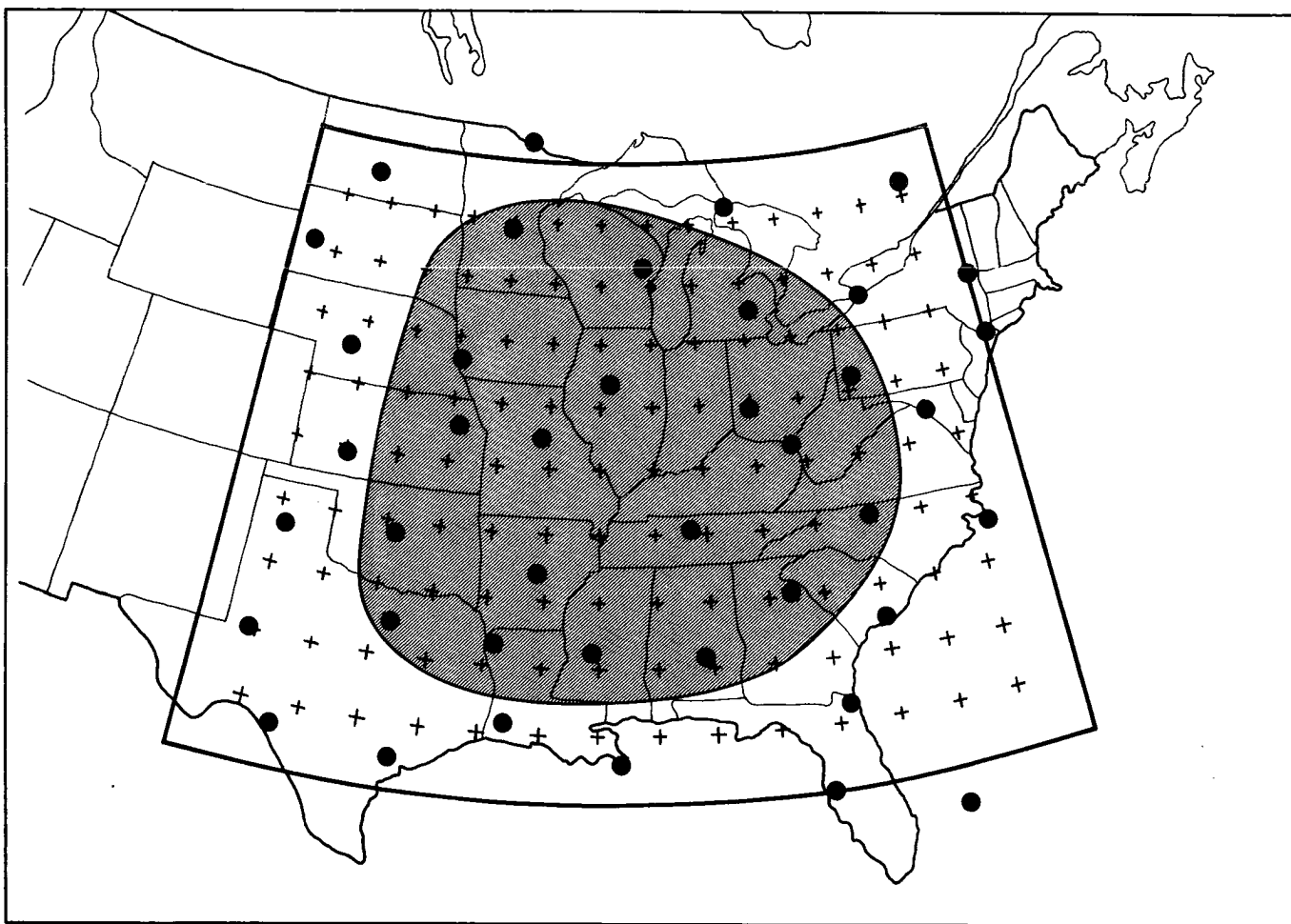


Fig. 3.1. Radiosonde Network. Data from stations outside the shaded area were utilized only to calculate the horizontal derivatives of temperature for the 19 interior stations. The superimposed  $2^{\circ}$  latitude -  $2^{\circ}$  longitude grid was used in all horizontal analyses.

Table 3.2

## Stations Included in the U. S. Network.

WMO#	WBAN#	Station	Lat. - Long. (deg.)		Sta. Elev. (meters)
1	72206	13889	Jacksonville, Florida	30.5 81.6	9
2	72208	13880	Charleston, South Carolina	32.9 80.0	15
3	72211	12842	Tampa, Florida	28.0 82.5	3
4	72226	13895	Montgomery, Alabama	32.3 86.4	62
5	72232	12884	Burwood, Louisiana	29.0 89.4	5
6	72235	13956	Jackson, Mississippi	32.3 90.2	101
*	72235	03940	Jackson, Mississippi	32.3 90.2	--
7	72240	03937	Lake Charles, Louisiana	30.2 93.2	10
8	72248	13957	Shreveport, Louisiana	32.5 93.8	79
9	72251	12926	Corpus Christi, Texas	27.7 97.5	13
*	72256	12912	Victoria, Texas	28.7 97.1	36
10	72259	13911	Fort Worth, Texas	32.8 97.0	176
11	72261	22010	Del Rio, Texas	29.4 100.8	313
12	72265	23023	Midland, Texas	32.0 102.2	872
13	72304	93729	Cape Hatteras, North Carolina	35.3 75.5	3
14	72311	13873	Athens, Georgia	34.0 83.3	247
15	72317	13723	Greensboro, North Carolina	36.1 79.9	270
16	72327	13897	Nashville, Tennessee	36.1 86.7	184
17	72340	13963	Little Rock, Arkansas	34.7 92.2	81
18	72353	13967	Oklahoma City, Oklahoma	35.4 97.6	398
*	72354	13919	Tinker AFB, Oklahoma	35.3 97.5	--
19	72363	23047	Amarillo, Texas	35.2 101.7	1099
20	72403	93734	Washington, D. C.	38.9 77.0	20
21	72425	03860	Huntington, West Virginia	38.4 82.6	255
22	72429	13840	Dayton, Ohio	39.9 84.2	306
23	72445	13983	Columbia, Missouri	39.0 92.4	239
24	72451	13985	Dodge City, Kansas	37.8 100.0	790
25	72456	13996	Topeka, Kansas	39.1 95.6	270
26	72518	14735	Albany, New York	42.8 73.8	89
27	72520	94823	Pittsburgh, Pennsylvania	40.5 80.2	373
28	72528	14733	Buffalo, New York	42.9 78.7	215
29	72532	14842	Peoria, Illinois	40.7 89.7	202
30	72553	94918	Omaha, Nebraska	41.4 96.0	406
31	72562	24023	North Platte, Nebraska	41.1 100.7	850
32	72637	14826	Flint, Michigan	43.0 83.7	234
33	72645	14898	Green Bay, Wisconsin	44.5 88.1	214
34	72655	14926	St. Cloud, Minnesota	45.6 94.2	318
35	72662	24090	Rapid City, South Dakota	44.1 103.1	966
36	72722	04734	Maniwakii, Quebec	46.4 76.0	170
37	72734	14847	S. St. Marie, Michigan	46.5 84.4	221
38	72747	14918	International Falls, Minnesota	48.6 93.4	361
39	72764	24011	Bismarck, North Dakota	46.8 100.8	506
40	74486	94789	New York City, New York	40.7 73.8	7
41	78063	12712	Gold Rock Creek, Grand Bahama Is.	26.6 78.3	6

\*Indicates station location changes during the period 1965-1970

the summer months utilized a total of 9 months of data or about 5,100 observations for both 00Z and 12Z.

Table 3.3

Period of record included in the network analyses.

	WINTER					SUMMER		
	Nov.	Dec.	Jan.	Feb.	Mar.	June	July	Aug.
1965	X	X						
1966	X	X	X	X	X	X	X	X
1967	X	X	X	X	X	X	X	X
1968	X	X	X	X	X	X	X	X
1969			X	X	X			

### 3.2 Analyses and Computations

Vertical Coordinates. Preliminary analyses suggested that the depth of the planetary boundary layer is frequently greater than the often quoted value of one kilometer (km). Consequently, this study was designed to include available data up to 2.5 - 3 km above the surface.

The vertical coordinates used in analyzing the data from the 4 stations listed in Table 3.1 are shown in Fig. 3.2. Wind data were available at each of the nine levels in Deck 545 format. All levels except those for 150 m and 300 m had to be adjusted for the 3 land stations. The data for the three land stations are combined. Eighty meters was chosen as a representative station elevation. Therefore, the 500 m

data were applied to 420 meters; 1000 m to 920 m; etc. The total depth became 2920 m for the 3 land stations and 3000 m for Ship E.

The heights of specified pressure levels above the surface varies from one station to another due to different station elevations. Likewise these heights vary in time due to the passage of "high" and "low" pressure systems. This height variability required that the specified pressure level radiosonde data be converted to a reference frame which would better indicate the height above the surface. The reference frame, which was utilized, is shown in Fig. 3.3. This system accounts for both station elevation differences and the time changes associated with moving pressure systems. Here the different levels above the surface are specified in terms of the surface pressure.

The analyses are restricted to the lowest 250 mb of the atmosphere. This corresponds approximately to the lowest 2.5 km. The 250 mb layer is subdivided by seven levels into a six layer model. Linear interpolation between the wind and temperature data in the specified pressure format provided wind and temperature data at each of the seven levels.

Computation of External Parameters. The external factors to be considered in this study are:

- (1) thermal stratification (stability)
- (2) the magnitude of the flow (speed)
- (3) baroclinicity .

Of these, only the magnitude of the flow can be computed directly from the wind data. The stability can be parameterized by the lapse rate of

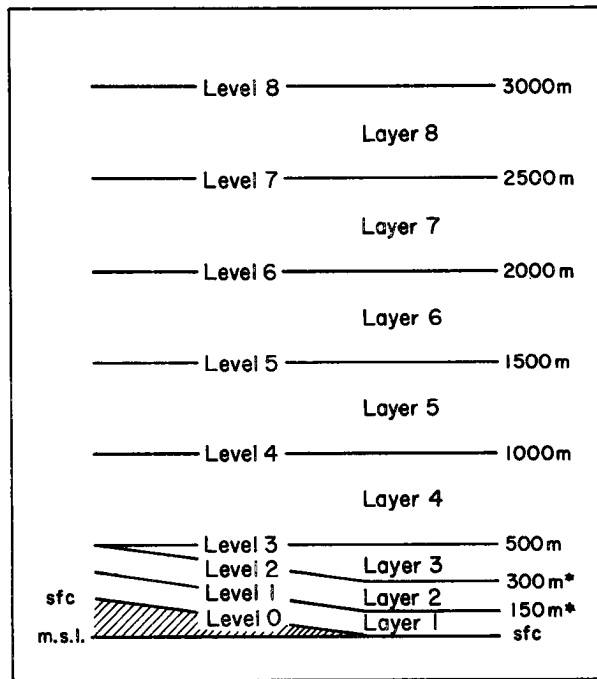


Fig. 3.2 Eight layer model used in the analyses of wind data for those stations given in Table 3.1. The asterisks indicate elevations above the surface.

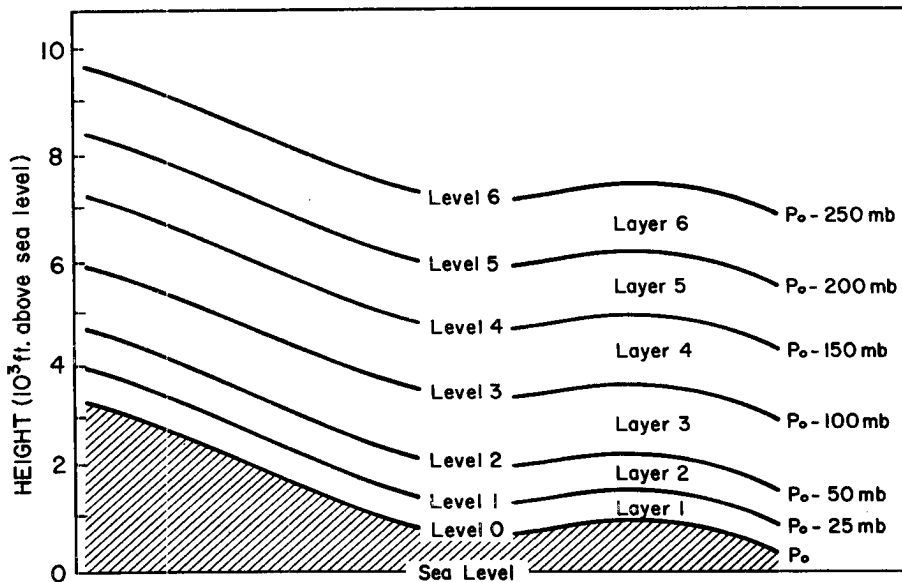


Fig. 3.3 Six layer model used in the network analyses.

temperature. Lapse rates can be estimated from the radiosonde temperature data, although some detail is lost in interpolating temperature values for specified levels. The thermal wind (baroclinicity) requires analysis of the horizontal temperature gradients before it can be evaluated. The procedures used to compute these parameters are discussed below.

(A) Stability -- Lapse rates were computed from the interpolated temperatures in the surface pressure based reference frame (Fig. 3.3). Values were obtained for only the lowest 150 mb (lowest four layers in Fig. 3.3). For each layer the temperature at the upper level was subtracted from the temperature at the lower level. With this convention, positive lapse rates correspond to decreasing temperatures with height. The values were then converted to units of  $^{\circ}\text{C}/100\text{ mb}$ . The symbol  $\Gamma$  is used to represent the lapse rates.

(B) Speed -- The speed parameter used in this study was the average speed in the lowest 100 mb. This was obtained by weighting the wind observations for the first four levels in Fig. 3.3 according to the depth of the layer for which they were representative, i. e.

$$S = .25 (|\vec{V}_{p_o-100}|) + .375 (|\vec{V}_{p_o-50}|) + .25 (|\vec{V}_{p_o-25}|) + .125 (|\vec{V}_{p_o}|) \quad (3.1)$$

(C) Thermal Wind Computations -- The thermal wind computations were made utilizing the expressions for pressure coordinates as given below:

$$\frac{\Delta u}{\Delta p} = \frac{R}{f_p} \left( \frac{\Delta T}{\Delta y} \right)_p \quad (3.2)$$

$$\frac{\Delta v}{\Delta p} = -\frac{R}{f_p} \left( \frac{\Delta T}{\Delta x} \right)_p \quad (3.3)$$

Two temperature analyses were made for each observation time. The first analysis utilized the average of the 950 mb and 900 mb temperatures as the initial data. In cases where the surface pressure is less than 950 mb, the surface temperature was substituted for the 950 mb temperature to arrive at an initial data value. The second analysis was made using the average of the 850, 800 and 750 mb temperatures as the initial data. The value of  $p$  in Eqs. (3.2) and (3.3) was set equal to 925 mb and 800 mb for the first and second analysis respectively.

Computing the thermal wind for a layer instead of at a given level smooths the effects of the height variation of temperature (inversions, etc.) on the value of the thermal wind. The decision not to use surface temperature in the analysis (except when required at stations with higher station elevations) is based on the fact that the surface temperatures are greatly affected by the immediate surroundings and often are not representative of the overall temperature pattern.

The horizontal temperature fields were analyzed by a modified version of an objective analysis program developed by Fritsch (1969). The two degree latitude x two degree longitude grid shown in Fig. 3.1 was used. Initial values for each grid point were obtained by weighting the data for the 5 closest stations. The grid values were then adjusted by two successive cubic spline interpolations. The horizontal temperature derivatives were evaluated by applying the centered finite difference approximation to the final grid values.

The station elevations of the inner 19 stations varied from 62 meters at Montgomery to 432 meters at Omaha. This implied a typical variation of only 35-40 millibars in surface pressure. Therefore, the thermal winds given by the first analysis were considered as representative for the first three layers in the surface pressure reference model given in Fig. 3.3. Similarly, the thermal winds from the second analysis were assigned to the upper three layers of the model. Using this scheme any changes in the thermal wind with height were reflected between the third and fourth layer. Usually, these differences were small. Exceptions were found near air mass boundaries and in the Great Plains where a significant diurnal variation in the direction of the thermal wind exists due to radiational heating and cooling on a sloping terrain.

Modification of the PBL wind profile by processes related to baroclinicity can best be determined from data taken in conditions with strong and variable thermal winds. It is well known that the

temperature gradients over the U. S. are typically much weaker in summer than in winter. For this reason, the thermal winds were computed only for the winter months. The summer data were only used to investigate stability variations.

As indicated in Section 2, the modifications due to baroclinicity should be proportional to the magnitude and orientation of the thermal wind relative to the low level wind. The parameter selected to define the magnitude is  $|\vec{V}_T| / S$  where  $\vec{V}_T$  is the thermal wind vector in the lowest 100 mb and  $S$  is the average speed in the lowest 100 mb. The parameter selected to define the orientation is the angle  $\psi$ , where  $\psi$  is defined as the angle measured clockwise from the wind direction 100 mb above the surface to the direction of  $\vec{V}_T$ . Both  $|\vec{V}_T| / S$  and  $\psi$  were computed for each individual observation.

Computations of Dependent Parameters. The parameters which define the observed wind profile are treated as dependent parameters. From the wind data (wind speed and direction at each level), the following were computed.

(A) The change in wind direction ( $\alpha_{T_j}$ ) in each of the layers defined in Figs. 3.2 and 3.3 -- The direction for the lower level was subtracted from the direction at the upper level such that positive differences indicate wind veering with height. The subscript  $T$  indicates the veering due to the thermal wind has not been eliminated from the data. The subscript  $j$  indicates the layer number defined in Figs. 3.2 and 3.3.

(B) Wind shear in each layer -- Wind components in meteorological coordinates (coordinates aligned with the north-south and east-west directions) were converted to components in a natural coordinate system. The natural coordinates were oriented so the positive  $s$  axis coincided with the wind vector at the lower level. The transformation equations are:

$$u'_l = -u_l \sin \gamma_l - v_l \cos \gamma_l = |\vec{V}_l| \quad (3.4)$$

$$v'_l = u_l \cos \gamma_l - v_l \sin \gamma_l = 0$$

$$u'_{l+1} = -u_{l+1} \sin \gamma_l - v_{l+1} \cos \gamma_l \quad (3.5)$$

$$v'_{l+1} = u_{l+1} \cos \gamma_l - v_{l+1} \sin \gamma_l$$

for the upper and lower levels respectively. Here  $u$  and  $v$  are the wind components in the meteorological coordinate system.  $u'$  and  $v'$  are the wind components in the natural coordinate system;  $\gamma$  is the wind direction; and the subscript  $l$  corresponds to the level number as defined in Figs. 3.2 and 3.3. The observed wind shear along ( $\Delta u'_{T_j}$ ) and perpendicular ( $\Delta v'_{T_j}$ ) to the flow at the lower level become:

$$\Delta u'_{T_j} = u'_{l+1} - u'_l \quad (3.6)$$

$$\Delta v'_{T_j} = v'_{\ell+1} \cdot \quad (3.7)$$

The subscript T indicates that the thermal wind or geostrophic shear is still present in the data. The subscript j indicates the layer number defined in Figs. 3.2 and 3.3. Fig. 3.4 provides a schematic diagram illustrating how this calculation was made. The values of  $\alpha_{T_j}$ ,  $\Delta u'_{T_j}$  and  $\Delta v'_{T_j}$  were computed for each observation. For the network analyses, this amounted to six values per observation, while eight were computed for the individual station analyses.

In about 5-10% of the observations, the data were missing for one or more of the levels. The change in wind direction and the wind shear could not be computed if the data for either of the two levels was missing. In this study, the computations were made for all possible layers instead of discarding the entire observation.

Additional criteria were established for cases of calm or light winds. When calm conditions were reported for a level, the angle ( $\alpha_T$ ) could not be computed for the two adjacent layers. In these instances the wind shear vector was not computed so that averages of the two parameters would be based on the same data sample. In conditions of light but non zero wind speeds, the wind direction can change greatly from one level to another. In these cases, it is no longer obvious whether the wind is veering or backing with height. If  $\alpha_T$  exceeded  $60^\circ$  in a given layer, the values of  $\alpha_T$ ,  $\Delta u'_T$ , and  $\Delta v'_T$

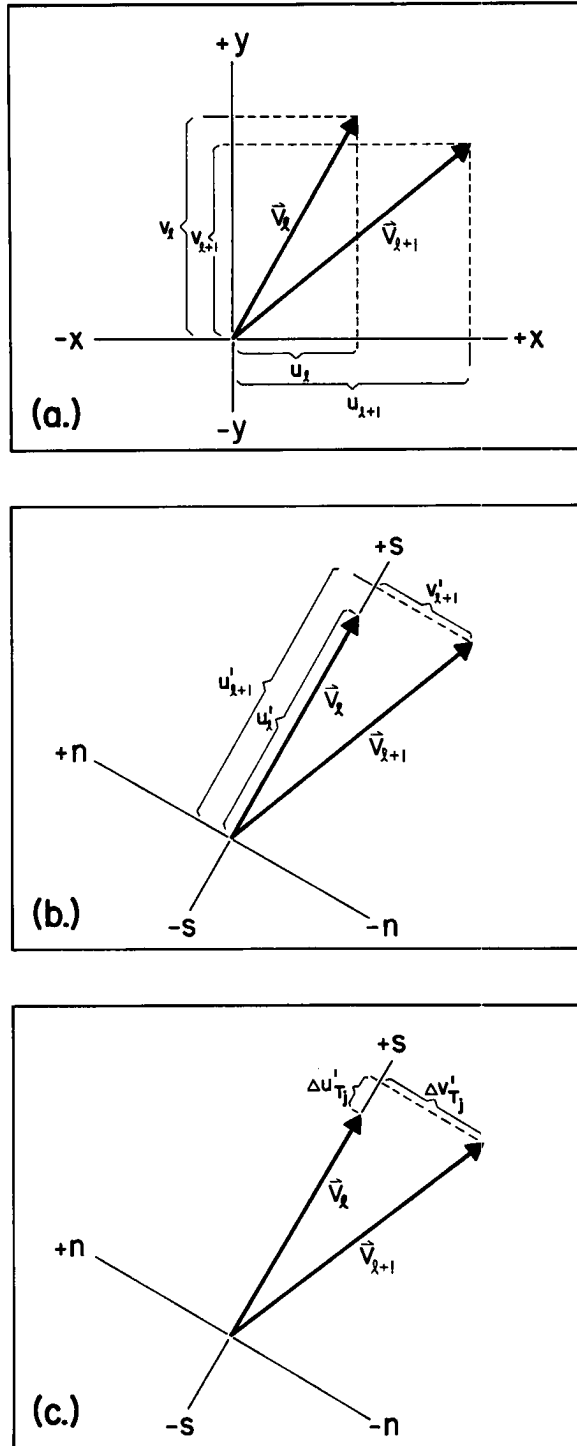


Fig. 3.4. Schematic diagram illustrating the method used to compute the wind shear between levels  $l$  and  $l+1$ . (a) Wind vectors and components in the meteorological coordinate system. (b) Wind vectors and components in the natural coordinate system. (c) Wind vectors and components of the wind shear in the natural coordinate system.

were discarded, maintaining the same data sample for the three parameters.

(C) Eliminating the geostrophic shear from the observed wind data -- The thermal wind vectors for each of the six layers in Fig. 3.3 were transformed into the natural coordinate system used to compute the observed shear (see Fig. 3.4). The resulting components of the geostrophic shear defined as  $\Delta u'_g$  and  $\Delta v'_g$  were subtracted from the observed shear.

$$\Delta u'_j = \Delta u'_{T_j} - \Delta u'_{g_j} \quad (3.8)$$

$$\Delta v'_j = \Delta v'_{T_j} - \Delta v'_{g_j} \quad (3.9)$$

Again  $j$  refers to the layer number in Fig. 3.3.

The resulting values of  $\Delta u'$  and  $\Delta v'$  along with the magnitude of the observed surface wind were utilized to construct a wind hodograph that had the geostrophic shear eliminated. Assuming geostrophic balance 250 mb above the surface, new veering angles were obtained from this hodograph. These veering angles, identified by the symbol  $\alpha$ , became the angle between the isobars and the observed wind. Fig. 3.5 illustrated how the hodographs were constructed and how the values of  $\alpha$  were obtained.

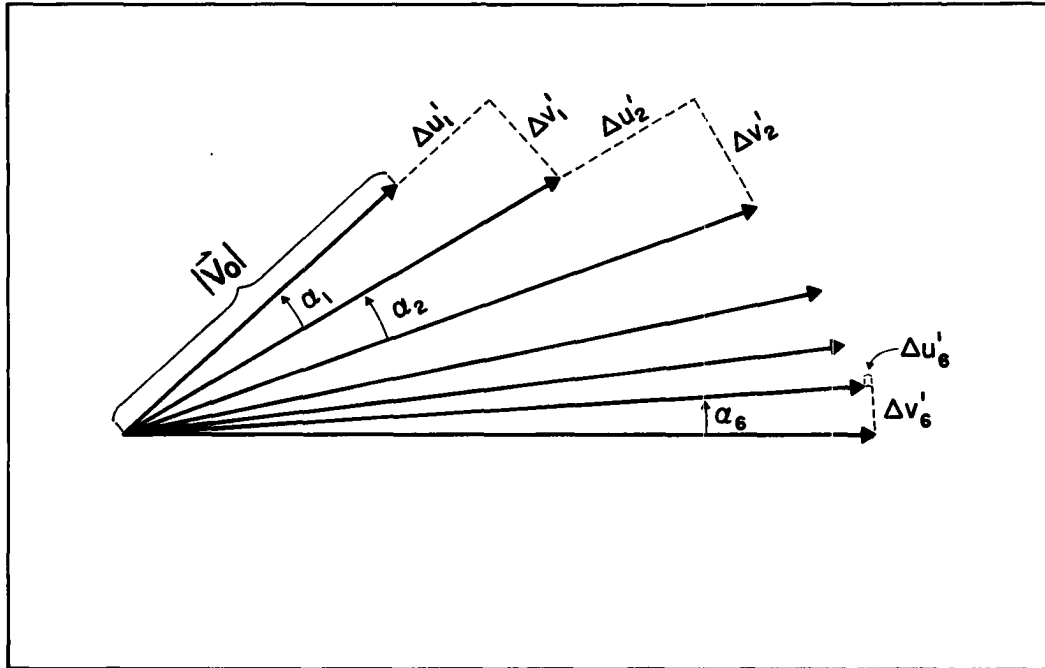


Fig. 3.5. Illustration of procedures employed in constructing hodographs.

### 3.3 Data Stratifications

Initially the role of the three external factors was assumed to be unknown. The proper methodology needed to establish the dependence of the PBL winds on any of these factors is to hold two of the factors constant and let the third vary. This means we must allow for all possible combinations of the three factors. Stratifications A and B are designed to satisfy these criteria. Both these stratifications treat only the winter data from the U. S. network.

Stratification A (five speed, three stability, and nine baroclinicity categories)

The dependent parameters defining the observed wind profiles ( $\Delta u'_T$ ,  $\Delta v'_T$  and  $\alpha_T$ ) are stratified using the categories of external parameters defined below. This scheme results in 135 possible

combinations of speed, stability and baroclinicity.

(A) Speed categories (based on the average speed in the lowest 100 mb) --

- (1)  $S \leq 5$  m/sec
- (2)  $5$  m/sec  $< S \leq 10$  m/sec
- (3)  $10$  m/sec  $< S \leq 15$  m/sec
- (4)  $15$  m/sec  $< S \leq 20$  m/sec
- (5)  $S > 20$  m/sec

(B) Stability categories (based on the average lapse rate in the lowest 100 mb) --

- (1)  $\bar{\Gamma} \leq 0^\circ\text{C}/100$  mb
- (2)  $0^\circ\text{C}/100$  mb  $< \bar{\Gamma} \leq 5^\circ\text{C}/100$  mb
- (3)  $\bar{\Gamma} > 5^\circ\text{C}/100$  mb

(C) Categories of baroclinicity (based on magnitude and direction of the thermal wind in the lowest 100 mb) --

- (1)  $\psi = 1-45^\circ$  ;  $|\vec{V}_T|/S \geq .2$
- (2)  $\psi = 46-90^\circ$  ;  $|\vec{V}_T|/S \geq .2$
- (3)  $\psi = 91-135^\circ$  ;  $|\vec{V}_T|/S \geq .2$
- (4)  $\psi = 136-180^\circ$  ;  $|\vec{V}_T|/S \geq .2$
- (5)  $\psi = 181-225^\circ$  ;  $|\vec{V}_T|/S \geq .2$
- (6)  $\psi = 226-270^\circ$  ;  $|\vec{V}_T|/S \geq .2$
- (7)  $\psi = 271-315^\circ$  ;  $|\vec{V}_T|/S \geq .2$
- (8)  $\psi = 316-360^\circ$  ;  $|\vec{V}_T|/S \geq .2$
- (9)  $|\vec{V}_T|/S < .2$  (negligible thermal wind)

The data combinations are identified by the three numbers corresponding to the speed, stability and thermal wind categories. For example the combination (3, 1, 7) includes those observations with  $S = 10-15$  m/sec,  $\bar{\Gamma} \leq 0^\circ\text{C}/100$  mb, and  $\psi = 271-315^\circ$  with  $|\vec{V}_T|/S \geq .2$ .

Stratification B (five speed, three stability, and nine baroclinicity categories--geostrophic shear eliminated from the wind data)

The categories of speed, stability and baroclinicity are identical to those defined in Stratification A. The dependent parameters (  $\Delta u'$ ,  $\Delta v'$ , and  $\alpha$  ) are those obtained after the geostrophic shear was eliminated from the observed data.

The results of Stratification B were used to obtain average values for two additional quantities. These are the geostrophic wind speed and the ageostrophic winds. Values were obtained at each of the seven levels defined in Fig. 3.3 for each of the 135 possible combinations.

(A) Average geostrophic wind speeds—Mean wind hodographs for each combination of speed, stability and thermal wind were constructed. The magnitude of the surface wind vector was set equal to the average surface speed. Vectors for successively higher levels were obtained by adding the average shear ( $\overline{\Delta u'}$  and  $\overline{\Delta v'}$ ) to the existing vectors. The procedure is illustrated in Fig. 3.6. Since the geostrophic shear is eliminated from the values of  $\overline{\Delta u'}$  and  $\overline{\Delta v'}$ , the magnitude of the vector for 250 mb is considered to be equal to the average surface geostrophic wind speed  $\left| \overline{\vec{V}}_{g_0} \right|$ . The average geostrophic speed at the top level  $\left| \overline{\vec{V}}_{g_6} \right|$  was set equal to the average observed speed at level six. The geostrophic speeds at the remaining levels were then obtained by linear interpolation between the values for the surface and the top level.

(B) Average ageostrophic wind components — The deviation of the wind vector from the geostrophic wind vector is the ageostrophic wind. The average ageostrophic components parallel ( $\overline{u''}$ ) and perpendicular ( $\overline{v''}$ ) to the geostrophic wind were taken from the mean wind hodographs as shown in Fig. 3.6. In this study,  $v''$  is positive for ageostrophic flow towards lower pressure, and  $u''$  is positive when the wind component along the isobar is less than the geostrophic speed.

Much of the variations in the magnitude of  $u''$  and  $v''$  are due to variations in the magnitude of the geostrophic wind. For this reason, the dimensionless quantities  $u''/|\overline{\vec{V}}_g|$  and  $v''/|\overline{\vec{V}}_g|$  were computed. These two dimensionless quantities, plus the angle between the wind and isobars ( $\alpha$ ), are used throughout this paper to define the characteristics of the wind profile.

The lapse rate is typically not constant in the lowest 1-2 km but changes drastically both as a function of height and time. This limits

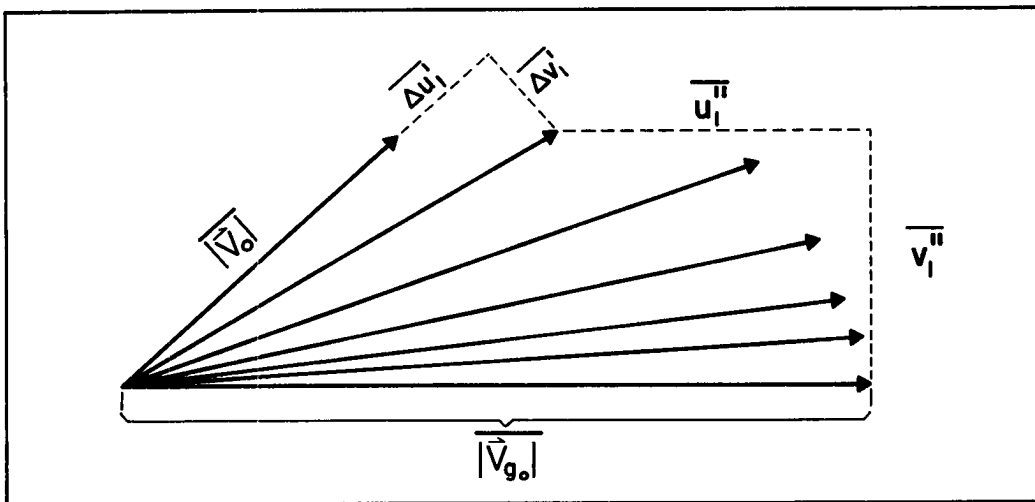


Fig. 3.6. Illustration of how the components of the ageostrophic wind were obtained.

the usefulness of the mean lapse rate parameterization used in Stratifications A and B. Therefore, two additional Stratifications (C and D) were carried out in an attempt to better define the variations related to stability. In these stratifications, stability is the only external factor.

Stratification C (detailed lapse rate stratification)

The lowest 150 mb of the atmosphere is divided into four layers as shown in Fig. 3.3. The lapse rate in each layer is categorized independent of the lapse rate in the other three layers. The categories are defined as follows:

- (1)  $\Gamma \leq 3^{\circ}\text{C}/100 \text{ mb}$
- (2)  $3^{\circ}\text{C}/100 \text{ mb} < \Gamma \leq 7^{\circ}\text{C}/100 \text{ mb}$
- (3)  $\Gamma > 7^{\circ}\text{C}/100 \text{ mb}$  .

These categories correspond approximately to absolutely stable, conditionally unstable, and unstable thermal stratifications. With four layers and three different lapse rate categories in each layer, a total of 81 possible combinations exist. The combinations are identified in a manner similar to that used in Stratifications A and B. The combination (3, 3, 1, 1) for example, indicates near adiabatic lapse rate in the lowest 50 mb with a stable layer from 50-150 mb above the surface. Stratification C treated the winter and summer data separately. The winter stratification was made using the dependent parameters (  $\Delta u'$ ,  $\Delta v'$  and  $\alpha$  ) obtained after elimination of the geostrophic shear. The summer analysis used the observed values (  $\Delta u'_{\text{T}}$ ,  $\Delta v'_{\text{T}}$  and  $\alpha_{\text{T}}$  )

with no corrections for geostrophic shear. It is assumed that the geostrophic shear will largely be eliminated from the summer data by the averaging process. For this assumption,  $\overline{\Delta u'_T} \approx \overline{\Delta u'}$ ;  $\overline{\Delta v'_T} \approx \overline{\Delta v'}$  and  $\overline{\alpha_T} \approx \overline{\alpha}$ .

Stratification D (stratification by time of observation--diurnal variations)

This stratification treats the data from the four stations given in Table 3.1. In this case, the data are categorized by season, with the seasons being defined as follows:

Winter	- (December - February)
Spring	- (March - May)
Summer	- (June - August)
Fall	- (September - November)

Within each season, the dependent parameters ( $\Delta u'_T$ ,  $\Delta v'_T$  and  $\alpha_T$ ) were stratified by time of observation. Data were available at three hour intervals, making a total of eight observations per day. This provides a way of examining the mean diurnal changes in the wind profiles. Though lapse rates cannot be computed, the diurnal changes can be related to the typical heating and cooling of the lower atmosphere. Again we assume that  $\overline{\Delta u'_T} \approx \overline{\Delta u'}$ ;  $\overline{\Delta v'_T} \approx \overline{\Delta v'}$  and  $\overline{\alpha_T} \approx \overline{\alpha}$ .

### 3.4 Analysis of Variance

An indication of the variability in the wind profiles for the winter season is given in Table 3.4. This table lists the standard deviations of the observed veering for the 19 interior stations in the U. S. network. From a statistical viewpoint, the variability results from a

Table 3.4

Standard deviations (degrees) of the observed wind veering.

Layers (millibars above surface)

Time	0-25	26-50	51-100	101-150	151-200	201-250	0-250
00Z	16.0	11.8	18.5	18.7	17.2	14.9	61.3
12Z	19.3	12.5	19.1	18.9	17.0	17.0	61.5

combination of errors in the data and real differences. In the following paragraphs the sources of the observed variability will be discussed.

Observational Errors. In the data making up any individual sounding, the possibility of errors exists due to the accuracy limitations of the observing system. In addition, errors may be introduced in the data reduction procedure or in any subsequent handling of the data. While these errors may contribute to the variability of the wind veering, it seems reasonable to assume that these errors are random. The methodology used in this study, namely averaging the data from many soundings to obtain composite or average profiles will eliminate the effects of these random errors.

Local Variations. At any time, the actual wind may be considered to be made up of a mean and a perturbation. In the PBL these perturbations are most commonly associated with the turbulent eddies. At other times perturbation arises due to mesoscale features such as

thunderstorms. While these variations are real and contribute to the variability in the wind profiles, they should be eliminated in a study of the mean wind profiles. Like observational errors, the variations due to gust scale turbulence and mesoscale systems are considered to be random in their occurrence. Thus, we assume that the effects of local variations are eliminated in the averaging process.

Topographical Effects. At some stations, the local topography modifies the planetary boundary layer wind profile. Since these modifications may be systematic at any one station, averaging the data does not eliminate these effects. If, however, the data from several stations are combined, as is the case in this study, the probability of the topographical effects being eliminated from the average value is good.

Vertical Resolution of Wind Data. The wind data provided in either the specified height format or the specified pressure format is actually an average wind for a layer of the atmosphere. For all altitudes considered in this study, the horizontal displacement of a balloon for a two minute period is converted to a wind speed and direction. The average rate of rise of the balloons is near 300 m/minute. The derived wind data is therefore an average for a layer approximately 600 m thick. This wind is then assigned to the height corresponding to the balloon elevation at the intermediate time. In the data reduction procedures, the two minute average wind is computed at one minute intervals in an overlapping fashion. The wind data assigned to the

specified height levels in Deck 545, or the specified pressure levels in Deck 645 are obtained by linear interpolation between elevations of the one minute interval wind data.

Due to the limits in the vertical resolution, the details existing in the actual wind profile are suppressed or smoothed in the resulting wind data. The result of this smoothing is to suppress the variability in the observed data. The true variability in the wind profiles may therefore be slightly larger than those given in Table 3.4.

If the details, which are lost by smoothing, are random variations, the averaging process will still yield an accurate profile of the mean wind profile. If, however, certain systematic but detailed features exist in the mean wind profiles, these features cannot be preserved in the average profiles.

The limited vertical resolution and subsequent smoothing in the collected data are the most serious drawbacks to a statistical treatment of routine radiosonde and windsonde data for the PBL. Nevertheless, the qualitative aspects of the major features in the actual wind profiles should still exist in the average profiles.

Variability Caused by External Factors. The characteristics of the wind profile in the PBL are influenced by:

- (1) Baroclinicity
- (2) Stability
- (3) Magnitude of the wind velocity
- (4) Accelerating or non-steady flow
- (5) Changes in surface roughness

The present study considers only the first three factors. Table 3.5 provides standard deviations of the wind veering for selected categories from Stratification B. The differences between the standard deviations in Table 3.4 and the average standard deviations in Table 3.5 are a measure of how much of the total variability is explained by variations in the first three factors listed above. (One would expect an even greater reduction if the number of categories for each factor were increased.) For the individual levels the standard deviation decreases from 30-50%. This implies a 50-75% reduction in the variance.

The standard deviation for the total veering in the lowest 250 mb is reduced from near  $60^{\circ}$  to near  $30^{\circ}$ . This corresponds to about a 75-80% reduction in the variance. This comparison suggests that a majority of the observed variability in the wind profiles for the lowest 2.5 km is related to changes in speed, stability or the direction and magnitude of the thermal wind.

For Stratification B,  $30^{\circ}$  is taken as a representative value of the standard deviation of the veering in the lowest 250 mb. For this amount of scatter in the data, the computed mean veering using 100 observations should be within  $\pm 5^{\circ}$  of the true mean approximately 90% of the time. For Stratifications C and D the standard deviation will be near  $60^{\circ}$ . For these Stratifications the computed mean based on 100 observations, should be within  $\pm 5^{\circ}$  of the true mean about 60% of the time. The average veering profiles obtained from Stratifications A, B and D and shown in the following chapters are all based on data

samples greater than 100. Veering profiles obtained from Stratification C are based on at least 50 observations.

Table 3.5

Standard deviations (degrees) for selected categories from Stratification B. (See Section 3.3 for a description of the categories.)

		Layers (millibars above surface)						
Time 00Z		0-25	26-50	51-100	101-150	151-200	201-250	0-250
Cate- gories	# of Obs.							
3,3,1	135	9.2	4.6	7.2	8.4	6.8	6.9	23.3
3,3,2	62	10.1	4.0	8.5	7.7	8.4	8.1	27.8
3,3,3	61	11.2	5.3	8.7	10.2	10.2	11.2	32.7
3,3,4	99	10.0	4.7	9.9	10.1	10.4	10.1	30.9
3,3,5	58	9.2	4.5	9.3	10.1	13.9	11.3	30.2
3,3,6	64	10.4	6.1	9.6	10.4	13.7	13.5	34.5
3,3,7	237	8.8	4.9	7.8	10.2	10.4	9.2	27.1
3,3,8	336	8.1	4.1	7.7	8.5	7.8	7.1	24.3
3,3,9	405	9.5	4.4	7.8	7.3	8.2	8.2	24.5
Average		9.6	4.4	8.5	9.2	10.0	9.5	28.4

Time 12Z

3,1,1	158	16.9	8.8	9.8	9.4	10.1	8.9	33.6
3,1,2	124	20.6	9.0	11.7	12.7	10.2	8.6	35.6
3,1,3	98	20.1	7.9	12.0	11.9	9.8	9.8	34.4
3,1,4	47	19.5	8.5	13.4	14.4	13.5	13.6	36.5
3,1,5	34	11.2	7.3	12.5	12.6	17.1	14.8	43.3
3,1,6	61	14.3	7.9	11.8	11.1	9.1	11.8	34.8
3,1,7	115	13.9	7.2	11.3	10.0	9.8	9.4	29.3
3,1,8	166	12.2	6.8	10.6	9.8	8.7	8.4	28.7
3,1,9	388	16.0	6.0	8.6	9.2	9.3	11.3	26.0
Average		16.1	7.7	11.3	11.2	10.8	10.7	31.0

## 4. PLANETARY BOUNDARY LAYER WINDS IN BAROCLINIC CONDITIONS

In Chapter 2, it was argued that two additional processes, not present in barotropic conditions, become important in conditions with large horizontal temperature gradients. The direct effect is that the pressure gradient (i. e., the geostrophic wind) will change with height. In Section 4.1, observational results are presented to demonstrate this effect.

The second or indirect effect is anticipated from the fact that baroclinicity alters the vertical shear in an existing turbulent boundary layer. This modifies the vertical transport of momentum and ultimately leads to a modification of the mean wind profile from that expected in barotropic conditions. Section 4.2 presents considerable observational evidence indicating such modifications exist in the planetary boundary layer. The angle between the wind and isobars; the ageostrophic wind components; the surface stress and the surface wind speed are all shown to be a function of the orientation of the thermal wind vector relative to the surface geostrophic wind. These results are utilized in constructing a physical model of this indirect modification. Finally, the potential importance of the geostrophic shear in selected atmospheric processes is discussed in Section 4.3.

### 4.1 Direct Effects of Geostrophic Shear

In Chapter 3 (Section 3.2), the variations in the geostrophic shear were defined by the parameters  $\psi$  and  $|\vec{V}_T|/S$ . The definition of  $\psi$

and  $|\vec{V}_T|/S$  are restated below. The angle  $\psi$  is measured clockwise from the wind direction 100 mb above the surface to the direction of the thermal wind for the lowest 100 mb (see Fig. 4.1). The quantity  $|\vec{V}_T|/S$  is the ratio of the magnitude of the thermal wind for the lowest 100 mb to the average wind speed in the lowest 100 mb.

Table 4.1 lists the combinations of speed, stability and thermal wind categories used to obtain the values shown in Figs. 4.2-4.5 and 4.7 - 4.10 and in Tables 4.2 - 4.6. In obtaining average values for each thermal wind category, the combinations were weighted equally, thereby eliminating any systematic trends related to speed or stability. The remaining combinations of speed and stability were not used because of much smaller data samples.

Average magnitudes of  $|\vec{V}_T|/S$  for each thermal wind category are given in Table 4.2. These values indicate the magnitudes of the thermal winds are somewhat larger for the cold air advection cases. The value of  $|\vec{V}_T|/S$  was  $\geq .2$  in 85% of the 00Z observations and  $\geq .2$  in 81% of the 12Z observations.

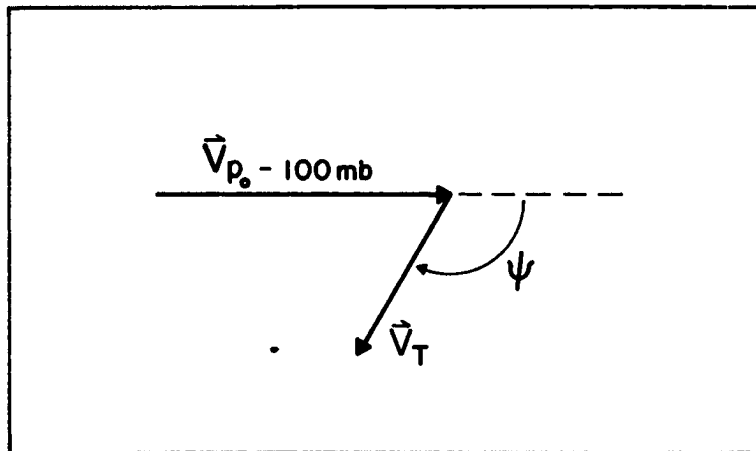


Fig. 4.1. Schematic diagram defining the angle  $\psi$ .

Table 4.1

Combinations of categories from Stratifications A and B which were used to obtain the values shown in Figs. 4.2-4.5, and Figs. 4.7-4.10. The number of observations is given for each combination. In obtaining average values for each thermal wind category, the combinations were weighted equally. (See Section 3.3 for a description of the categories.)

00Z		Number of Observations								
Categories		Thermal wind categories								
Speed	Stability	1	2	3	4	5	6	7	8	9
2	2	223	232	205	171	122	132	201	255	181
3	2	92	95	88	46	32	40	63	90	235
2	3	310	198	165	204	203	228	457	625	398
3	3	135	62	61	99	58	64	237	336	405

12Z		Number of Observations								
Categories		Thermal wind categories								
Speed	Stability	1	2	3	4	5	6	7	8	9
2	1	335	323	255	166	148	234	334	429	336
3	1	158	124	98	47	34	61	115	166	388
2	2	169	123	86	101	156	232	363	322	240
3	2	120	52	37	36	69	88	160	187	363

In Fig. 4.2, the average observed veering angle at 00Z is plotted as a function of height for cases of significant warm air advection, ( $\psi = 46^\circ - 135^\circ$ ,  $|\vec{V}_T|/S \geq .2$ ); significant cold air advection, ( $\psi = 226^\circ - 315^\circ$ ,  $|\vec{V}_T|/S \geq .2$ ); and negligible thermal wind, ( $|\vec{V}_T|/S < .2$ ). In Fig. 4.2 and throughout this paper, the veering angles are plotted as deviation of wind direction from the direction at the top level. Here, the top level is 250 millibars above the surface. Large differences are found in the observed veering for the warm and cold air advection cases. Contrast, for example, surface values of  $\alpha_T$  of  $70^\circ$  and  $-21^\circ$  for warm air and cold air advection respectively. The geostrophic veering is positive for warm air advection and negative for cold air advection. The negligible thermal wind case portrays the more typical profile of observed veering.

Fig. 4.2 indicates the geostrophic shear resulting from horizontal temperature gradients has a profound effect on the observed PBL wind veering. The next problem is to determine if the existence of geostrophic shear modifies the angle between the isobars and the winds, or ageostrophic wind components.

#### 4.2 Indirect Effects of Geostrophic Shear

Variations of Wind Veering. Fig. 4.2 also shows the veering as a function of height after the geostrophic veering has been subtracted from the observed veering. The veering angle is now the angle between the observed wind and the isobars ( $\alpha$ ). As expected, the profile for the negligible thermal wind cases remains essentially the same.

Table 4.2

Average values of  $|\vec{V}_T|/S$  during the winter season for the nine thermal wind categories.

Thermal wind category	12Z	00Z
1-45 $ \vec{V}_T /S \geq .2$	.49	.49
46-90 $ \vec{V}_T /S \geq .2$	.46	.45
91-135 $ \vec{V}_T /S \geq .2$	.48	.47
136-180 $ \vec{V}_T /S \geq .2$	.56	.51
181-225 $ \vec{V}_T /S \geq .2$	.57	.58
226-270 $ \vec{V}_T /S \geq .2$	.61	.63
271-315 $ \vec{V}_T /S \geq .2$	.58	.61
316-360 $ \vec{V}_T /S \geq .2$	.55	.55
$ \vec{V}_T /S < .2$	.13	.13

However, large changes occurred in the other two classes. The important result is that, in the lowest 1 km, the angle between the wind and isobars for the cold air advection cases are significantly greater than the values for warm air advection. This is completely opposite to the observed veering comparisons.

Figs. 4.3 and 4.4 show in more detail the dependence of the angle between wind and isobars on the direction of the thermal wind in relation to the wind at approximately 1 km above the surface. Values of  $\psi$  from approximately  $330^\circ$ - $150^\circ$  represent warm air advection; and values from  $150^\circ$ - $330^\circ$ , cold air advection. For both 00Z and 12Z,

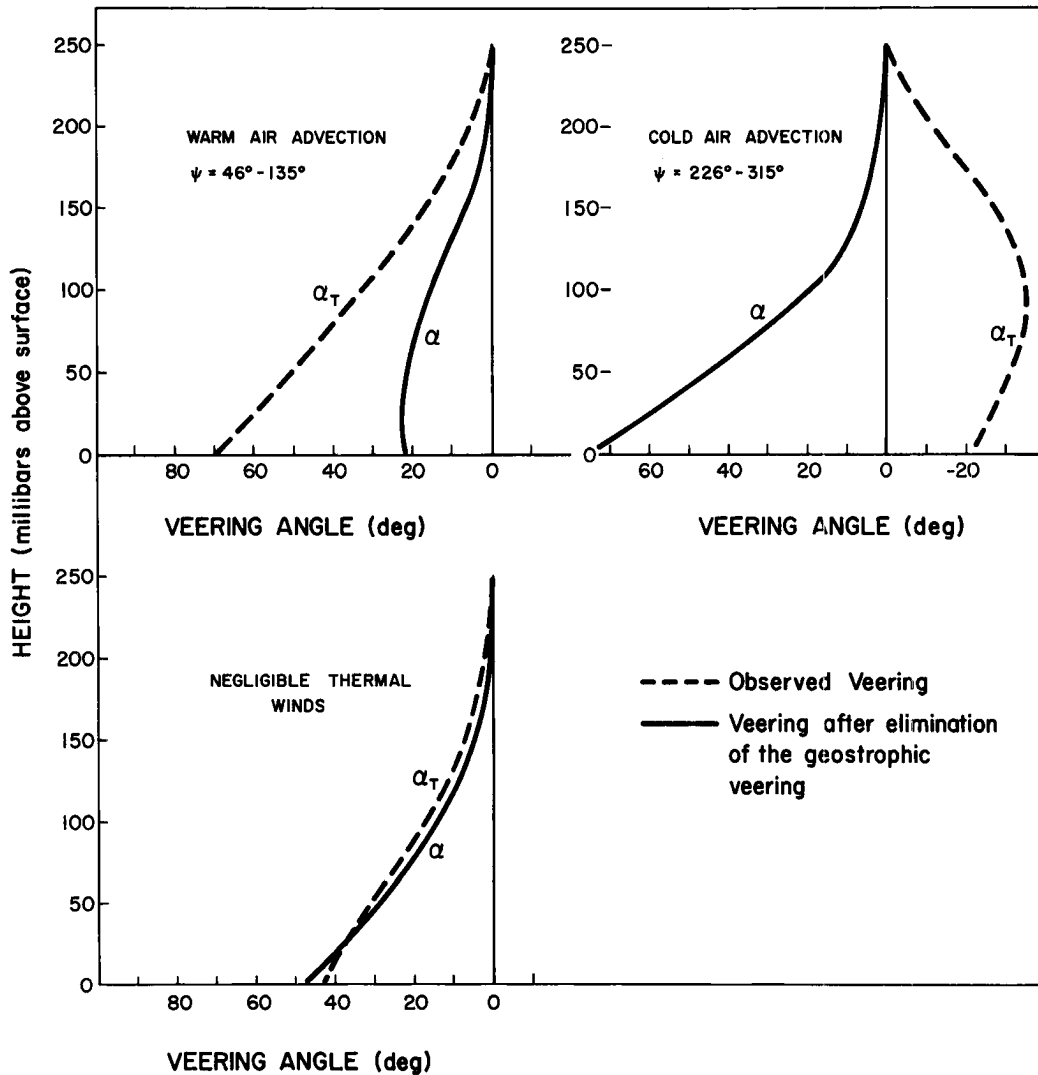


Fig. 4.2. Comparison of the average veering angles prior to and after the elimination of the geostrophic veering. The angle  $\psi$  is measured clockwise from the direction of the wind 100 mb above the surface to the direction of the mean thermal wind in the lowest 100 mb.

we see that the profiles are dependent on the value of  $\psi$ . Again the veering angles are significantly larger in cases of cold air advection.

In Fig. 4.5, the angle between the surface wind and surface isobar from Figs. 4.3 and 4.4 is shown as a function of  $\psi$ . The range amounts to 56 degrees for the 00Z cases and 35 degrees for the 12Z

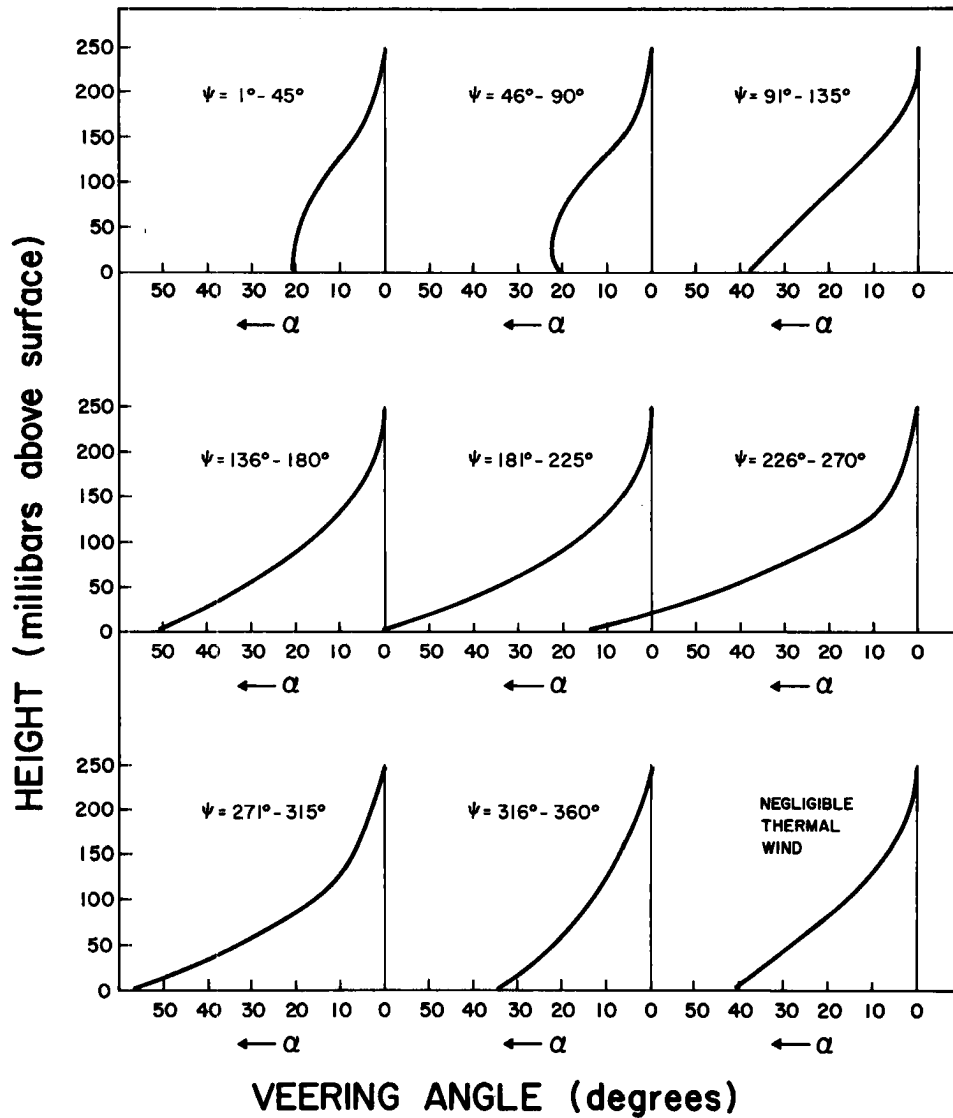


Fig. 4.3. Angle between wind and isobars versus height at 00Z for the nine thermal wind categories. The geostrophic veering has been eliminated from the data. The angle  $\psi$  is measured clockwise from the direction of the wind 100 mb above the surface to the direction of the thermal wind vector for the lowest 100 mb.

cases. Minimum and maximum values of  $\alpha_0$  occur for  $\psi \approx 45^\circ$  and  $245^\circ$ , respectively.

The surface geostrophic wind is often more easily obtained than the actual wind 100 mb above the surface. Therefore, it is desirable to have the information shown in Fig. 4.5 expressed as a function of

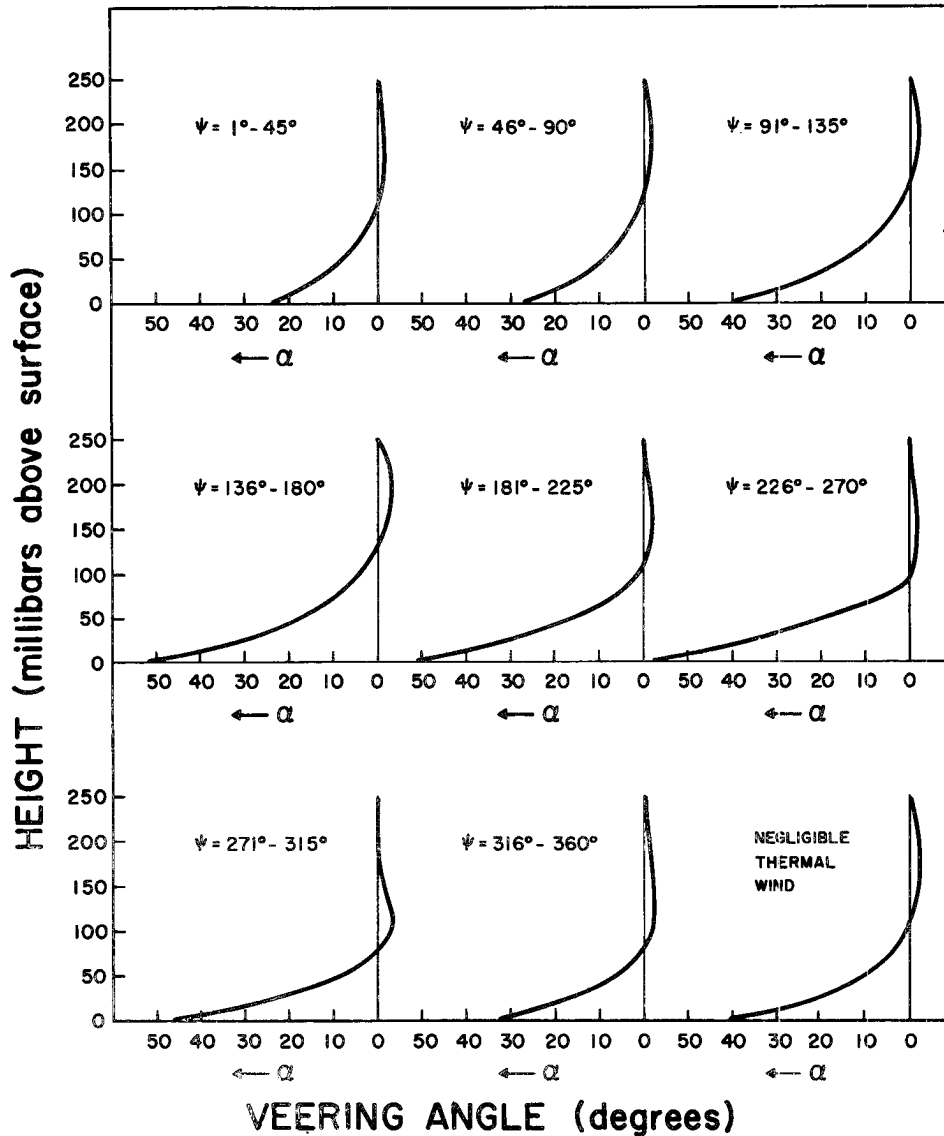


Fig. 4.4. Angle between wind and isobars versus height at 12Z for nine thermal wind categories. The geostrophic veering has been eliminated from the data. The angle  $\psi$  is measured clockwise from the direction of the wind 100 mb above the surface to the direction of the thermal wind vector for the lowest 100 mb.

the angle ( $\beta$ ) between the direction of the surface geostrophic wind and the thermal wind in the lowest 100 mb (see Fig. 4.6). In the analysis procedures, surface pressure data reduced to sea level were not available and the surface geostrophic winds were not computed. However, the average difference between the angles  $\psi$  and  $\beta$  can

be obtained as follows. For the eight categories of  $\psi$ , the average directional difference ( $\alpha'$ ) between the surface wind and the wind at 100 mb above the surface can be obtained from the average observed veering angles. The values of  $\alpha'$  were obtained from the results of Stratification A. The directional difference ( $\alpha_0$ ) between the surface wind and the surface geostrophic wind is given in Fig. 4.5 (from stratification B). The average difference ( $\alpha''$ ) between the surface geostrophic wind direction and the wind direction at 100 mb above the surface is then,

$$\alpha'' = \alpha' - \alpha_0 . \quad (4.1)$$

Therefore, the angle  $\beta$  is given by,

$$\beta = \psi + \alpha'' . \quad (4.2)$$

Fig. 4.7 shows  $\alpha_0$  as a function of  $\beta$ . The amplitudes obviously remain the same as those in Fig. 4.5. Note, however, that the minimum values of  $\alpha_0$  now occur at  $\beta \approx 65^\circ$  and the maximum values of  $\alpha_0$  occur at  $\beta \approx 210^\circ$ .

Variation in Ageostrophic Winds. Tables 4.3 and 4.4 give the average values of  $|\vec{V}_g|$ ,  $v''/|\vec{V}_g|$  and  $u''/|\vec{V}_g|$  at each level for each of the nine thermal wind categories for 00Z and 12Z, respectively.

Remember that  $v''$  is the ageostrophic wind component perpendicular to the isobar while  $u''$  is the component parallel to the isobar. Fig.

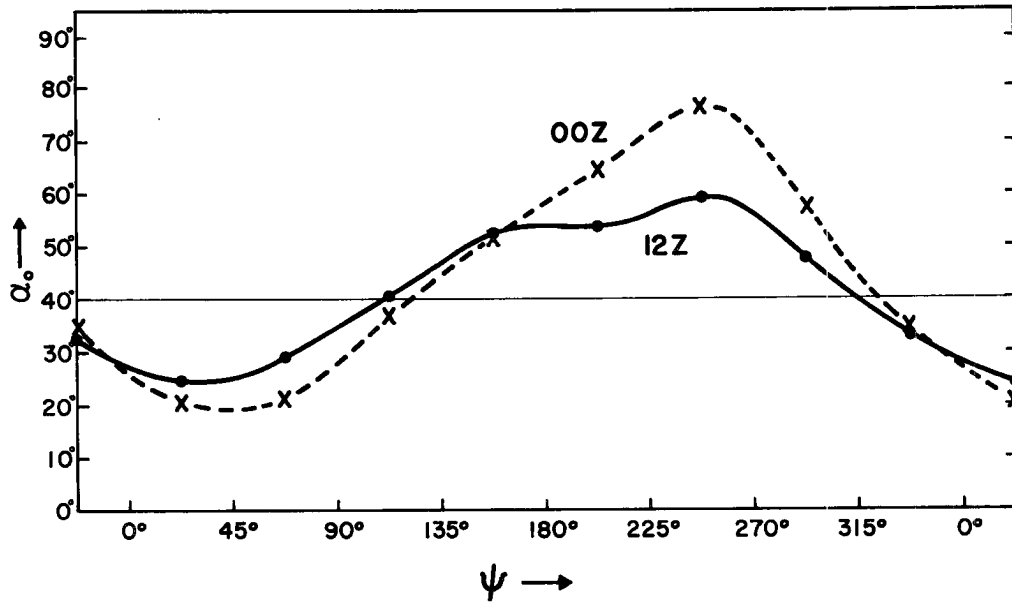


Fig. 4.5. Angle between the surface wind and surface isobars as a function of the angle between the wind vector 100 mb above the surface and the thermal wind vector in the lowest 100 mb.

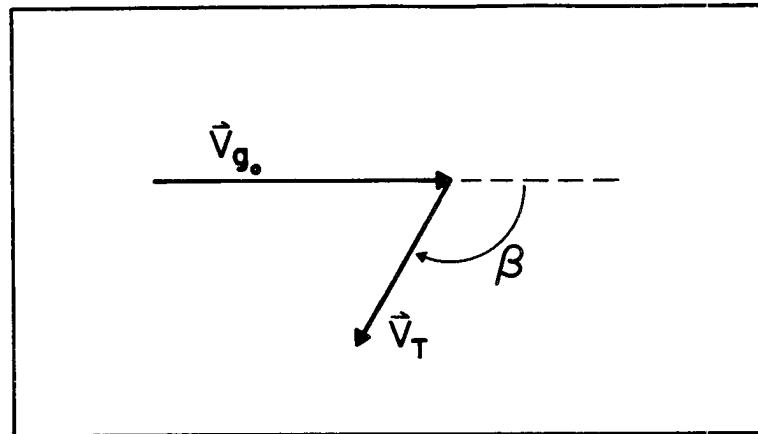


Fig. 4.6. Schematic diagram defining the angle  $\beta$ .

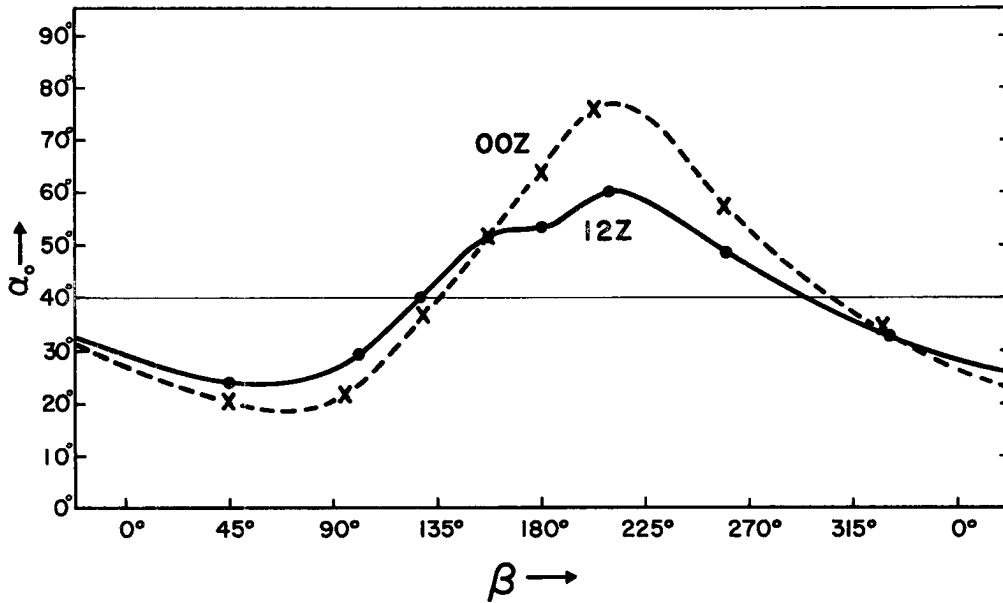


Fig. 4.7. Angle between the surface wind and surface isobars as a function of the angle between the surface isobars and the thermal wind.

4.8 provides a comparison of the normalized ageostrophic components for cold and warm air advection. In the lowest 1 km there is significantly more cross isobaric flow in the cold air advection cases. Also note the large difference between the values for 00Z and 12Z. The major reason for this difference is the more stable lapse rate categories associated with the 12Z data. These effects are treated in detail in Chapter 5.

At 00Z, Fig. 4.8 shows greater values of  $u'' / |\vec{V}_g|$  in the lowest 700 m for the cold air advection cases. The difference, however, is not as great as for the  $v'' / |\vec{V}_g|$  values. At 12Z, there is no significant difference between cold and warm air advection.

Table 4.3

Average values of the geostrophic wind speed, and the normalized ageostrophic wind components for eight categories of  $\psi$  (or  $\beta$ ) and for conditions with negligible thermal winds. Time 00Z.

		Height (millibars above surface)						
		0	25	50	100	150	200	250
$\psi$ (deg)	$\beta$ (deg)	Average Geostrophic Wind Speed - $ \vec{V}_g $ (m/sec)						
01-45	06-70	9.1	10.0	10.9	12.7	14.4	16.2	18.0
46-90	71-112	12.1	12.6	13.0	14.0	14.9	15.8	16.7
91-135	113-142	14.4	14.4	14.4	14.3	14.3	14.2	14.2
136-180	143-168	14.7	14.4	14.1	13.4	12.9	12.3	11.8
181-225	169-190	14.3	13.9	13.4	12.5	11.6	10.6	9.6
226-270	191-230	12.8	12.8	12.7	12.7	12.6	12.5	12.4
271-315	231-297	9.8	10.6	11.4	12.9	14.4	15.8	17.2
316-360	298-05	7.8	9.0	10.1	12.3	14.6	16.8	18.9
$ \vec{V}_T /S < .2$		12.2	12.4	12.6	13.0	13.4	13.8	14.2
$\psi$ (deg)	$\beta$ (deg)	Average Value of $v'' /  \vec{V}_g $						
01-45	06-70	.30	.32	.38	.25	.08	.03	---
46-90	71-112	.21	.30	.34	.26	.11	.03	---
91-135	113-142	.22	.31	.35	.27	.11	.03	---
136-180	143-168	.23	.33	.35	.27	.12	.03	---
181-225	169-190	.28	.38	.41	.29	.15	.08	---
226-270	191-230	.43	.55	.58	.35	.13	.06	---
271-315	231-297	.51	.60	.55	.28	.10	.04	---
316-360	298-05	.53	.57	.52	.29	.12	.04	---
$ \vec{V}_T /S < .2$		.32	.41	.43	.29	.12	.04	---
$\psi$ (deg)	$\beta$ (deg)	Average Value of $u'' /  \vec{V}_g $						
01-45	06-70	.59	.32	.15	.04	.00	.00	---
46-90	71-112	.67	.40	.23	.07	.01	.00	---
91-135	113-142	.70	.46	.25	.05	-.01	-.01	---
136-180	143-168	.71	.47	.26	.03	-.01	.00	---
181-225	169-190	.72	.49	.32	.06	.00	.00	---
226-270	191-230	.80	.57	.36	.06	.01	.01	---
271-315	231-297	.76	.52	.30	.04	.00	-.01	---
316-360	298-05	.62	.33	.15	.03	.00	.00	---
$ \vec{V}_T /S < .2$		.69	.44	.27	.04	-.01	-.01	---

Table 4.4

Average values of the geostrophic wind speed, and the normalized ageostrophic wind components for eight categories of  $\psi$  (or  $\beta$ ) and for conditions with negligible thermal winds. Time 12 Z.

		Height (millibars above surface)						
		0	25	50	100	150	200	250
$\psi$ (deg)	$\beta$ (deg)	Average Geostrophic Wind Speed - $ \vec{V}_g $ (m/sec)						
01-45	08-72	8.4	9.2	9.9	11.4	13.0	14.5	16.0
46-90	73-115	9.9	10.4	10.9	11.8	12.8	13.7	14.6
91-135	116-142	11.8	11.8	11.9	11.9	11.9	12.0	12.0
136-180	143-167	12.2	11.9	11.6	11.1	10.5	9.9	9.3
181-225	168-192	11.6	11.3	11.0	10.3	9.7	9.0	8.3
226-270	193-232	10.5	10.8	11.1	11.6	12.2	12.7	13.2
271-315	233-300	8.6	9.4	10.4	11.9	13.6	15.2	16.9
316-360	301-07	7.0	8.1	9.2	11.5	13.6	15.9	18.0
$ \vec{V}_T /S < .2$		10.3	10.5	10.7	11.1	11.6	12.0	12.4
$\psi$ (deg)	$\beta$ (deg)	Average Value of $v'' /  \vec{V}_g $						
01-45	08-72	.24	.26	.16	.00	-.02	-.01	---
46-90	73-115	.22	.21	.14	.00	-.05	-.02	---
91-135	116-142	.22	.25	.20	.04	-.03	-.02	---
136-180	143-167	.25	.28	.21	.05	-.02	-.05	---
181-225	168-192	.28	.29	.20	.00	-.03	-.01	---
226-270	193-232	.31	.31	.19	.00	-.03	-.02	---
271-315	233-300	.35	.32	.19	-.03	-.02	.00	---
316-360	301-07	.36	.30	.16	-.04	-.03	-.01	---
$ \vec{V}_T /S < .2$		.27	.26	.18	.00	-.03	-.01	---
$\psi$ (deg)	$\beta$ (deg)	Average Value of $u'' /  \vec{V}_g $						
01-45	08-72	.63	.13	-.12	-.16	-.08	-.01	---
46-90	73-115	.67	.23	-.08	-.17	-.08	-.04	---
91-135	116-142	.69	.30	-.01	-.16	-.08	-.02	---
136-180	143-167	.70	.30	-.02	-.17	-.09	-.03	---
181-225	168-192	.66	.24	-.07	-.17	-.10	.00	---
226-270	193-232	.66	.23	-.04	-.11	-.05	-.01	---
271-315	233-300	.65	.19	-.06	-.13	-.05	-.03	---
316-360	301-07	.59	.12	-.13	-.12	-.05	-.01	---
$ \vec{V}_T /S < .2$		.66	.23	-.06	-.15	-.08	-.02	---

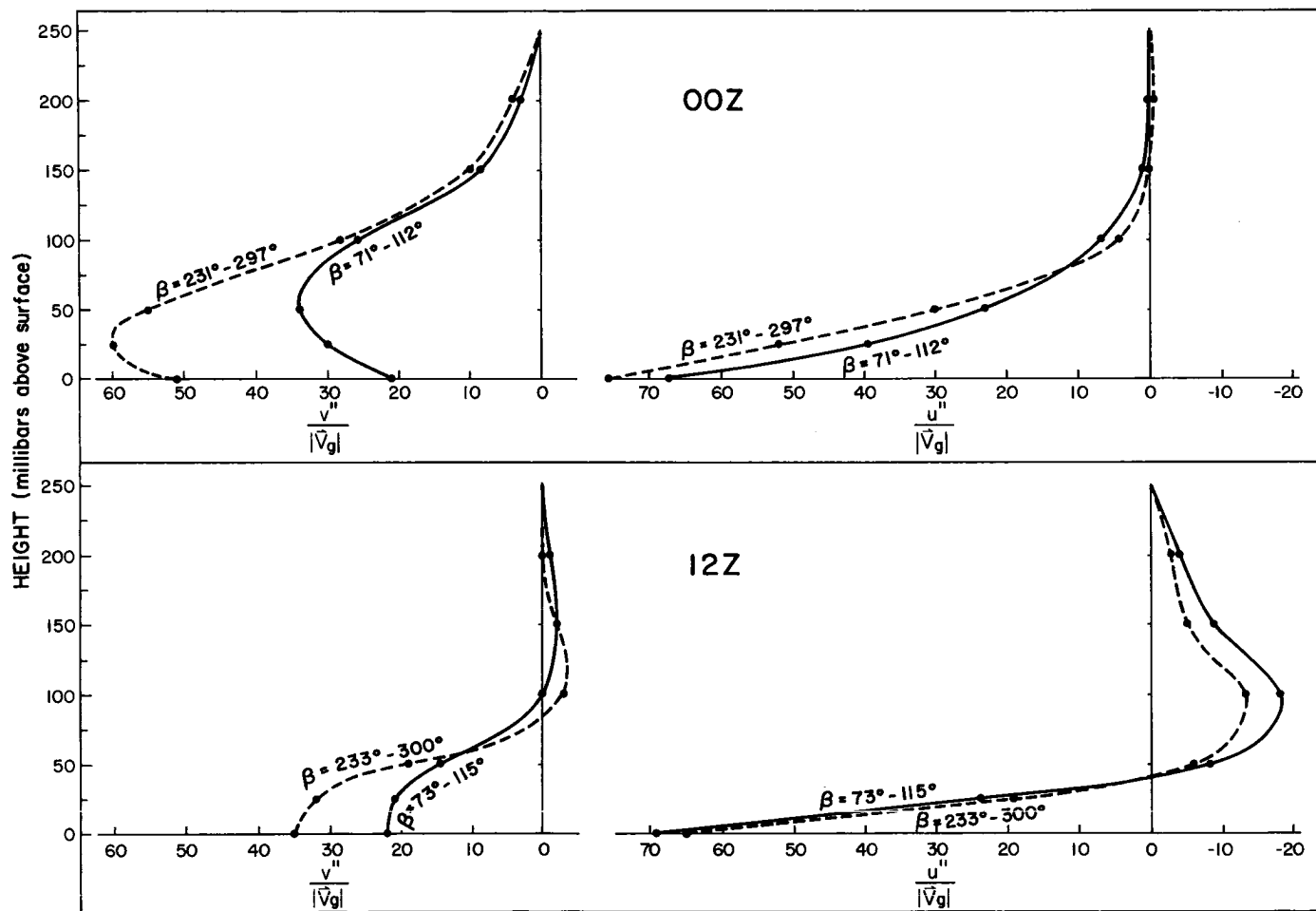


Fig. 4.8. Comparison of the normalized ageostrophic wind components for cases of warm and cold air advection.

Variations in Surface Stress. Assuming no accelerations, the equation of motion in pressure coordinates for the wind components along and perpendicular to the surface geostrophic wind can be written as:

$$fv_n - g \frac{\partial z}{\partial s} - g \frac{\partial \tau_{zs}}{\partial p} = 0 \quad (4.3)$$

$$-fu_s - g \frac{\partial z}{\partial n} - g \frac{\partial \tau_{zn}}{\partial p} = 0, \quad (4.4)$$

where the positive  $s$  axis coincides with the direction of the surface geostrophic wind and  $u_s$  and  $v_n$  are the wind components parallel and perpendicular to the  $s$  axis. In component form, the geostrophic wind relationship is:

$$g \frac{\partial z}{\partial s} = fv_{ng} \quad (4.5)$$

$$g \frac{\partial z}{\partial n} = -fu_{sg}. \quad (4.6)$$

Substituting (4.5) and (4.6) into (4.3) and (4.4), respectively, and rearranging we have,

$$\frac{\partial \tau_{zs}}{\partial p} = \frac{f}{g} (v_n - v_{n_g}) \quad (4.7)$$

$$\frac{\partial \tau_{zn}}{\partial p} = \frac{f}{g} (u_{s_g} - u_s) . \quad (4.8)$$

Integrating from the surface to a level where the stress becomes negligible, we obtain the geostrophic departure formulation for computing the surface stress. Assuming the stress is zero, 250 mb above the surface, the computational expression for the components of the surface stress are:

$$\tau_{zs_0} = -\frac{f}{g} \int_{p_0}^{p_0-250 \text{ mb}} (v_n - v_{n_g}) dp \quad (4.9)$$

$$\tau_{zn_0} = \frac{f}{g} \int_{p_0}^{p_0-250 \text{ mb}} (u_s - u_{s_g}) dp \quad (4.10)$$

The assumption of no accelerations is not valid for the individual observations. Eqs. (4.9) and (4.10) are applied to average values,

however. We assume that the accelerations produced by moving synoptic systems are largely eliminated in the averaging process.<sup>1</sup>

Values of  $\tau_{zs_0}$ ,  $\tau_{zn_0}$  and  $\bar{\tau}_{z_0}$  were computed for 00Z for each of the nine thermal wind categories using the data combinations given in Table 4.1. The resulting values are given in Table 4.5. To demonstrate the dependence of the stress on the angle  $\beta$ , the values have been normalized by dividing by the average surface geostrophic wind speed. These ratios are also listed in Table 4.5.

The effect of the thermal wind in modifying the stress in the PBL is demonstrated in Fig. 4.9. The variations in the ratios of surface stress to surface geostrophic wind speed are shown as a function of the angle  $\beta$ . Note the similarity between the curve for  $\tau_{zn_0} / |\bar{V}_{g_0}|$  and the curve for  $\alpha_0$  given by Fig. 4.7. The minimum value of  $\tau_{zs_0} / |\bar{V}_{g_0}|$  is found at  $\beta \approx 180^\circ$ , while the maximum value is near  $325^\circ$ . These angles correspond closely to conditions with the thermal wind opposing ( $\beta \approx 180^\circ$ ) and increasing ( $\beta \approx 325^\circ$ ) the surface wind vector. Combining the stress components gives rise to significantly larger ratios of  $\bar{\tau}_{z_0} / |\bar{V}_{g_0}|$  for cold air advection conditions.

Variations in Surface Speed. Table 4.6 lists the average surface wind speeds at 00Z for the nine thermal wind categories. Also included are the values of the normalized quantity  $|\bar{V}_0| / |\bar{V}_{g_0}|$ . The averages

---

<sup>1</sup>It will be shown in Chapter 5 that at 12Z much of the ageostrophic flow in the lowest 2 km is related to inertial motions. The accelerations associated with the inertial motion are systematic. Therefore, the geostrophic departure method cannot be used to compute the surface stress at 12Z.

Table 4.5

Average values of the surface stress and components of surface stress for 00Z. Included are ratios of the stress values to the average surface geostrophic wind speed.

	$\beta$ (degrees)								Negligible Thermal Winds
	06-70	71-112	113-142	143-168	169-190	191-230	231-297	298-05	
$\tau_{zS_o}$ (dynes/cm <sup>2</sup> )	5.2	6.2	6.6	6.5	5.9	5.2	6.3	6.5	6.6
$\tau_{zn_o}$ (dynes/cm <sup>2</sup> )	2.0	2.4	3.8	4.5	6.6	9.2	6.4	2.9	3.8
$\tau_{z_o}$ (dynes/cm <sup>2</sup> )	5.6	6.7	7.6	7.9	8.9	10.5	9.0	7.1	7.6
$\tau_{zS_o} /  \vec{V}_{g_o} $ ( $\frac{\text{dynes/cm}^2}{\text{m/sec}}$ )	.57	.51	.46	.44	.41	.41	.64	.83	.54
$\tau_{zn_o} /  \vec{V}_{g_o} $ ( $\frac{\text{dynes/cm}^2}{\text{m/sec}}$ )	.22	.20	.26	.31	.46	.72	.65	.37	.31
$\tau_{z_o} /  \vec{V}_{g_o} $ ( $\frac{\text{dynes/cm}^2}{\text{m/sec}}$ )	.62	.55	.53	.54	.62	.82	.92	.91	.62

Table 4.6

Average values of  $|\vec{V}_o|$  and  $|\vec{V}_o| / |\vec{V}_{g_o}|$  for the nine thermal wind categories.

	$\beta$ (degrees)								Negligible Thermal Winds
	06-70	71-112	113-142	143-168	169-190	191-230	231-297	298-05	
$ \vec{V}_o $	4.6	4.8	5.3	5.6	5.8	6.2	5.7	5.2	5.4
$ \vec{V}_o  /  \vec{V}_{g_o} $	.51	.40	.37	.38	.41	.48	.58	.67	.44

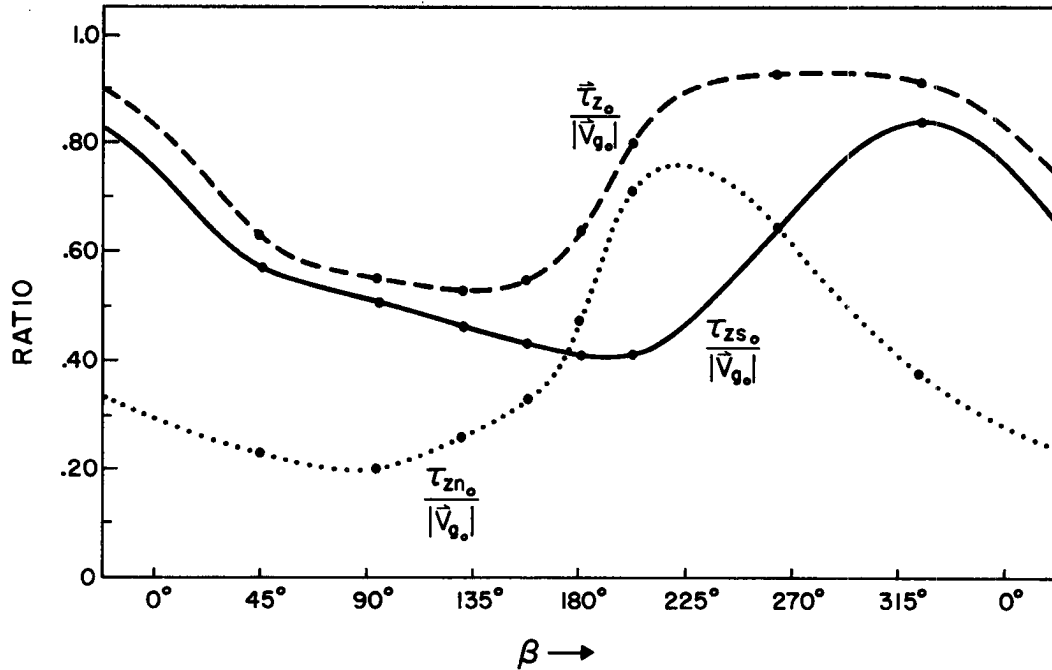


Fig. 4.9. Normalized values of the surface stress at 00Z as a function of the angle between the surface geostrophic wind and the thermal wind in the lowest 100 mb. The units are in  $(\text{dynes/cm}^2) / (\text{m/sec})$ .

were obtained from the data combinations listed in Table 4.1.

The curve of  $|\vec{V}_o| / |\vec{V}_{g_o}|$  vs.  $\beta$  is shown in Fig. 4.10. Note that the variations are very similar to the variations of  $\vec{\tau}_{z_o} / |\vec{V}_{g_o}|$  presented in Fig. 4.9. Indeed, these curves should be similar if the geostrophic departure method and drag coefficient method for computing surface stress are to yield comparable values. (The formulation for the drag coefficient method is  $\vec{\tau}_{z_o} = \rho C_d (\vec{V}_o)^2$  where  $C_d$  bulk drag coefficient).

Interpretation of Results. The amount of mechanical turbulence near the surface is determined primarily by the magnitude of the flow near the surface and the roughness characteristics of that surface.

To a large extent, the vertical distribution of the turbulence is

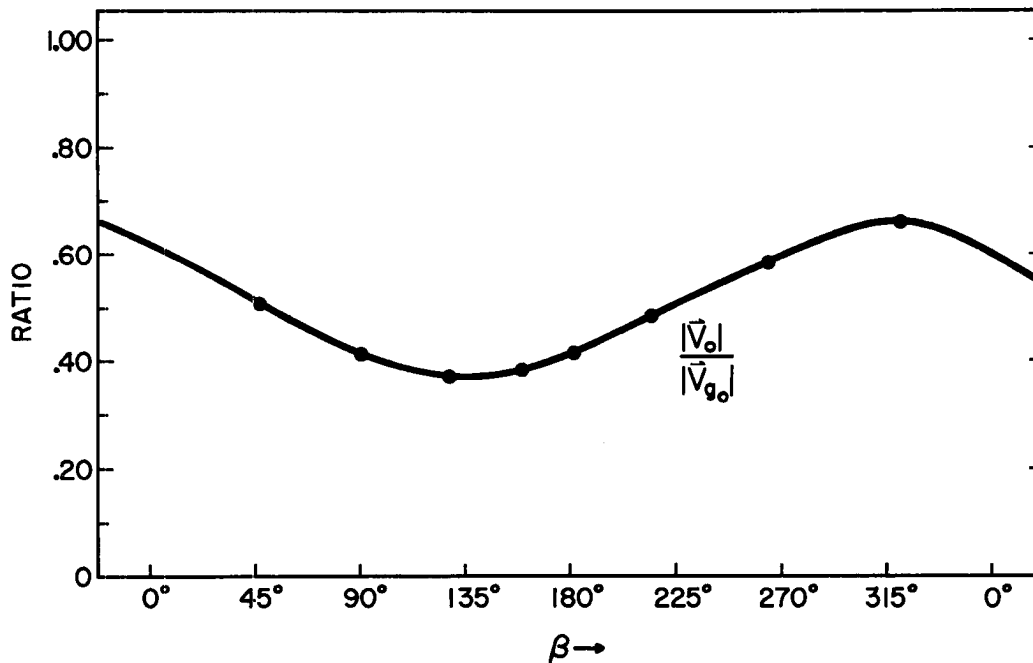


Fig. 4.10. Normalized values of the surface wind speed as a function of the angle between the surface geostrophic wind and the thermal wind in the lowest 100 mb.

determined by the thermal stratification. Mixing length theory states that the vertical momentum transport is proportional to the shear of the horizontal wind vector. When geostrophic shear exists in the PBL, the vertical momentum transport is modified from that expected in barotropic conditions. This modifies the stress profile as shown in Fig. 4.9. This in turn modifies the mean wind profiles in the lower layers.

The mechanism is portrayed schematically in Fig. 4.11. Examples are shown for (a) warm air advection — ( $\beta = 70^\circ$ ) and (b) cold air advection — ( $\beta = 210^\circ$ ). In addition, examples are shown for cases of (c) the thermal wind blowing in the same direction as the surface geostrophic wind — ( $\beta = 0^\circ$ ), and (d) the thermal wind opposing the

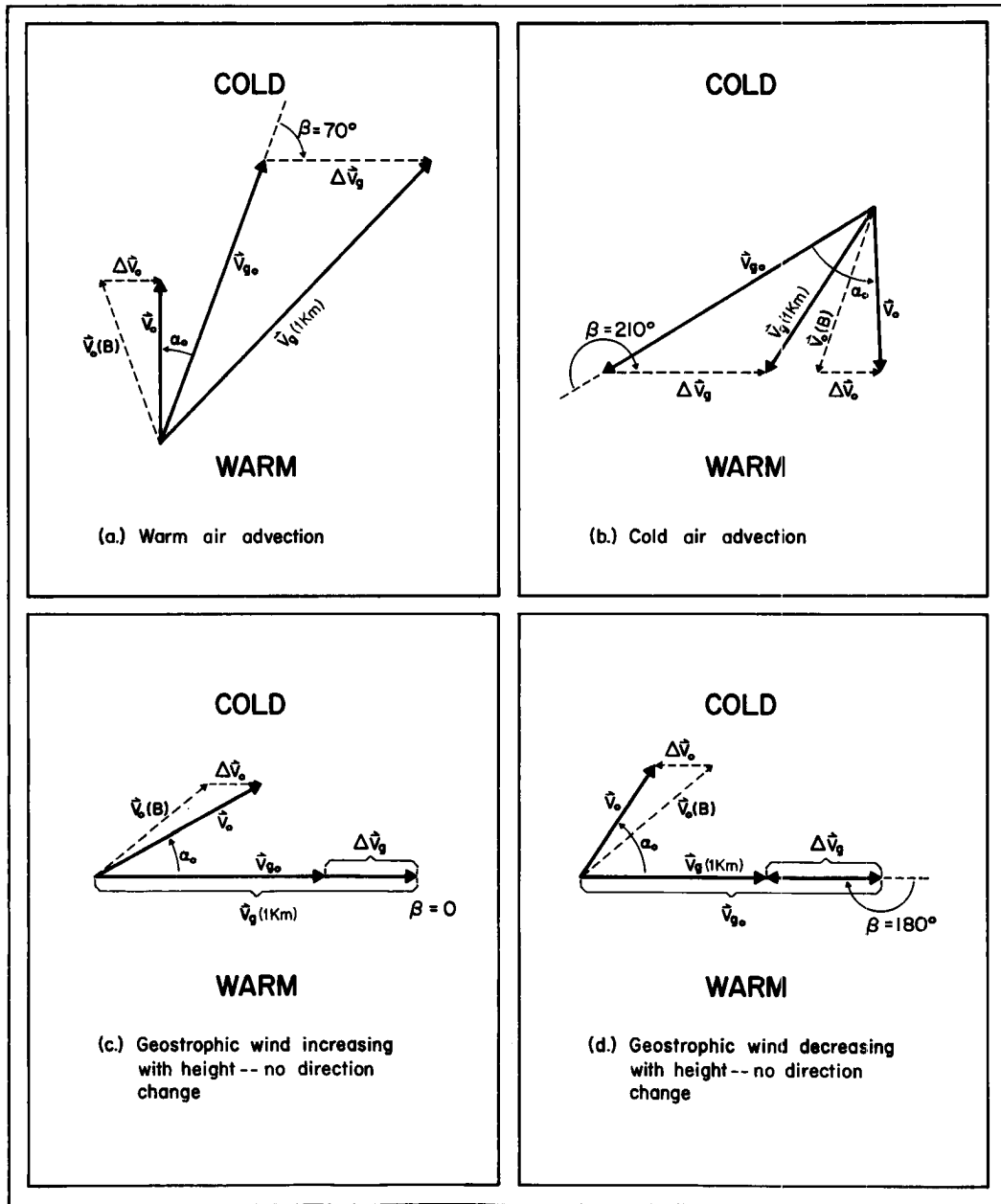


Fig. 4.11. Schematic examples of how the additional downward momentum transport, resulting from geostrophic shear in the turbulent boundary layer, modifies the surface veering angle from that expected in a barotropic atmosphere. ( $\vec{V}_O(B)$  is the surface wind which would exist in barotropic conditions;  $\Delta\vec{V}_g$  represents the geostrophic shear vector in the lowest kilometer;  $\vec{V}_O$  is the actual surface wind;  $\vec{V}_{g0}$  is the surface geostrophic wind;  $\vec{V}_g(1\text{ km})$  is the geostrophic wind at one kilometer; and  $\alpha_0$  is the angle between the surface wind and surface geostrophic wind.)

surface geostrophic wind — ( $\beta = 180^\circ$ ). In each case, the additional downward momentum transfer induced by the geostrophic shear is added schematically to the surface wind vector that would exist in a barotropic atmosphere. For  $\beta = 70^\circ$ , the additional momentum transported from above opposes the flow toward lower pressure in the region near the surface. The result is a smaller surface crossing angle and less ageostrophic flow towards lower pressure. When  $\beta = 210^\circ$  (cold air advection), the flow towards lower pressure is increased and  $\alpha_0$  becomes larger than the value for similar conditions in a barotropic atmosphere. Intuitively, it is expected that the greatest modification of  $\alpha_0$  occurs when the additional momentum transport is perpendicular to the surface wind vector that would exist in barotropic conditions. This is verified by Fig. 4.5.

In cases where  $\beta = 0^\circ$ , the effect is to increase the surface wind speed and slightly decrease the crossing angle. This would result in an increase of the surface stress in the direction of the surface geostrophic wind. When the thermal wind opposes the geostrophic wind vector, the result is a decreased value of the surface stress along the geostrophic wind and an increase in the surface crossing angle.

Sheppard, et al. (1952) were the first to suggest that this mechanism could modify the PBL wind profile. Recently, Blackadar (1965), MacKay (1971) and Cattle (1971) have developed theories expressing this effect quantitatively. For neutral conditions  $|\vec{V}_T| / S \approx .5$ , and  $z_0 = 1 \text{ cm}$ , Blackadar's model gave values of  $\alpha_0$  of  $18.4^\circ$ ,

17.7°, 26.3° and 26.8° for  $\beta$  equal to 0°, 90°, 180° and 270°, respectively. While these model variations in  $\alpha_0$  are in qualitative agreement with the present study, the amplitudes are much smaller than those given in Fig. 4.7. However, greater variations would be expected if the values of  $z_0$  were increased.

Cattle presented theoretical values of  $\alpha_0$  for  $\beta = 0^\circ, 90^\circ, 180^\circ$  and  $270^\circ$ . He showed large values of  $\alpha_0$  for  $\beta = 270^\circ$  and small values for  $\beta = 90^\circ$  when significant temperature gradients were assumed. He also found larger values of  $\alpha_0$  for  $\beta = 180^\circ$  as opposed to  $\beta = 0^\circ$ . Cattle's theoretical results are also in qualitative agreement with the observational results of the present study.

MacKay shows maximum and minimum values of  $\alpha_0$  at  $\beta = 135^\circ$  and  $315^\circ$ , respectively. This does not agree with Cattle's theoretical results or the observational results shown in Fig. 4.7. The phase angle between MacKay's curves and those in Fig. 4.7 is very near  $90^\circ$ . The explanation for this difference is not clear, but may result from MacKay's modeling the magnitude of the thermal wind as an exponential function decreasing with height as opposed to the more general case of the magnitude being approximately constant with height.

#### 4.3 The Role of Geostrophic Shear in Selected Atmospheric Processes

Movement of Cold Air Masses. The effects just described can frequently be observed in synoptic analysis. Fig. 4.12 provides a good example. Here the surface analysis over the Eastern

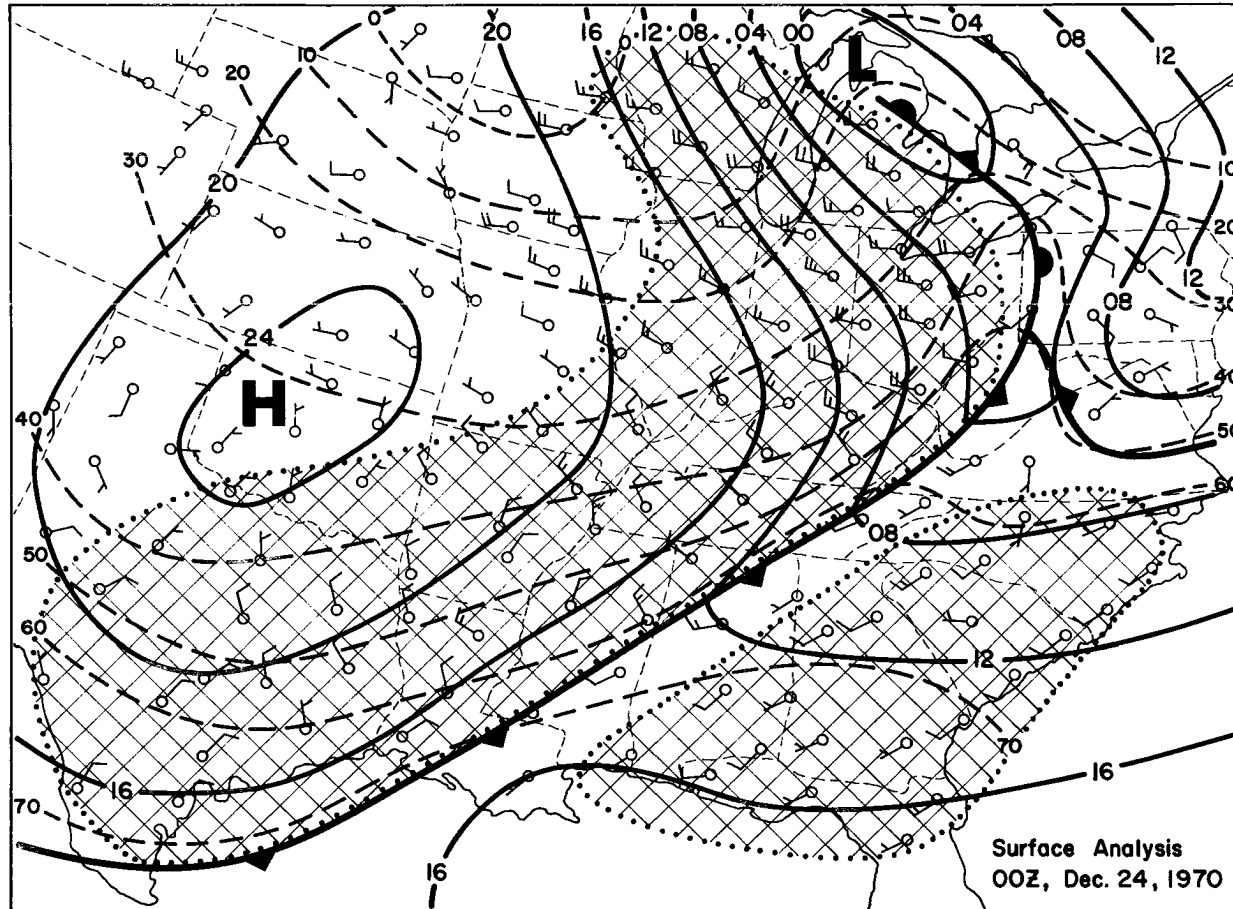


Fig. 4.12. Surface analysis showing the modification of the angle between the surface winds and surface isobars. Surface pressure in millibars (only the last two digits are plotted) is given by the solid lines. The temperature field ( $^{\circ}\text{F}$ ) is given by the dashed lines. The observed winds are plotted for each station. In the stippled area behind the cold front the average value of  $\alpha_{\circ}$  is  $60^{\circ}$ . In the stippled area ahead of the cold front the average value of  $\alpha_{\circ}$  is  $33^{\circ}$ .

United States for 00Z, December 24, 1970, is shown. A strong cold front is advancing through the area. The region of cold air advection is indicated by the stippled area behind the cold front. In this region, the value of  $\beta$  as given by the angle between the isobars and surface isotherms is between  $200^\circ$  and  $270^\circ$ . The average value of  $\alpha_0$  is  $60^\circ$ . Ahead of the front there is an area of weak warm air advection indicated in a second stippled area. In this region, the values of  $\beta$  range from  $0^\circ$ - $50^\circ$  and the average value of  $\alpha_0$  is  $33^\circ$ .

The momentum transport initiated by the geostrophic shear in the strong baroclinic zones behind cold fronts results in an increase in the cold air advection at the surface. This allows the air to flow almost directly away from the center of the cold anticyclones. The cold air then moves very rapidly eastward and southward (in the Northern Hemisphere) allowing little time for air mass modification.

Transport of Angular Momentum. Conservation of angular momentum arguments lead to the fact that westerly momentum must be transported from the atmosphere to the earth in mid-latitudes. This obviously is the case in regions where the average surface geostrophic winds are from the west. However, in much of the Northern Hemisphere, the synoptic pressure systems are cellular. Alternating high and low pressure systems move across a region and the resultant surface geostrophic wind may have a negligible westerly component.

Fig. 4.13 shows such a pattern in schematic form. Here the typical case of a sinusoidal temperature field existing in a cellular pressure

magnitude of the thermal wind in the PBL relative to the direction and magnitude of the surface geostrophic wind. The effect is to increase (decrease) the ageostrophic wind components towards lower pressure in cold (warm) air advection. In conditions with a basic north-south temperature gradient, the geostrophic shear produces a systematic transport of westerly angular momentum from the atmosphere to the earth's surface. This increases the westerly component of the average surface wind.

## 5. EFFECTS OF STABILITY ON PLANETARY BOUNDARY LAYER WIND PROFILES

This study was designed to investigate two different aspects of the relationship between the characteristics of the PBL wind profile and stability changes. Section 5.1 presents results showing the general changes in the wind profile. Qualitative relationships based on these results are considered valid when the stability of the lowest 1-2 km is constant or changing slowly.

Section 5.2 is devoted to diurnal changes in stability. Typically, these changes are large and occur rapidly. Observed diurnal variations in the wind profiles are presented. A qualitative model is then developed to explain the observed variations.

### 5.1 General Effects of Stability

Variations in Wind Veering. Fig. 5.1 shows the average veering profiles for three stability categories. The results are taken from Stratification B (five speed, three stability, and nine baroclinicity categories -- geostrophic shear eliminated from the wind data). The same categories of speed and thermal wind are included for each lapse rate category (see Table 5.1). These profiles were obtained by weighting the average veering values for each combination equally. This eliminated the variations not related to changes in stability.

At both 00Z and 12Z, the surface crossing angle ( $\alpha_0$ ) increases with increasing stability. At elevations greater than 50 mb above the surface, the trend reverses. Here the veering angles decrease with

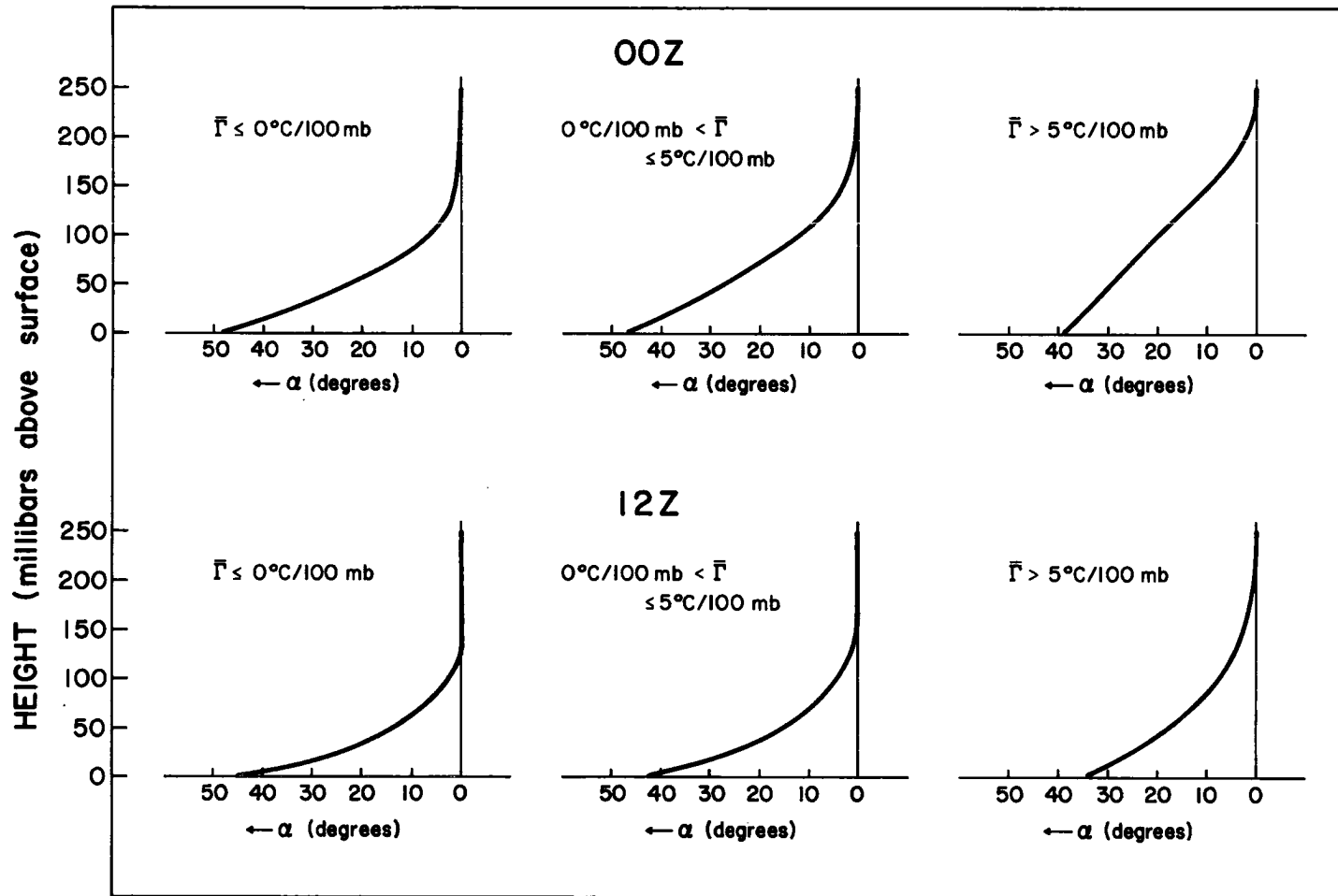


Fig. 5.1. Angle between wind and isobars versus height for three stability categories.

Table 5.1

Combinations of categories from Stratification B which were used to obtain the values shown in Fig. 5.1. The number of observations is given for each combination. In obtaining average values for each stability category the combinations were weighted equally. (See Section 3.3 for a description of the categories.)

## Time 00Z

Categories		Thermal Wind Categories								
Speed	Stability	1	2	3	4	5	6	7	8	9
2	1	97	148	93	51	19	22	45	58	52
3		44	73	64	22	7	6	11	29	59
2	2	223	232	205	171	122	134	201	255	181
3		92	95	88	46	32	40	63	90	235
2	3	310	198	165	204	203	228	457	625	398
3		135	62	61	99	58	64	237	336	405

## Time 12Z

Categories		Thermal Wind Categories								
Speed	Stability	1	2	3	4	5	6	7	8	9
2	1	334	323	245	163	147	237	334	428	336
3		158	124	98	47	34	61	115	166	338
2	2	169	123	85	99	156	232	363	322	239
3		120	52	37	36	68	88	160	187	362
2	3	23	5	3	13	36	78	211	126	69
3		14	4	4	7	17	78	153	123	142

increasing stability. Therefore, the depth of the layer of geostrophic flow towards lower pressure decreases with increasing stability.

The results of Stratification C (detailed lapse rate Stratification) are shown in Figs. 5.2 - 5.5 (Fig. 5.2 - winter 00Z; Fig. 5.3 - winter 12Z; Fig. 5.4 - summer 00Z; Fig. 5.5 - summer 12Z). Adjacent to each veering profile is a plot of the average change of potential temperature ( $\theta - \theta_0$ ) with height in the lowest 150 mb. The diagrams are arranged in order of decreasing stability. Obviously, if  $\theta - \theta_0$  is constant, the lapse rate is equal to the dry adiabatic lapse rate. Isothermal lapse rates correspond to increases of about  $9^\circ\text{C}/100\text{ mb}$ . The four numbers separated by commas indicate the lapse rate categories for Stratification C (as defined in Section 3.3). The first number is the stability category for the lowest 25 mb layer; the second for the layer 25-50 mb above the surface; the third for the layer 50-100 mb above the surface; and the fourth for the layer 100-150 mb above the surface. Immediately above the category indicator is the number of observations with the indicated lapse rates. With the exception of combination (3, 3, 3, 3) for 12Z during the winter season, only those combinations with a data sample greater than 50 are shown.

In Fig. 5.2, the 00Z profiles indicate values of  $\alpha_0$  near  $50^\circ$  for very stable conditions and near  $30^\circ$  for the conditions where  $\frac{\partial\theta}{\partial z} \approx 0$ . The profiles also show a gradual increase in the height at which  $\alpha$  approaches zero as the lowest 150 mb becomes less stable. However, 12Z profiles (making up Fig. 5.3) show no systematic variation of  $\alpha_0$

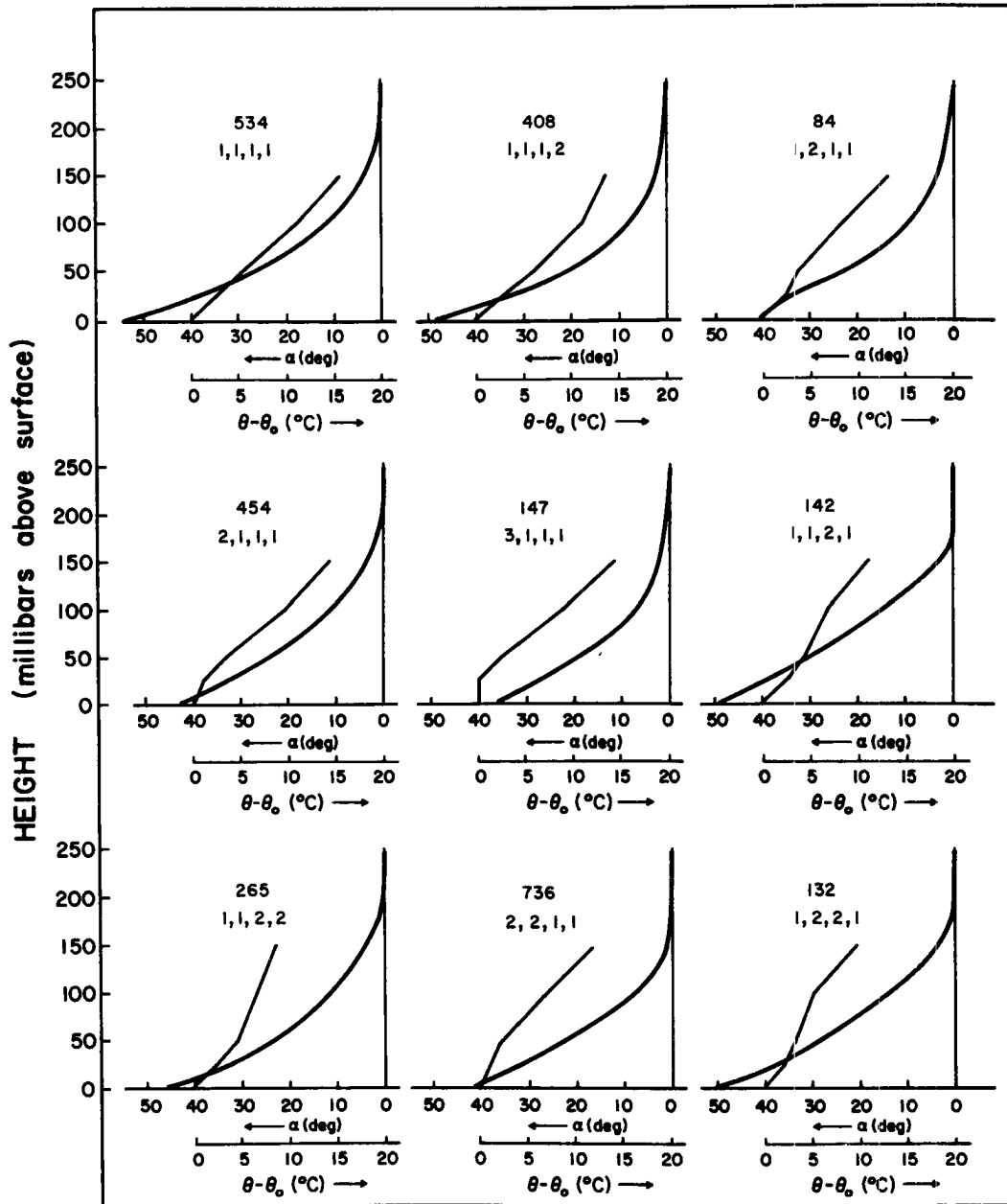


Fig. 5.2. Veering angle as a function of height for various lapse rate profiles. Time-00Z; Season-Winter.

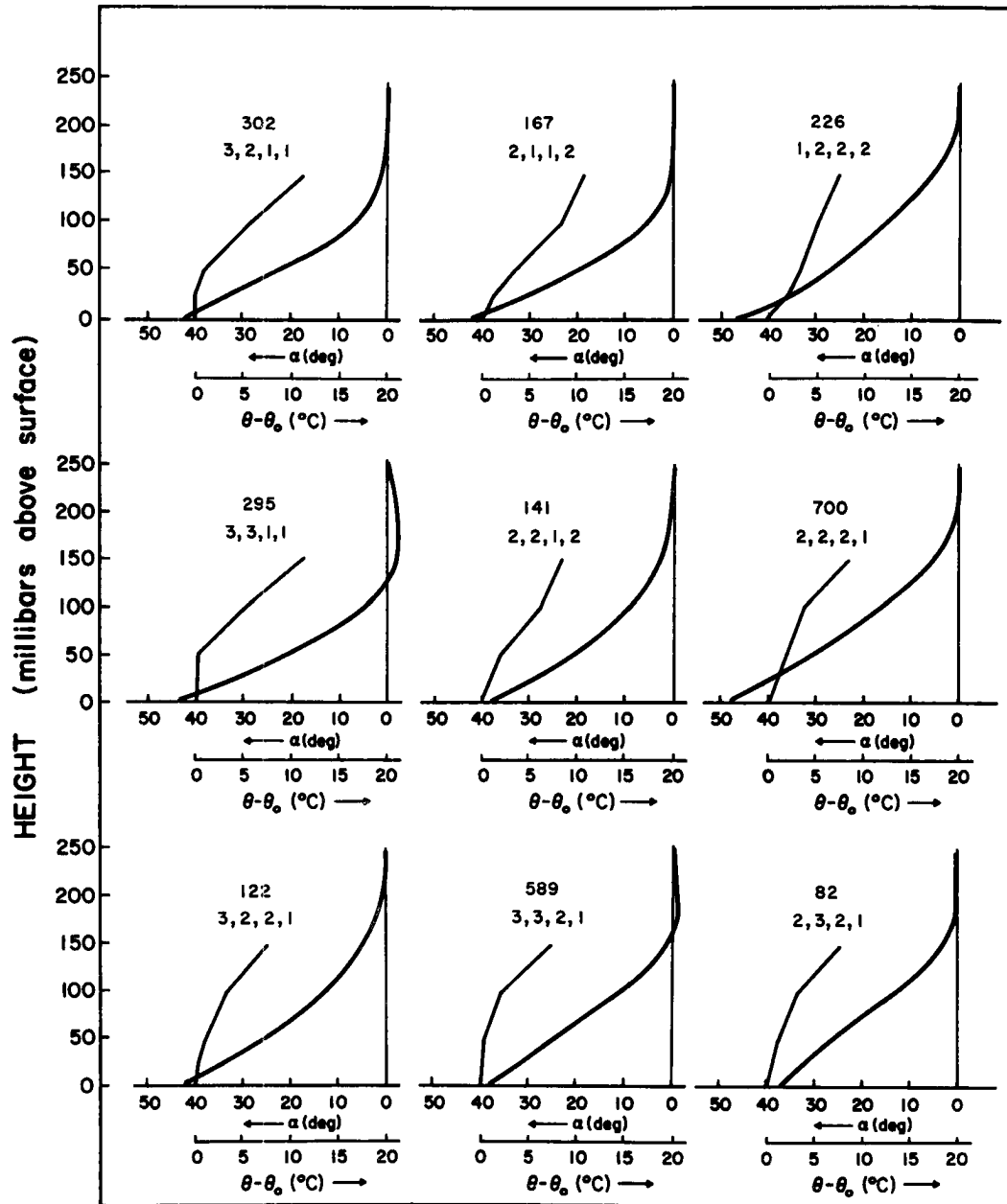


Fig. 5.2. (Continued)

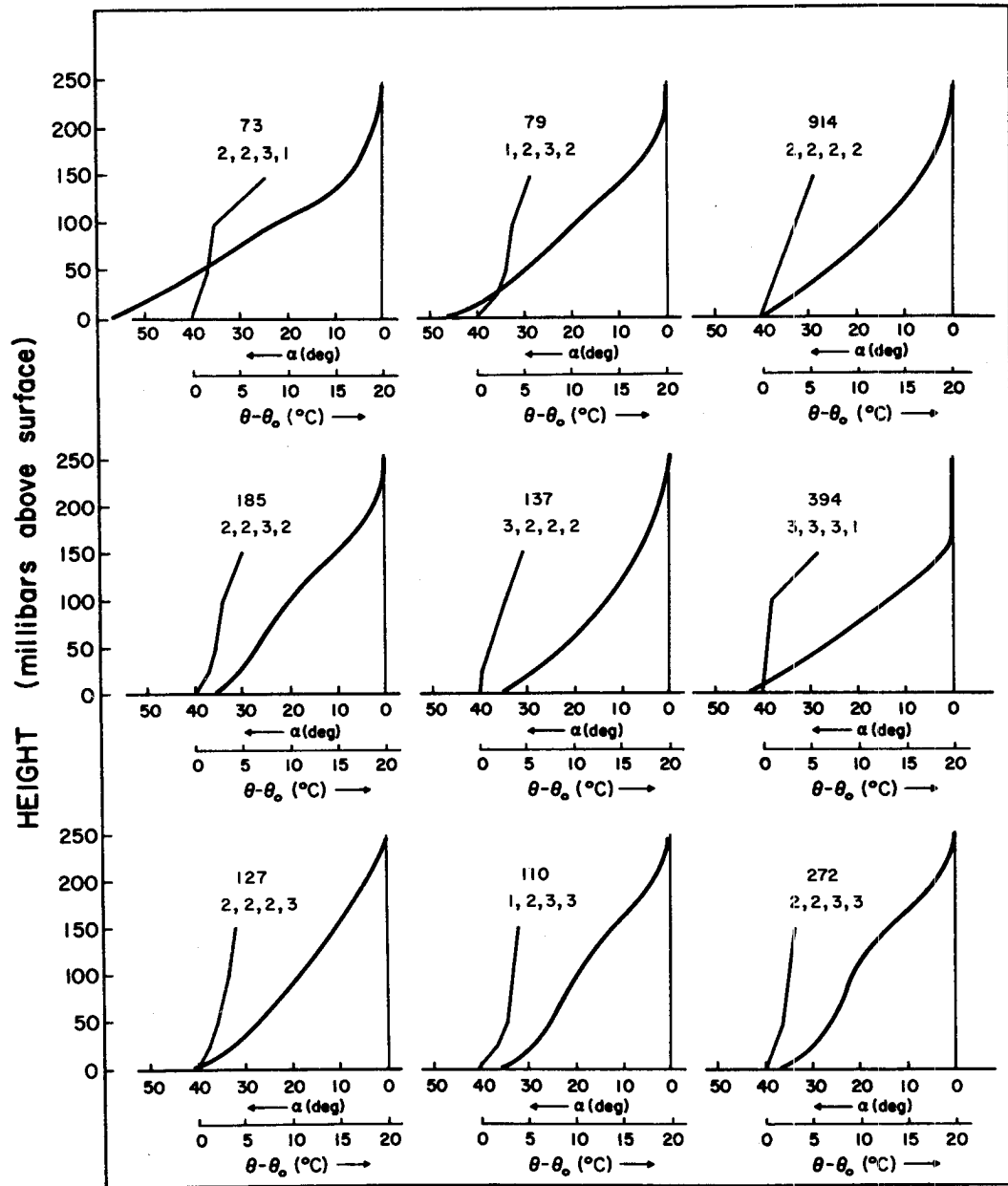


Fig. 5.2. (Continued)

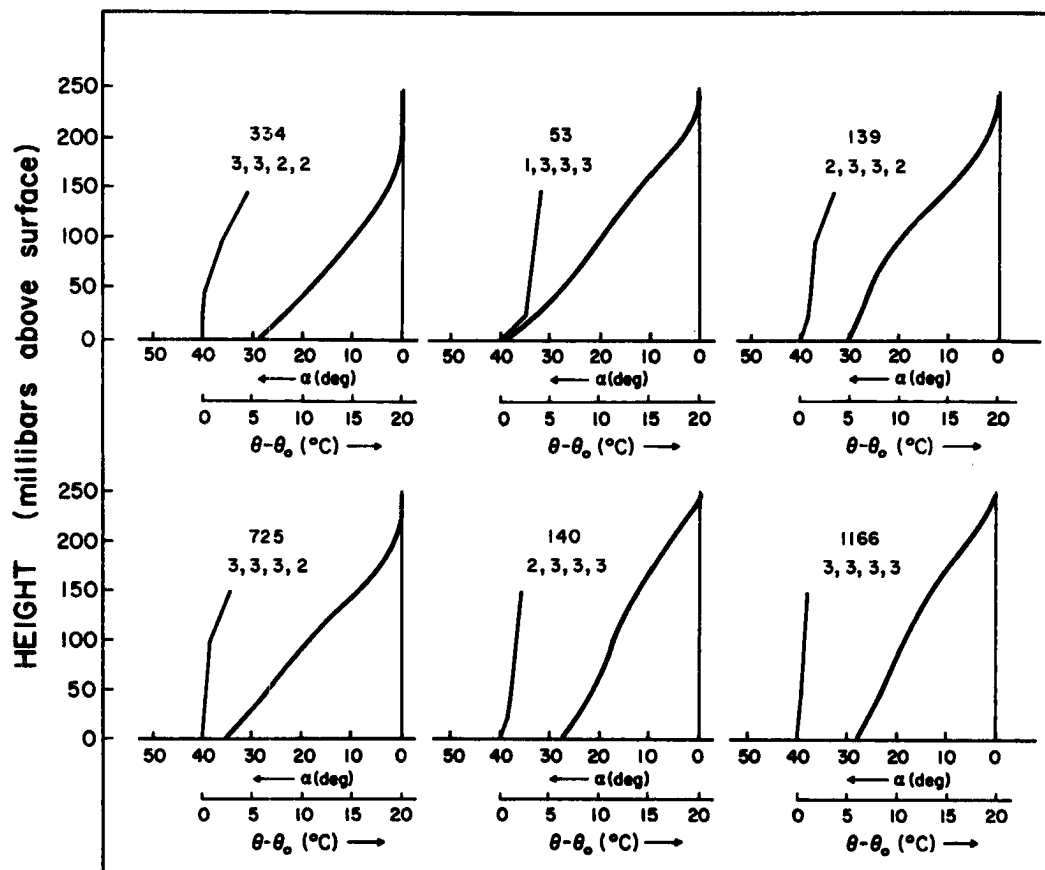


Fig. 5.2. (Continued)

with stability. But again the 12Z profiles suggest that the height at which  $\alpha$  becomes zero increases for the less stable situations.

During the summer months, synoptic changes are much weaker. Therefore, the diurnal cycle in the stability profiles becomes more evident. Figs. 5.4 and 5.5 confirm this statement. At 12Z ( $\approx 0600$  LT) all of the combinations with a sufficient data sample are stable. A majority of the observations indicate ground based inversions. At 00Z ( $\approx 1800$  LT), the reverse occurs with a majority of the observations being in the least stable combinations. The typical values of  $\alpha_0$  for

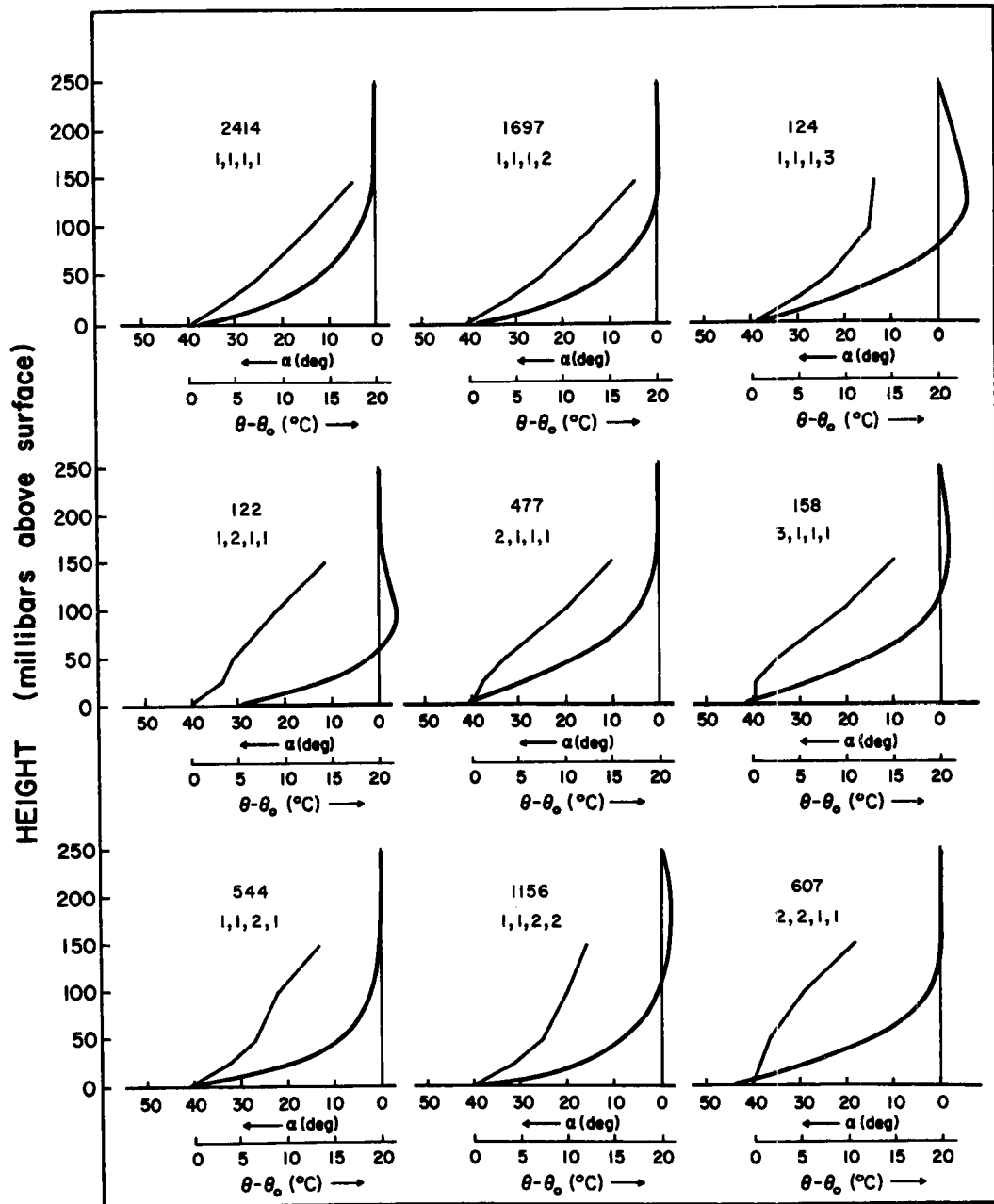


Fig. 5.3. Veering angle as a function of height for various lapse rate profiles. Time-12Z; Season-Winter.

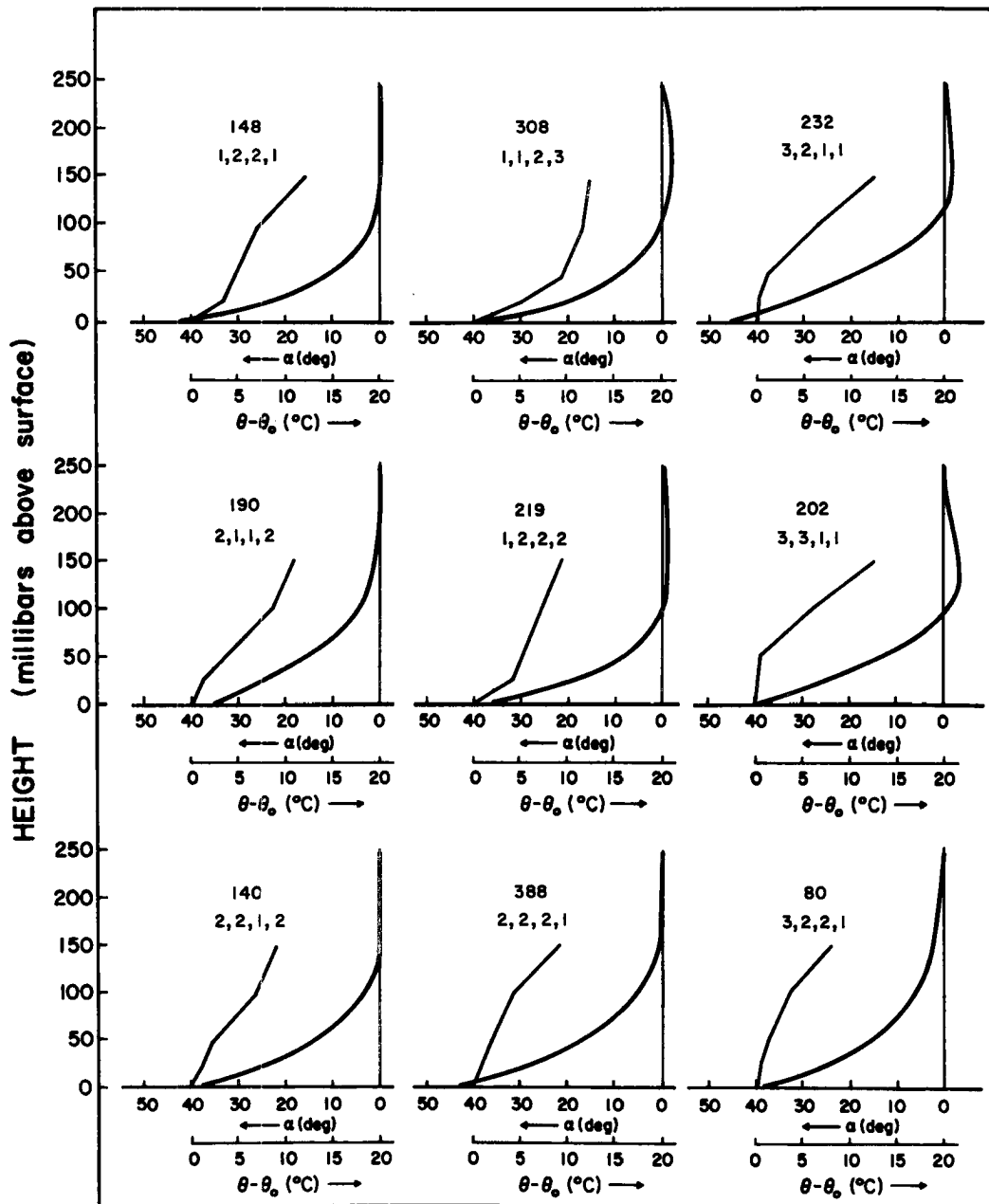


Fig. 5.3. (Continued)

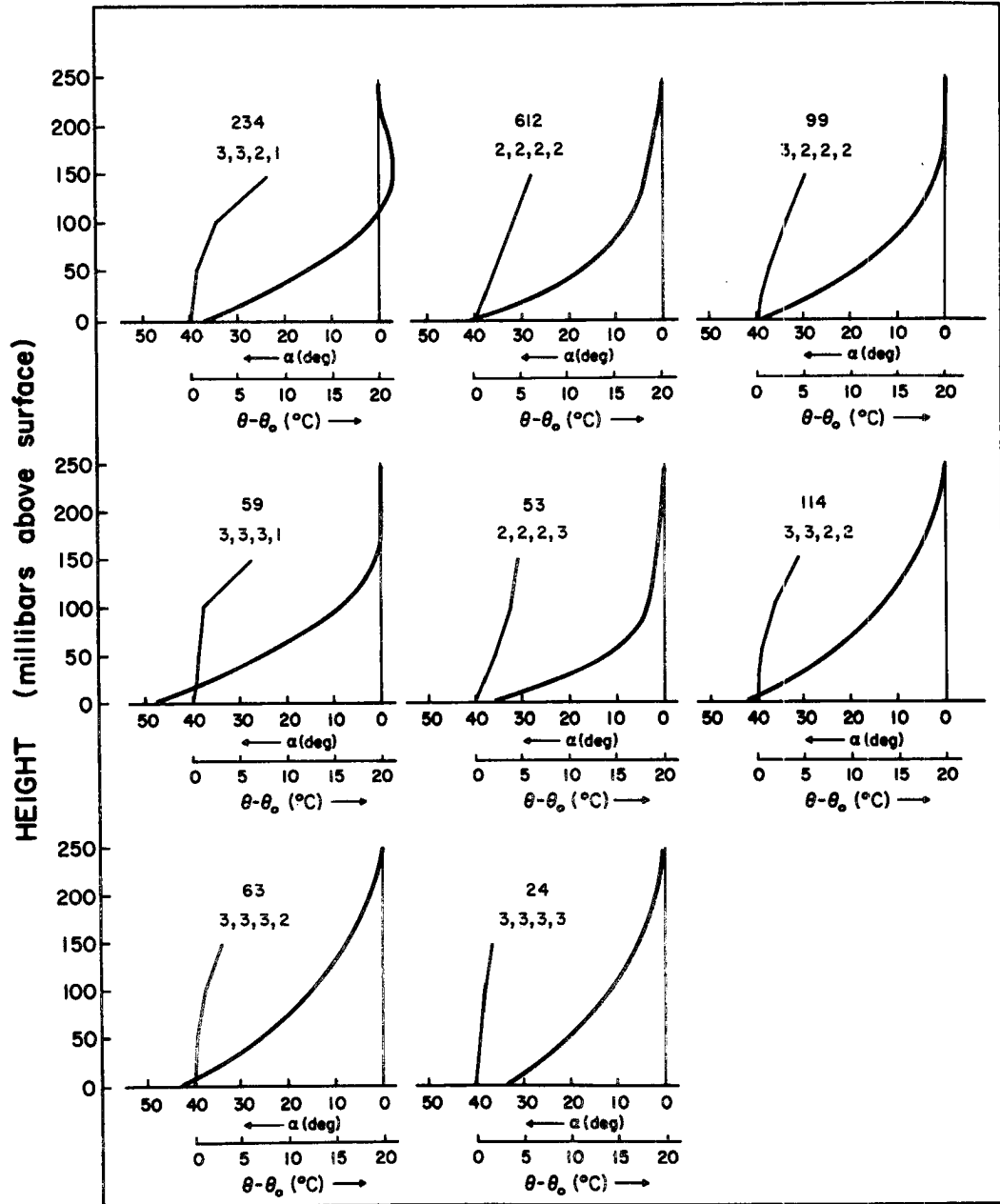


Fig. 5.3. (Continued)

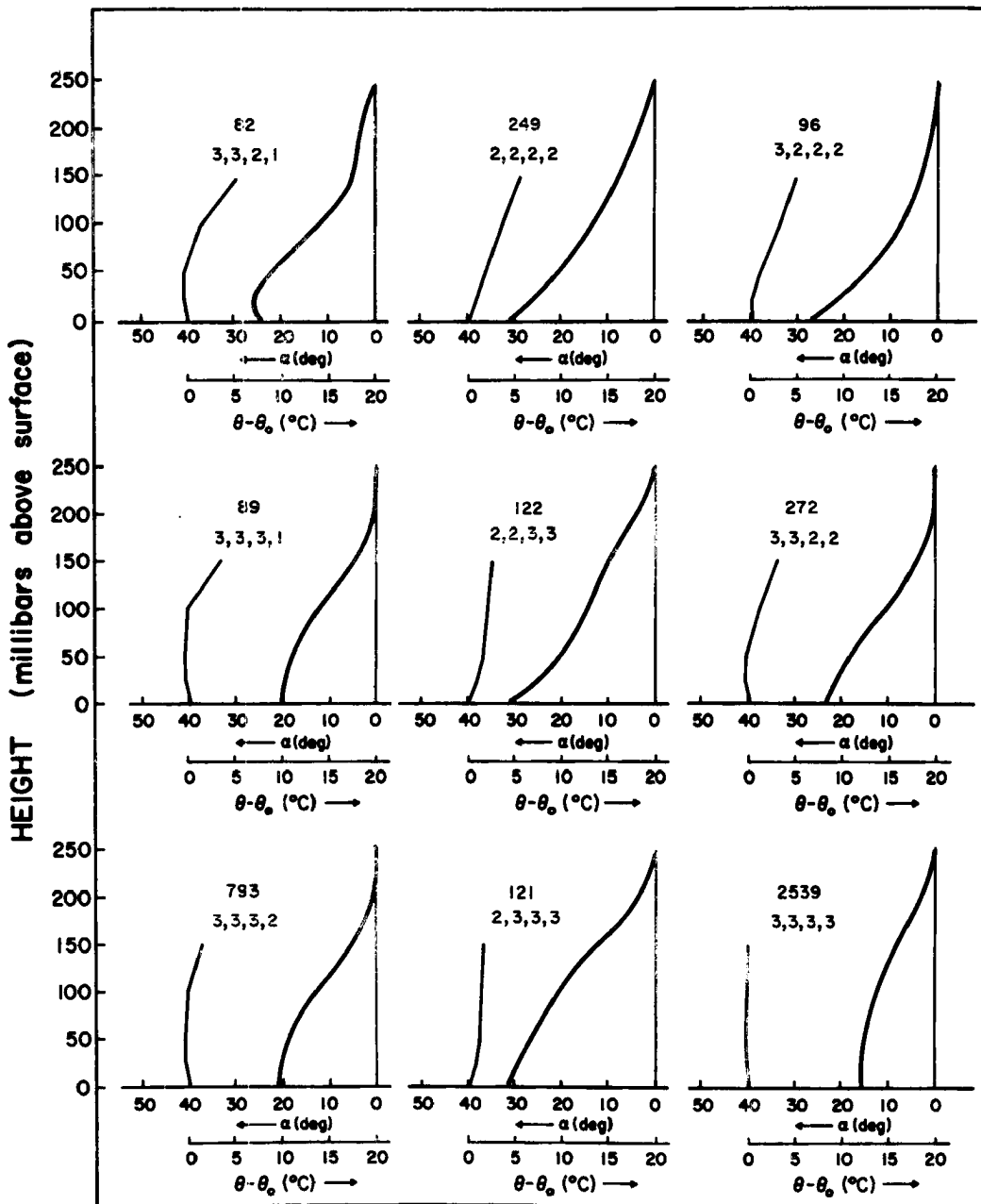


Fig. 5.4. Veering angle as a function of height for various lapse rate profiles. Time 00Z; Season-Summer.

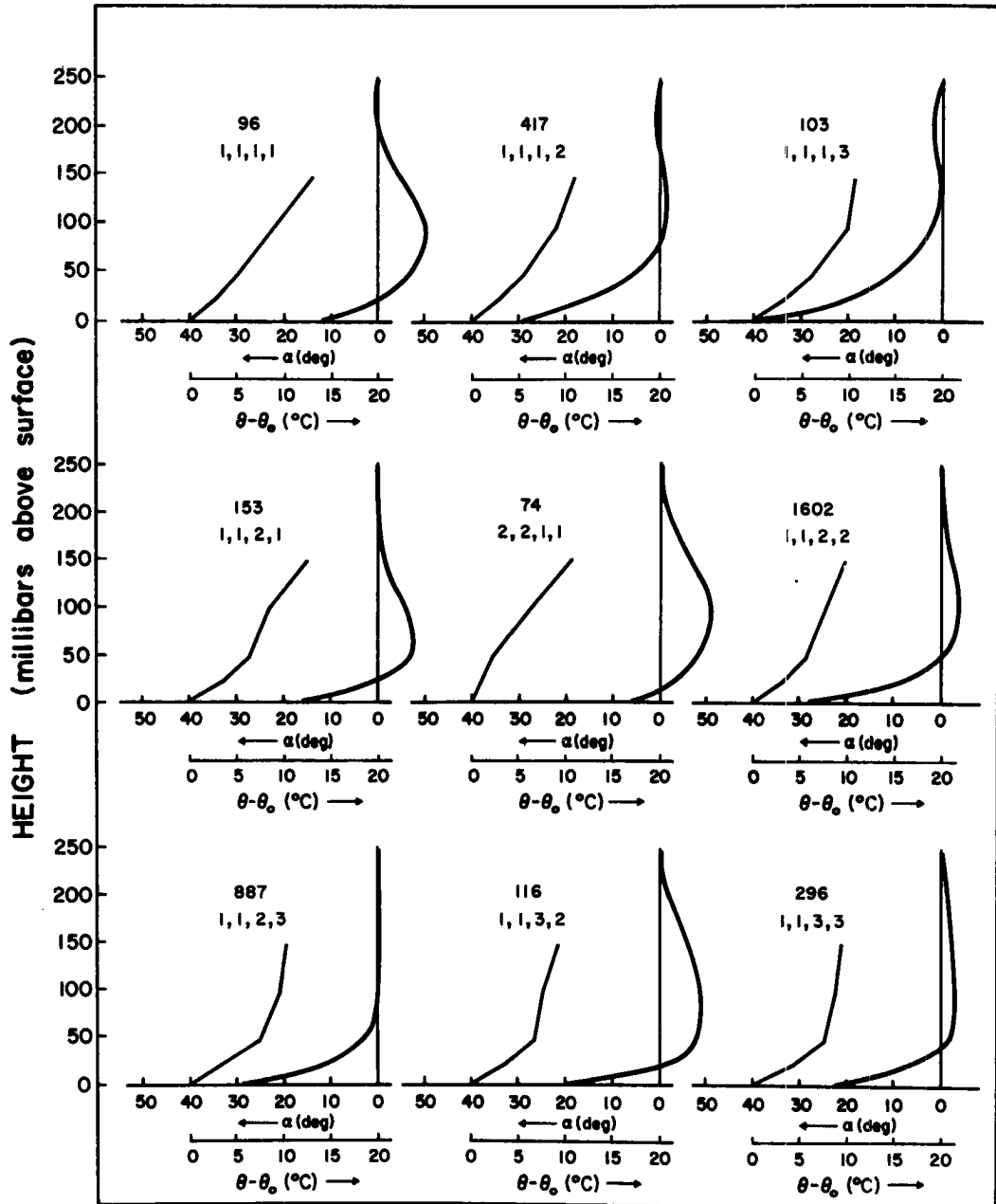


Fig. 5.5. Veering angle as a function of height for various lapse rate profiles. Time-12Z; Season-Summer.

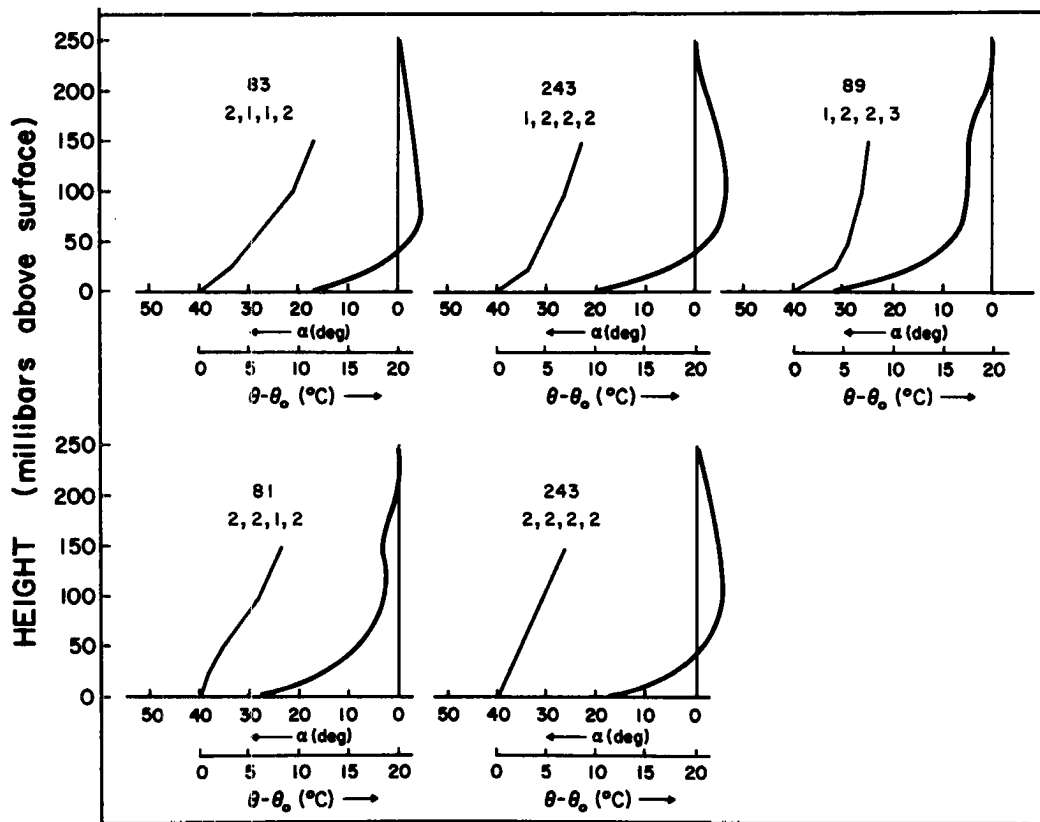


Fig. 5.5. (Continued)

the summer season are near  $25^\circ$  at 12Z and  $15-20^\circ$  at 00Z. These values are significantly smaller than the mean values for the winter season.

When comparing the 00Z and 12Z summer profiles, the difference in the level at which  $\alpha$  first becomes zero is very great. In the morning, the level is only 30-50 mb above the surface while in the late afternoon it is near 250 mb above the surface. Typical veering in the first 50 mb is near  $30^\circ$  at 12Z but only  $3-5^\circ$  at 00Z. Similar values for 12Z and 00Z were found by Mendenhall (1967) in an analysis of the surface - 950 mb veering at Shreveport, La.

The 12Z summer profiles show a definite tendency for the wind to back in the layer 100-200 mb above the surface. This results in negative veering values or flow towards higher pressure above the first 30-50 mb. This interesting feature is part of the diurnal variation and is treated in detail in the next section (Section 5.2).

Figs. 5.1 - 5.5 confirm the basic concept of the role of stability as outlined in Chapter 2. In stable conditions, the vertical propagation of mechanical turbulence is suppressed, allowing large vertical shears of the horizontal wind. The effects of surface friction are confined to the lowest few hundred meters. For unstable conditions, buoyancy induced turbulence aids in the vertical momentum transport. The large mixing rates act to destroy vertical wind shears resulting in a much deeper layer of ageostrophic winds and small changes of the wind veering with height.

Variations in Ageostrophic Winds. Table 5.2 lists several lapse rate combinations from Stratification C, selected to represent very stable, moderately stable and adiabatic conditions respectively. The normalized ageostrophic wind components for these conditions are given in Tables 5.3 and 5.4.

Stratification C does not include a speed parameterization. However, the average values of  $S$  (the average speed in the lowest 100 mb) were computed for each lapse rate combination. The variations in the ageostrophic components due to speed variations were eliminated by

applying corrections obtained from Tables 7.3 and 7.4 in Chapter 7.

The values in Tables 5.3 and 5.4 are valid for  $S \approx 12$  m/sec.

The values from Tables 5.3 and 5.4 for very stable and near adiabatic conditions are plotted in Fig. 5.6 for comparison purposes. The values of the cross isobaric component are greater for the near adiabatic conditions at both observational times. This is consistent with the trends in the veering angle as observed in Figs. 5.2 - 5.5 at elevations above the lowest 50 mb. However, near the surface we find the veering angle increasing with stability while Fig. 5.6 implies the opposite for the cross isobaric wind component. Inspection of the curves for the ageostrophic component along the isobar, reveals why the surface crossing angle and surface cross isobaric component can have opposite variations with stability. The surface of  $v'' / |\vec{V}_g|$  is a function of both  $\alpha$  and  $|\vec{V}_o| / |\vec{V}_{g_o}|$ . The values of  $u'' / |\vec{V}_g|$  indicates that the ratio  $|\vec{V}_o| / |\vec{V}_{g_o}|$  is significantly greater in the near adiabatic conditions. This comparison demonstrates the potential for errors when using only the veering angle to define the cross isobaric flow.

Table 5.2

Lapse rate combinations from Stratification C which were included in the indicated stability classes. The numbers refer to the lapse rate categories defined in Section 3.3

Combinations from Stratification C				
Very Stable Lapse Rates	1, 1, 1, 1;	1, 1, 1, 2;	1, 1, 2, 1;	1, 1, 2, 2
Moderately Stable Lapse Rates	2, 2, 2, 2			
Near Adiabatic Lapse Rates	3, 3, 2, 2;	2, 3, 3, 3;	3, 3, 3, 2;	3, 3, 3, 3

Table 5.3

Average normalized ageostrophic wind components at 00Z for three stability classes.

	Height (millibars above surface)						
	0	25	50	100	150	200	250
Average Value of $v'' /  \vec{V}_g $							
Very Stable	.30	.40	.41	.22	.07	.01	---
Moderately Stable	.33	.43	.44	.29	.12	.02	---
Unstable	.38	.46	.47	.34	.16	.04	---
Average Value of $u'' /  \vec{V}_g $							
Very Stable	.83	.50	.21	-.04	-.07	-.01	---
Moderately Stable	.71	.43	.21	.00	-.06	-.01	---
Unstable	.54	.31	.15	.02	-.01	.01	---

Table 5.4

Average normalized ageostrophic wind components at 12Z for three stability classes.

	Height (millibars above surface)						
	0	25	50	100	150	200	250
Average Value of $v'' /  \vec{V}_g $							
Very Stable	.29	.30	.24	.06	.01	.00	---
Moderately Stable	.33	.36	.34	.18	.07	.02	---
Unstable	.42	.46	.43	.29	.13	.04	---
Average Value of $u'' /  \vec{V}_g $							
Very Stable	.74	.29	.00	-.15	-.07	-.01	---
Moderately Stable	.70	.30	.05	-.08	-.06	-.02	---
Unstable	.55	.28	.10	-.05	-.05	-.02	---

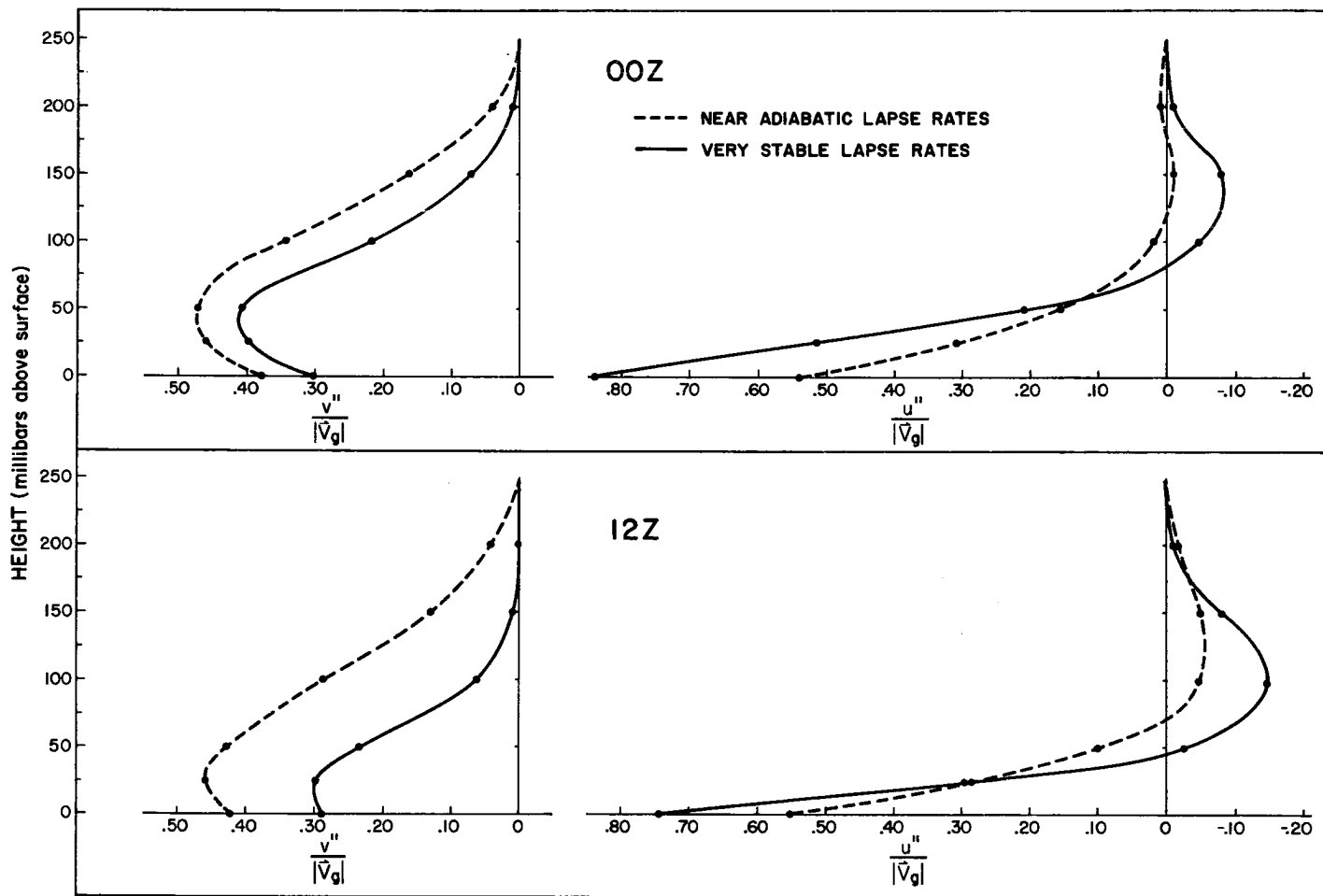


Fig. 5.6. Comparison of the normalized ageostrophic wind components for very stable and near adiabatic conditions during the winter season.

## 5.2 Diurnal Variations

Variations in Wind Veering. This section presents the results of Stratification D (stratification by time of observation). The data from the three land stations - Jackson, Mississippi; Shreveport, Louisiana; and Montgomery, Alabama, were combined. All three stations are located at near  $32.5^{\circ}\text{N}$ .

Fig. 5.7 presents the diurnal variation of the surface crossing angle ( $\alpha_{\circ}$ ). In all seasons, the same basic pattern exists. The maximum value of  $\alpha_{\circ}$  persist from 2100 to 0600 LT while the minimum values occur between 0900 and 1200 LT. At all times the smallest values of  $\alpha_{\circ}$  are for the summer season. The lower atmosphere is typically less stable during the summer season. Thus, the smaller surface crossing angles support the conclusion reached in Section 5.1 - namely, the surface crossing angle decreases as the stability decreases.

Figs. 5.8 - 5.11 show the diurnal changes of  $\alpha$  vs. height for each season. The rate of decrease of  $\alpha$  in the lowest 500 m is maximum at 0600 LT, minimum at 1500 LT. This corresponds to the typical times of maximum low level stability and instability respectively. The level at which  $\alpha$  first becomes zero typically increases from 300-500 m during the period from 0300 to 0900 LT to 1.5 - 2.0 km in the late afternoon. Like the 12Z (0600 LT) profile for summer in Fig. 5.4, there is a tendency for wind backing in the 1 - 2 km layer during the period 0300 - 0900 LT.

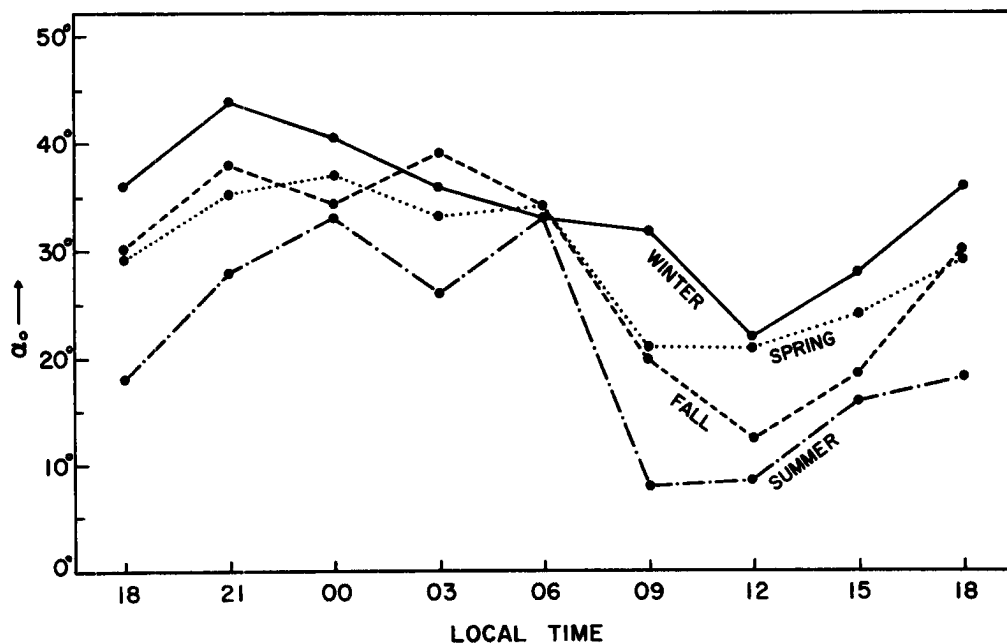


Fig. 5.7. Diurnal variation of the angle between the surface wind and surface isobars. Values based on data from Jackson, Mississippi; Shreveport, Louisiana; and Montgomery, Alabama.

Variations in Wind Speed. Fig. 5.12 shows the corresponding variations observed in the wind speed profiles for the winter and summer seasons. The average wind speed at the surface is a maximum in the afternoon hours and a minimum late at night.

In the 200-1500 m layer an opposite oscillation exists. The maximum speeds occur near 0200 LT with no detectable phase shift with height. The minimum speeds occur in the early afternoon. For the summer season, the time of minimum speed definitely changes with height. At 200 m, the minimum occurs near noon (1200 LT). At 1500 m, the minimum occurs near 1500 LT. The phase shift is approximately three hours or 2.5 hrs./km. This observed phase shift is opposite to that predicted numerically by Krishna (1968). His

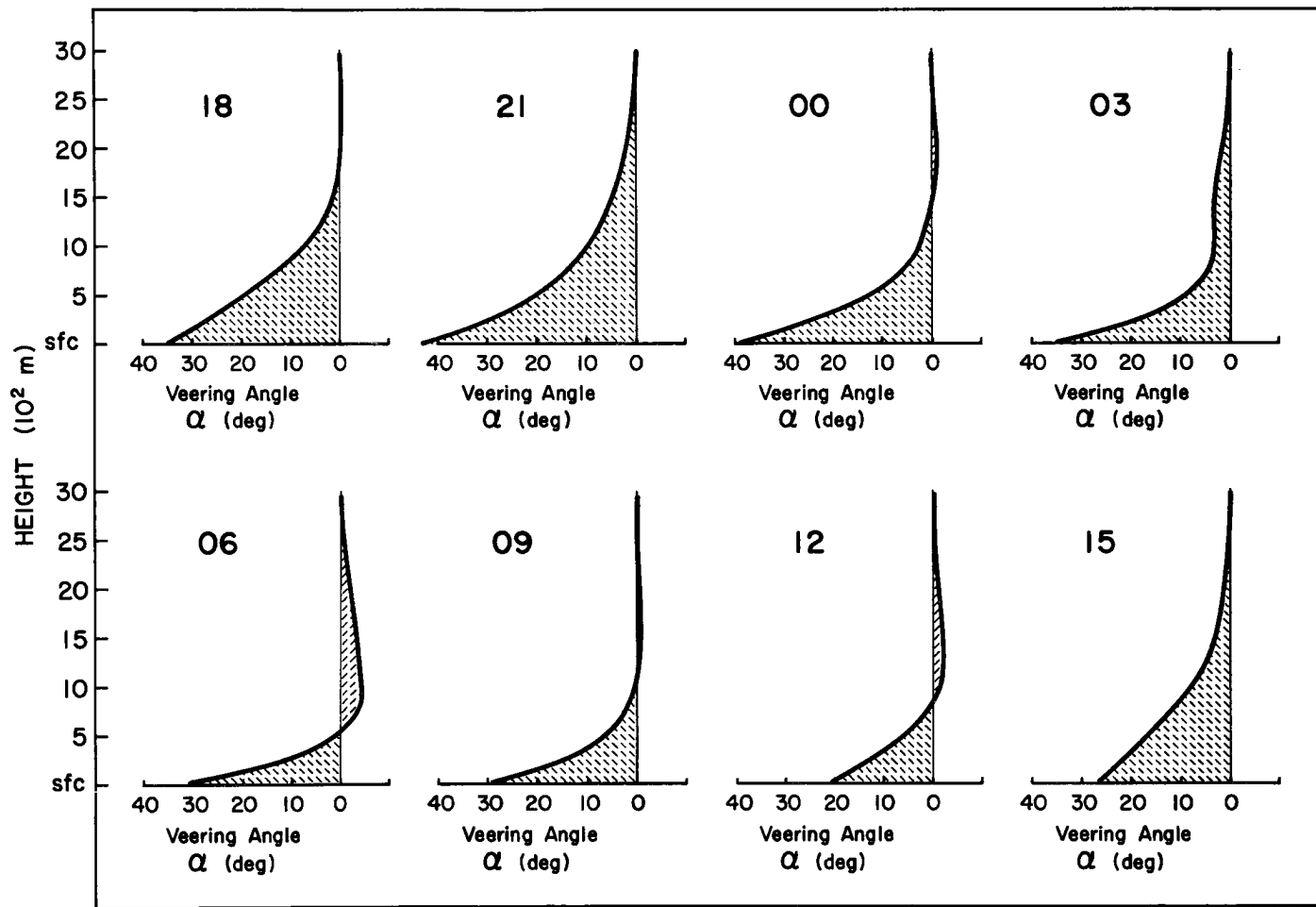


Fig. 5.8. Diurnal variation of the angle between wind and isobars as a function of height. Values based on data from Jackson, Mississippi; Shreveport, Louisiana; and Montgomery, Alabama. Season-Winter. Times are in Local Time.

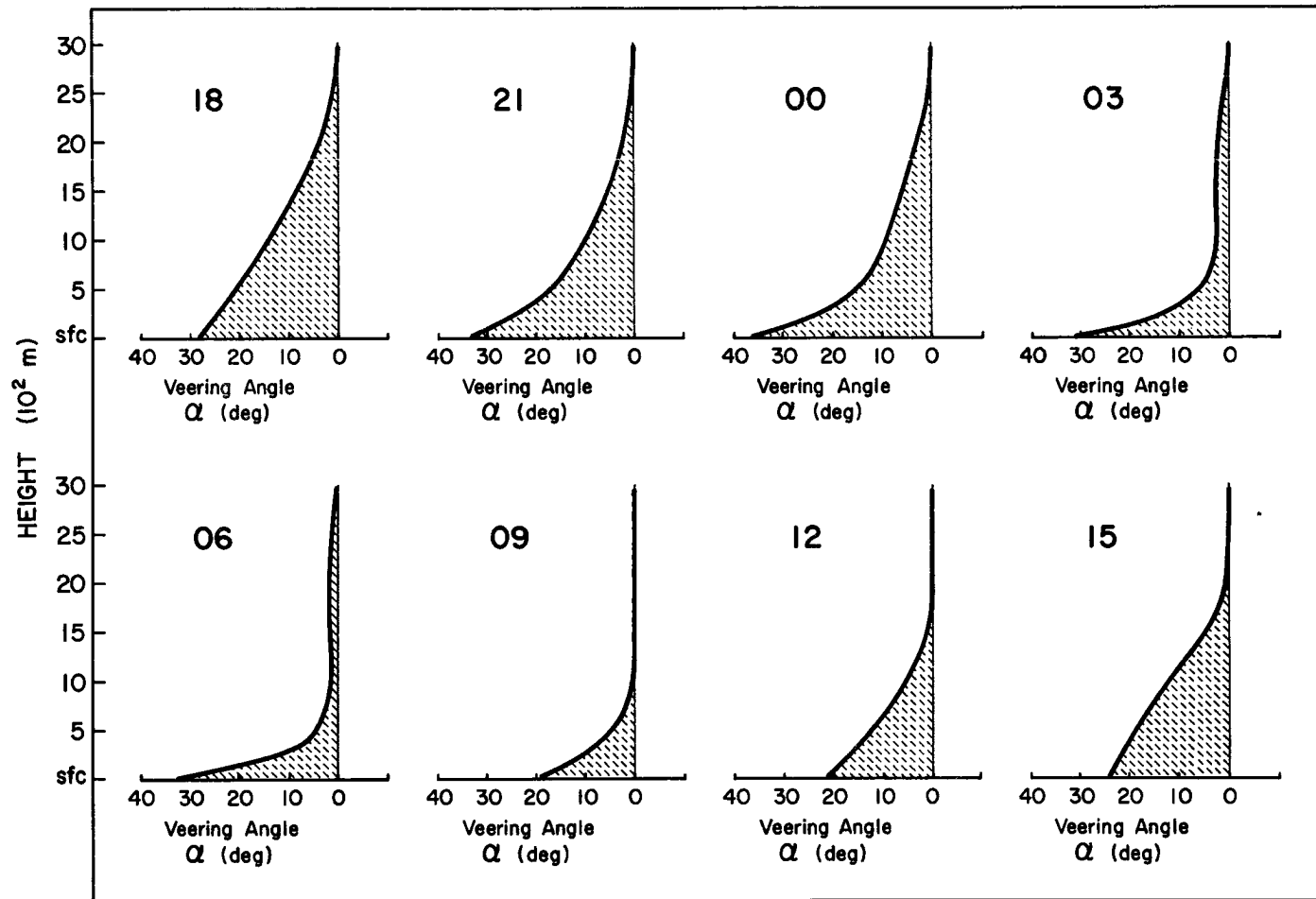


Fig. 5.9. Same as Fig. 5.8. Season-Spring.

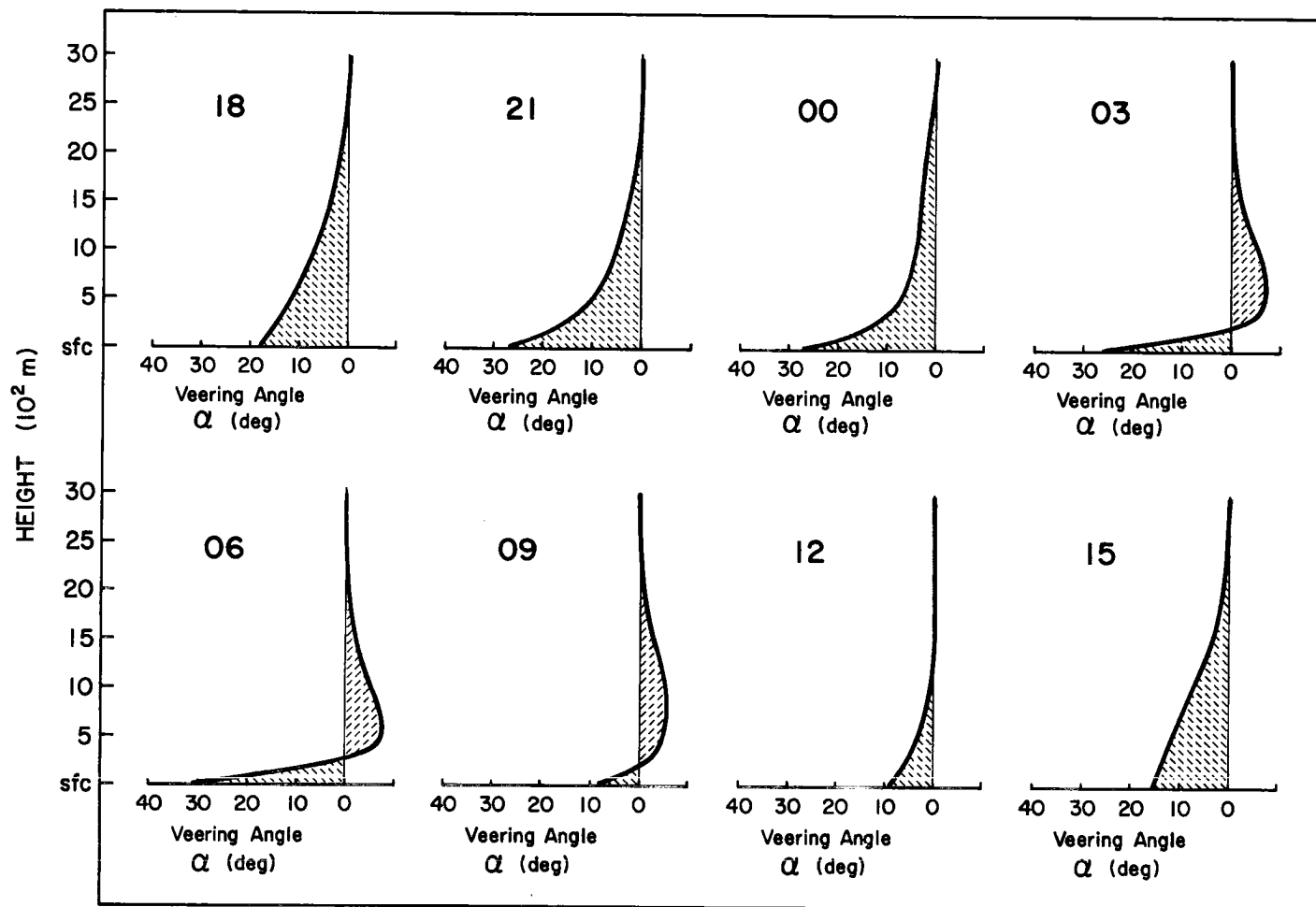


Fig. 5.10. Same as Fig. 5.8. Season-Summer.

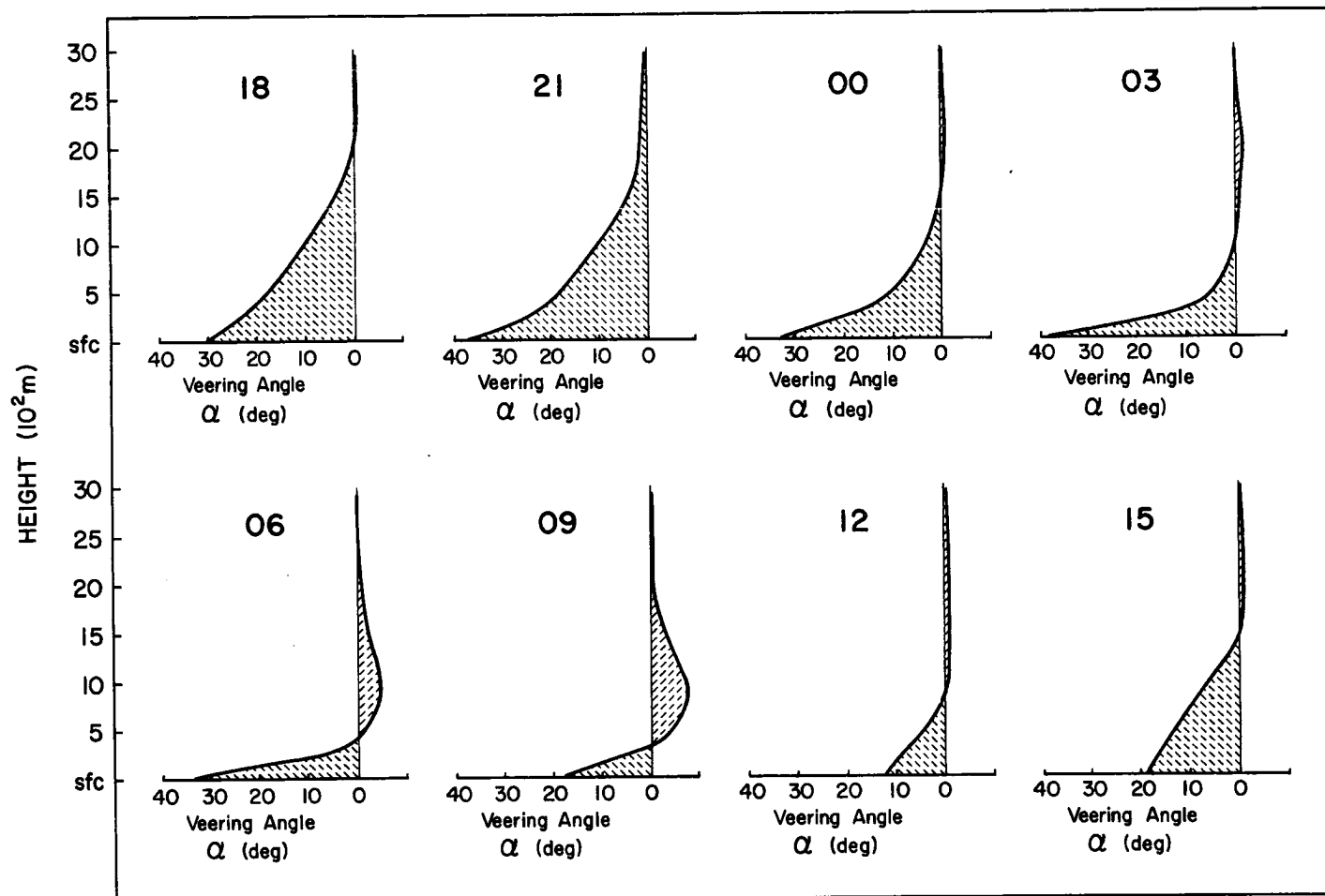


Fig. 5.11. Same as Fig. 5.8. Season-Fall.

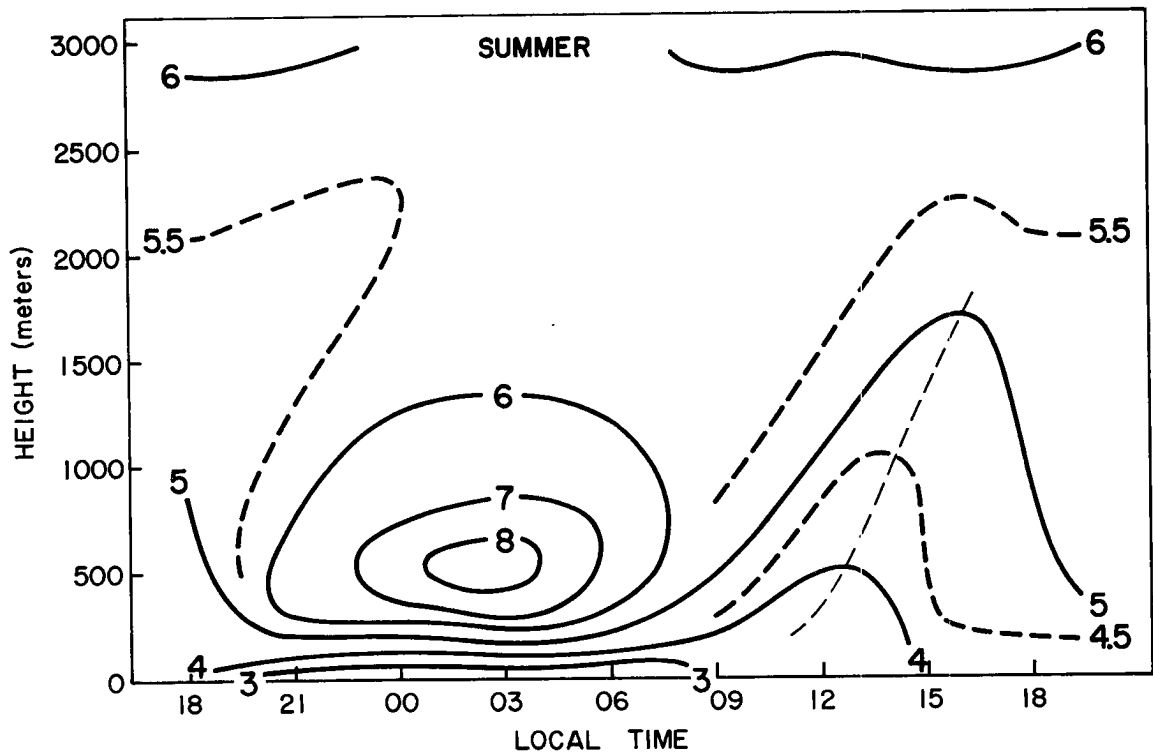
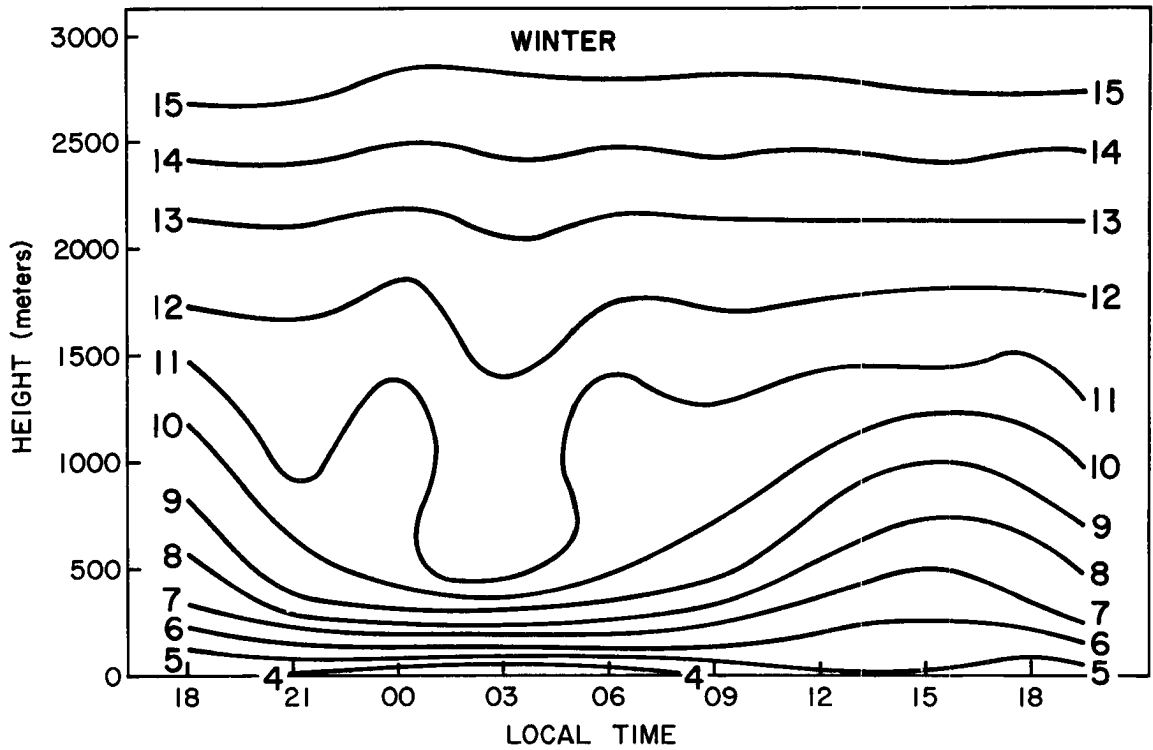


Fig. 5.12. Diurnal variation of the wind speed as a function of height. Values are based on data from Jackson, Mississippi; Shreveport, Louisiana; and Montgomery, Alabama. Times are given in Local Time.

results suggested that both the maximum and minimum speeds are observed first at the higher levels. At  $30^{\circ}\text{N}$ , the phase shift amounted to  $-2 \text{ hrs./km}$  while at  $37^{\circ}\text{N}$  the value increased to  $-8 \text{ hrs./km}$ .

During the night and morning hours, variations in both veering and speed above about 200 m appear to be independent of the changes in the lowest 200 m. The physical processes in the 200 - 1500 m layer are apparently not directly related to surface friction during this period. These observations suggest that the total layer of ageostrophic flow which we have defined as the PBL is made up of two sub-layers during the night and morning hours. The layer adjacent to the surface is the momentum boundary layer or Ekman layer. The top of this layer is the level at which the turbulent mixing induced by surface friction becomes negligible. At night the momentum boundary layer is only a few hundred meters thick. The second layer is formed shortly after sunset when the deep late afternoon momentum boundary layer disappears. Blackadar (1957), and Blackadar and Buajitti (1957) have shown that variations in the ageostrophic wind in this layer correspond to inertial oscillations. We shall therefore refer to this layer as the inertial boundary layer.

Diurnal Variations Over the Ocean. For comparison purposes, the diurnal variations of wind veering vs. height and wind speed vs. height are given in Fig. 5.13 and Fig. 5.14 for Ship E ( $35^{\circ}\text{N}$ ,  $48^{\circ}\text{W}$ ). Here only annual averages are shown. Since the diurnal changes in surface temperatures are usually negligible over the ocean, it can be

inferred that the changes in low level stability are also negligible. Therefore, from arguments given in Section 5.1, it is expected that no significant diurnal variations exist in the wind profiles. This expectation is confirmed in Figs. 5.13 and 5.14. The surface crossing angle is approximately  $12^{\circ}$  with little diurnal variation. This value of  $\alpha_0$  is in good agreement with the mean oceanic value of  $10^{\circ}$  given by Gray (1972).

Qualitative Model of Diurnal Wind Variations. The observed diurnal variations in the winds have been shown above. The reasons for these variations will now be associated with diurnal changes in stability.

The typical diurnal variation in the potential temperature profile for the lowest 2.5 km is given in Fig. 5.15. This diagram is representative of clear sky conditions with no significant synoptic changes. The profiles in Figs. 5.8 - 5.12, however, represent average diurnal changes, since data from both clear and cloudy conditions have been combined. The amplitudes of the wind variations in clear conditions are therefore somewhat suppressed. Nevertheless, the essential features of the daily variation in the wind veering and wind speed profiles can be related to the potential temperature profiles of Fig. 5.15.

As indicated earlier, the data suggests that the lowest 2 km is made up of two layers - the momentum boundary layer and the inertial boundary layer. A schematic diagram of the diurnal variation in the depth of these two layers is included in Fig. 5.16.

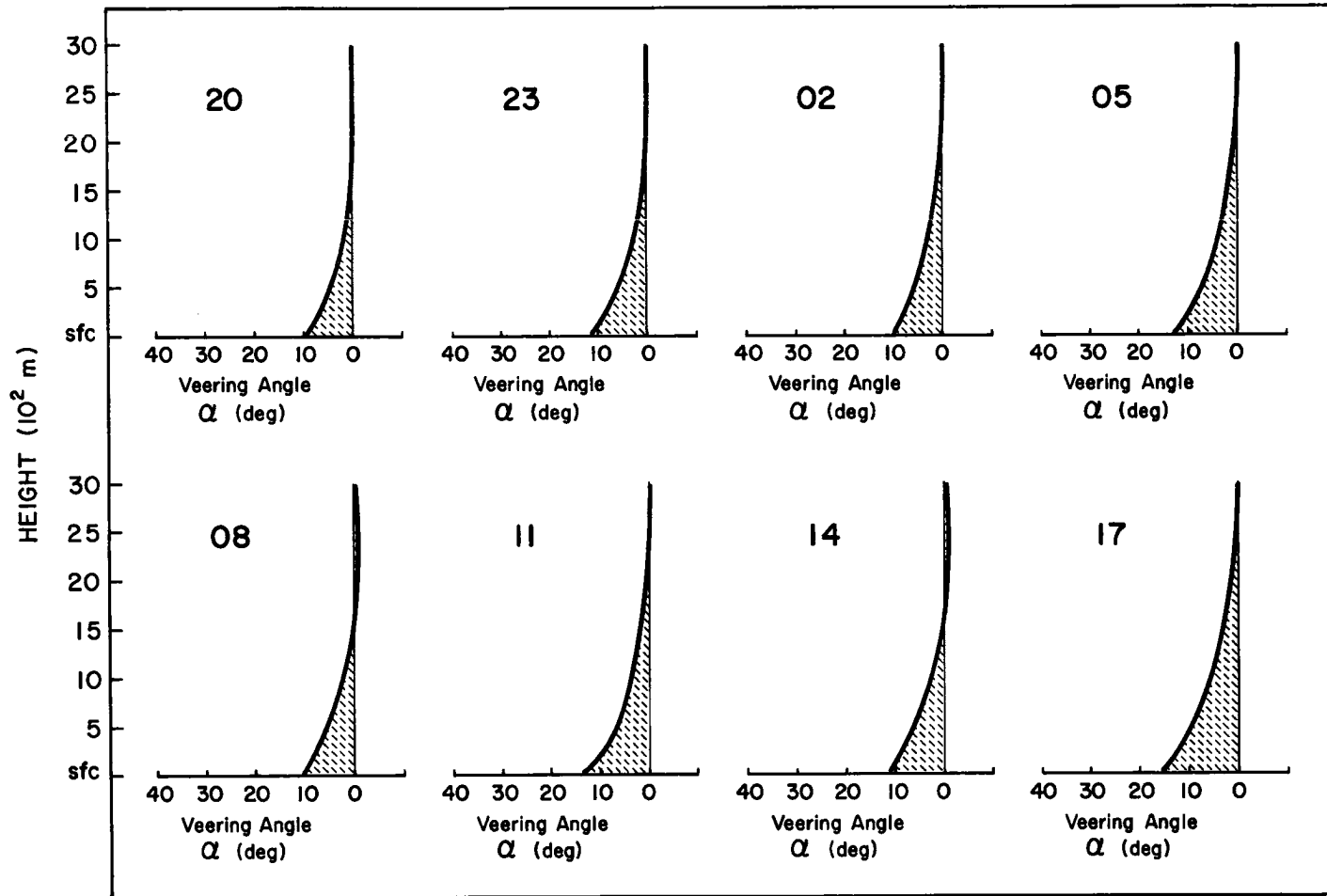


Fig. 5.13. Diurnal variation of the angle between wind and isobars as a function of height for Weather Ship E (35°N, 48°W). Annual average. Times are given in Local Time.

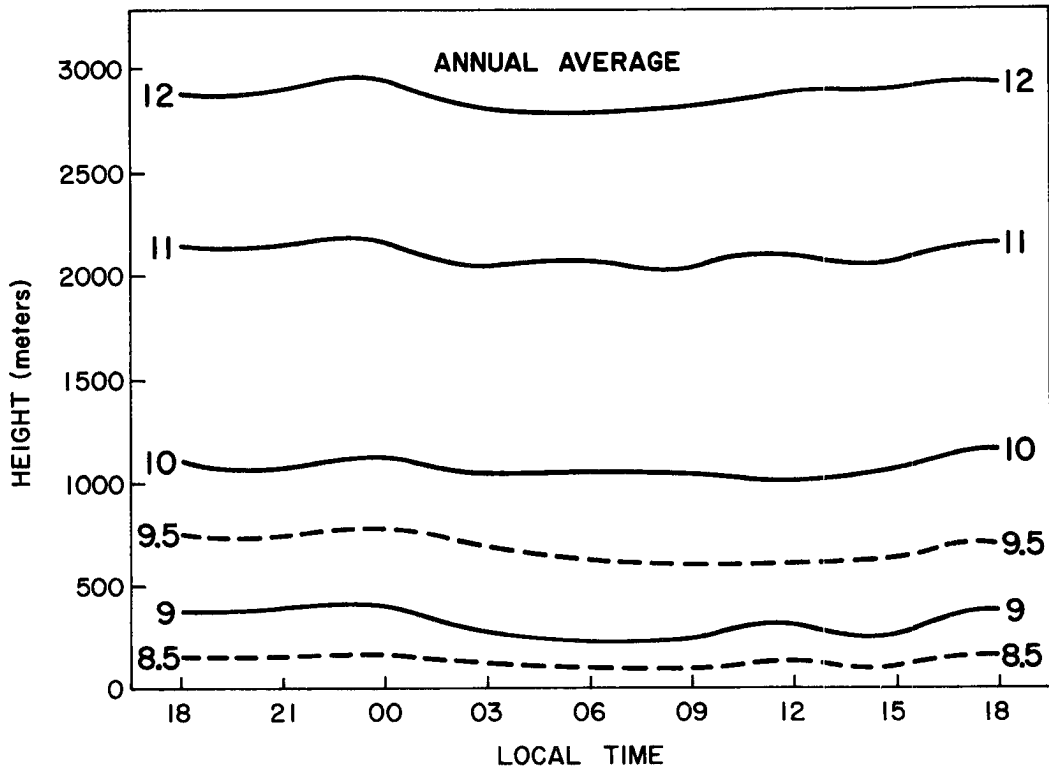


Fig. 5.14. Diurnal variation of wind speed as a function of height for Weather Ship E ( $35^{\circ}\text{N}$ ,  $48^{\circ}\text{W}$ ). Annual average. Times are given in Local Time.

The period of inertial motion is  $2\pi / f$ . The phase of the oscillation therefore depends on the latitude. The change of the ageostrophic wind components after the formation of the inertial boundary layer is demonstrated in Fig. 5.17 for  $35^{\circ}\text{N}$ . In both Figs. 5.16 and 5.17, the inertial boundary layer is developed near 1900 LT.

The discussion will begin with conditions during mid-afternoon (1500 LT). Surface heating and subsequent transfer of this heat to the lower atmosphere has produced a deep layer with adiabatic lapse rate conditions. The momentum boundary layer is nearly 2 km thick. Both the kinetic energy generation and dissipation rates are large with an approximate balance between the terms.

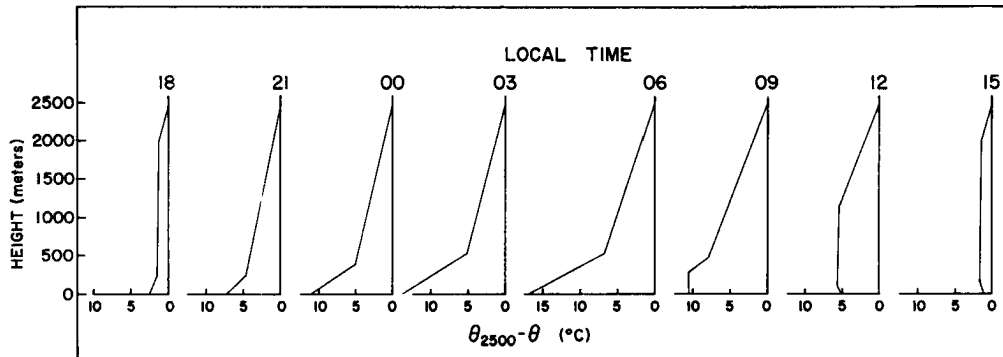


Fig. 5.15. Schematic profiles illustrating the typical diurnal variation in the potential temperature profile for the lowest 2500 m under basically clear sky conditions.

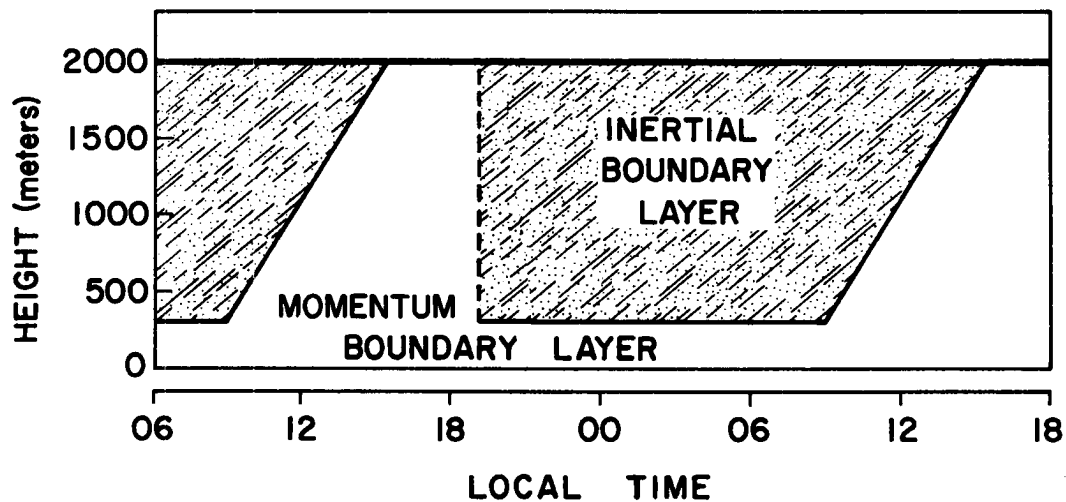


Fig. 5.16. Schematic diagram of the diurnal variation in the depths of the momentum and inertial boundary layers. Together these layers make up the planetary boundary layer.

Just after sunset, the surface cools rapidly. In turn, the lowest layers of the atmosphere are cooled while the temperature in the remainder of the layer remains essentially unchanged. The low level cooling suppresses mechanical and buoyant mixing and leads to the formation of a new and much thinner momentum boundary layer. The veering and speed profiles in the new layer adjust with a time scale of the mixing processes (typically on the order of minutes). The dissipation of kinetic energy by the turbulence processes now becomes confined to the lowest few hundred meters. The total kinetic energy dissipation for the lowest 2 km decreases significantly. Above the developing ground based stable layer, the turbulent mixing decreases rapidly. Frictional forces become insignificant. The adjustment time for the motion increases to that for large scale motion (i. e., inertial motion). As a result, the kinetic energy generation in the layer remains significant for several hours (see Fig. 5.17). With the dissipation mechanism largely eliminated, the wind speeds increase rapidly. Eventually the Coriolis force becomes greater than the pressure gradient force and the flow towards lower pressure decreases to zero. At latitudes of  $35-40^{\circ}\text{N}$ , the wind speeds typically reach maximum values one - three hours after midnight (see Fig. 5.17).

An important consequence of the development of the inertial layer is that the flow at the top of the Ekman or momentum boundary layer will no longer be in geostrophic balance.

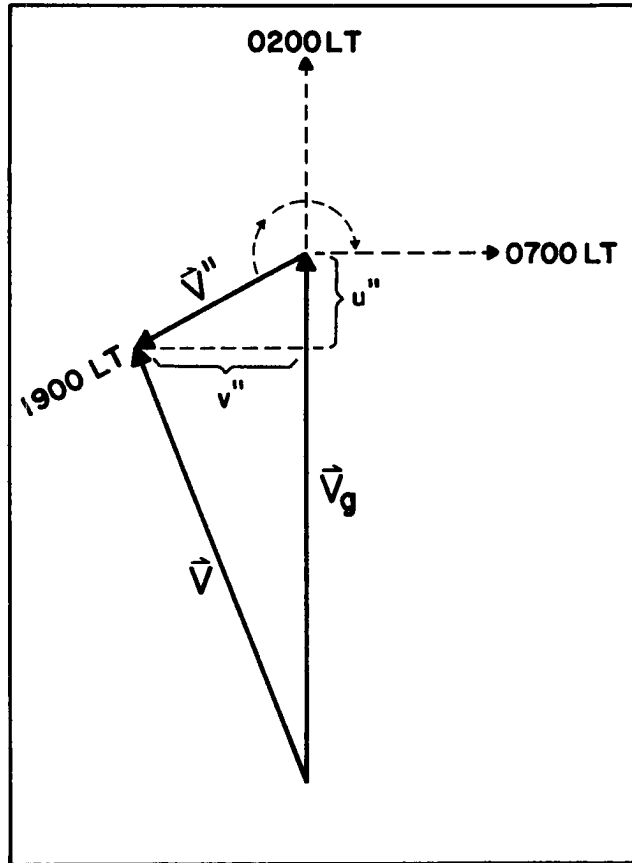


Fig. 5.17. Schematic diagram showing the change of ageostrophic wind components in the inertial boundary layer. Time of formation assumed to be 1900 LT. Latitude  $\approx 35^{\circ}\text{N}$ .

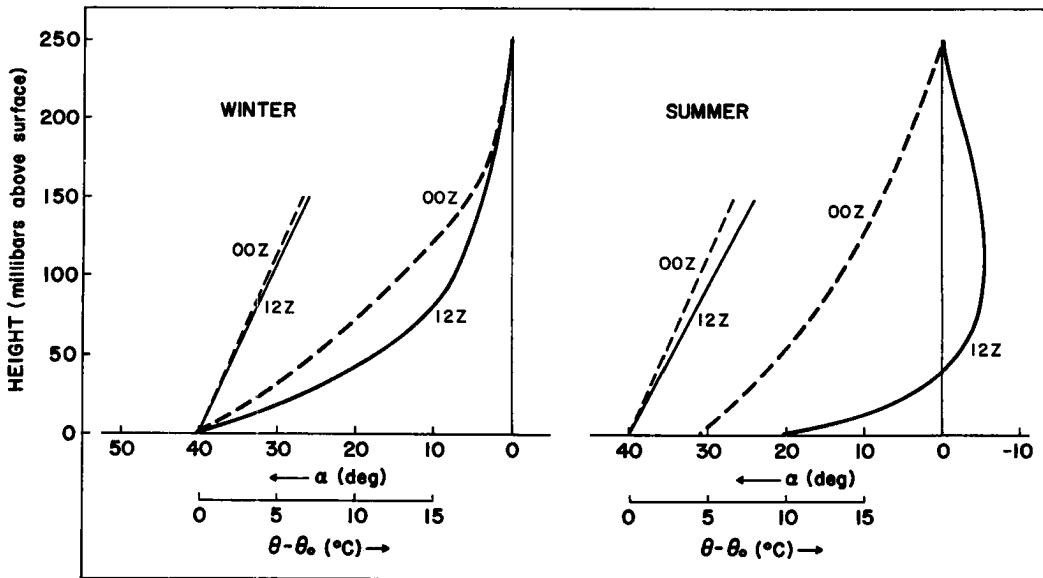


Fig. 5.18. Comparison of the 00Z (1800 LT) and 12Z (0600 LT) veering profiles for conditions with same lapse rate profiles.

By sunrise, the low level stable layer is very well developed. The height of the momentum boundary layer is probably less than 300 meters with the veering angle and speed changing rapidly with height. In the inertial layer, an ageostrophic component towards higher pressure has developed in response to the formation of the super geostrophic wind speeds. This up gradient flow produces negative kinetic energy generation values--conversion of kinetic energy to potential energy. As a result the wind speeds decrease.

After sunrise, surface heating eliminates the ground based stable layer. The mixing in the momentum boundary layer is enhanced by eliminating the restraining effects of a stable atmosphere. The rate of wind veering and speed changes with height are reduced.

Between 0900 and 1500 local time, the surface heating produces a deepening layer in which the lapse rates are essentially adiabatic. The adjustment of the depth of the Ekman or momentum boundary layer occurs on a time scale associated with the turbulent mixing processes. Thus the depth of this layer will at all times correspond roughly to the depth of the adiabatic layer. As the mixing reaches higher and higher, the layer exhibiting inertial motion is eliminated. By mid-afternoon, the inertial layer has been completely destroyed and the boundary conditions for the top of the Ekman layer once again become that specified by gradient or geostrophic balance.

It should be pointed out that at 30-40°N the wind maximum in the inertial layer is destroyed by the combination of two separate processes:

- (1) Flow towards higher pressure (reducing kinetic energy)
- (2) Dissipation by turbulent scale processes as the momentum boundary layer replaces the inertial layer during the period from 0900 to 1500 LT.

The existence of inertial oscillations in the ageostrophic winds means that stability effects cannot be modeled considering only the existing lapse rates. This is vividly demonstrated in Fig. 5.18. Here the profiles for the same lapse rate combination (2, 2, 2, 2) from Stratification C are shown for 12Z (0600 LT) and 00Z (1800 LT). Note the difference in the veering profiles, especially for the summer season.

### 5.3 Conclusions.

The thermal stratification of the lowest kilometer influences the mean wind profile by controlling the height distribution of turbulent momentum transfer. In general, increasing the stability results in the following adjustments in the wind profiles:

- (1) decreased depth of the PBL
- (2) greater angles between the surface wind and isobars
- (3) smaller values of the ageostrophic wind towards lower pressure
- (4) increased vertical shears of the horizontal wind
- (5) smaller values of the ratio  $|\bar{V}_o| / |\bar{V}_{g_o}|$

Diurnal changes in the lapse rates for the lowest 2 km under basically clear conditions, typically leads to:

- (1) the formation of an inertial boundary layer above 200-300 m shortly after sunset
- (2) an order of magnitude variation in the depth of the momentum boundary layer.

Through the night and morning hours the PBL is made up of the momentum and inertial boundary layers. In the afternoon hours, the inertial boundary layer is destroyed. The motions in the inertial boundary layer amplify the daily variations in the PBL wind profiles. This eliminates the feasibility of parameterizing the winds in terms of the existing lapse rates. Only in the afternoon hours does a balance exist among the Coriolis, pressure gradient and frictional forces. The geostrophic departure method for computing surface stress is likewise valid for the afternoon hours only.

## 6. VARIATIONS IN THE KINETIC ENERGY BALANCE OF THE PLANETARY BOUNDARY LAYER RELATED TO CHANGES IN STABILITY

At one time, meteorologists thought that a majority of the kinetic energy (KE) generation and practically all of the KE dissipation in the entire atmosphere occurred in the PBL. Recently diagnostic studies by Kung (1967) and (1969), Trout and Panofsky (1969) and Holopainen (1963) have suggested that a significant portion of both the generation and dissipation occurs above the PBL. Kung (1969) for example found only about 40 percent of the total atmospheric KE generation and dissipation occurs in the lowest 250 mb of the atmosphere.

In the previous chapter the dependence of the ageostrophic winds on stability was shown. In this chapter the corresponding dependence of the kinetic energy generation and dissipation on stability will be examined. First the results of kinetic energy generation calculations for 00Z and 12Z over the U. S. network are presented. These results are compared with the values presented by Kung (1969) for the Northern Hemisphere. Next, diurnal variations in the kinetic energy generation, kinetic energy dissipation, and change in kinetic energy are shown.

### 6.1 Kinetic Energy Generation over the U. S. Network

Method of Computation. The KE generation per unit mass can be written as  $\vec{V} \cdot \nabla(gz)$ . Substituting from the geostrophic wind relationship, this expression can be written as  $f\vec{V} \cdot \vec{V}_g$  or  $f(v'') \left| \vec{V}_g \right|$ .

The KE generation was computed for each of the 81 combinations in Stratification C, using average values of the geostrophic wind speed and cross-isobaric wind component. The values of  $v''$  and  $|\vec{V}_g|$  were obtained by the procedures demonstrated in Fig. 3.6. The winter computations are based on the data values obtained after the geostrophic shear was eliminated from the observed data. The summer computations utilized the actual data with no adjustments. The Coriolis parameter was assumed to be  $9 \times 10^{-5} \text{ sec}^{-1}$  which is the average value for the 19 stations in the U. S. network.

Results. Fig. 6.1 presents the average values of the cross isobaric wind component. The differences between 00Z and 12Z are significant with the 00Z values being larger at all levels. Also, note that at 12Z during the summer months the mean cross isobaric flow is towards higher pressure at elevations greater than 50 mb above the surface.

Table 6.1 contains the computed kinetic energy generation values in units of  $\text{watts/m}^2$  for five layers each 50 mb thick. The total generation in the lowest 250 mb is also given. During winter, the total generation at 00Z is more than twice the 12Z value. During summer, the total generation is slightly negative at 12Z. The fact that the net KE generation can be negative in the lowest 2.5 km is one of the more surprising results of the study. Table 6.2 contains Kung's (1969) results for comparison purposes. Kung found differences between 00Z

and 12Z but not as large as those found in this study. In addition, he found significant generation values at 12Z during his summer season.

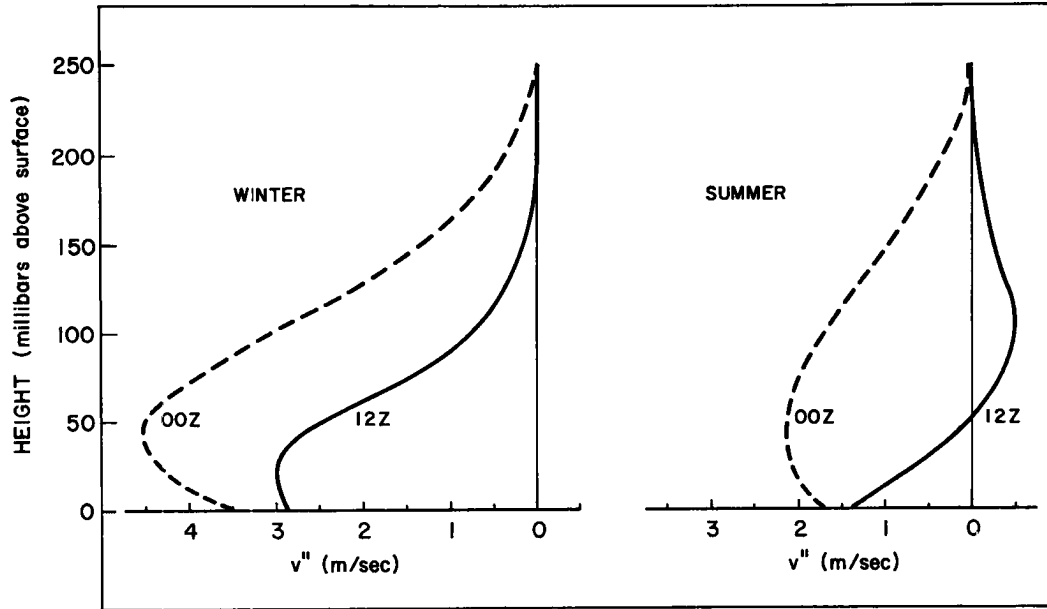


Fig. 6.1. Average cross-isobaric wind components for the 19 interior stations in the U. S. network.

Table 6.1

Average kinetic energy generation (watts/m<sup>2</sup>) for the area covered by the 19 interior stations of the U. S. network.

Winter (Nov. - March)

Summer (June - Aug.)

Height (millibars above sfc)	00Z	12Z	00Z	12Z
0-50	1.93	1.29	.68	.24
51-100	1.88	.77	.66	-.09
101-150	1.16	.24	.46	-.12
151-200	.42	.06	.21	-.06
201-250	.07	.00	.05	-.02
Total	5.46	2.36	2.06	-.05

Table 6.2

Average kinetic energy generation (watts/m<sup>2</sup>) for the Northern Hemisphere as given by Kung (1969).

Pressure Layer (mb)	Winter (Nov. - Apr.)		Summer (May - Oct.)	
	00Z	12Z	00Z	12Z
*				
969-950	.64	.60	.32	.26
950-900	1.64	1.27	.93	.56
900-850	1.20	.82	.79	.29
850-800	.79	.51	.56	.21
800-750	.52	.34	.36	.18
750-700	.37	.29	.23	.14
Total	5.16	3.83	3.20	1.64

\*The average surface pressure for all stations was 969 mb.

Most of the differences between Table 6.1 and 6.2 can be attributed to contrasting methods of analysis. First, Kung used a constant pressure vertical reference frame. By including radiosonde data from the majority of the Northern Hemisphere, he combined the surface data of the stations at higher elevations with the data 1 or 2 km above the surface for stations near sea level. This procedure inevitably spread the computed generation over a deeper layer and smoothed the details of the profile. Secondly, Kung combines all the data recorded at 00Z and 12Z respectively, though his analysis area covers 4 or 5 time zones. This smooths the effects of any diurnal cycle. Thirdly, his winter season consisted of the six month period November-April, while the summer seasons includes the months of May-October. The seasons are therefore defined differently in the two studies.

## 6.2 Diurnal Variations in the Kinetic Energy Budget

Method of Computation. The budget equation for the kinetic energy per unit mass can be written as:

$$\frac{d(\text{KE})}{dt} = \vec{V} \cdot \nabla (gz) - \epsilon \quad (6.1)$$

where  $\epsilon$  is the kinetic energy dissipation.

This equation states that the total rate of change of kinetic energy is equal to the generation minus the dissipation. Assuming that, in the mean, the advective terms are negligible, this equation reduces to

$$\frac{\partial (\text{KE})}{\partial t} = \vec{V} \cdot \nabla (gz) - \epsilon \quad (6.2)$$

Results from Stratification D (stratification by time of observation) were used to obtain estimates of the diurnal variation of each of these three terms.

As indicated earlier, the generation term ( $\vec{V} \cdot \nabla (gz)$ ) can be written as  $f(v'') \left| \vec{V}_g \right|$ . Average values of  $v''$  and  $\left| \vec{V}_g \right|$  were estimated as follows. Values of the ratio  $\left| \vec{V}_g \right| / \left| \vec{V} \right|$  were obtained at 00Z and 12Z for the winter and summer seasons from the results of Stratification C. These values, plus the speed profiles like those in Fig. 5.12 allowed estimates of  $\left| \vec{V}_g \right| / \left| \vec{V} \right|$  to be made for the remaining six observation times. Utilizing the averaging veering profiles in

Figs. 5.8 - 5.11, the average geostrophic wind speed and average cross-isobaric wind component can be evaluated by the following relationships:

$$\overline{v''} \approx |\overline{\vec{V}}| \sin \overline{\alpha} \quad (6.3)$$

$$|\overline{\vec{V}}_g| \approx |\overline{\vec{V}}| (|\overline{\vec{V}}_g| / |\overline{\vec{V}}|) \quad (6.4)$$

The generation term then becomes

$$\overline{\vec{V}} \cdot \nabla(gz) \approx f(|\overline{\vec{V}}| \sin \alpha) [|\overline{\vec{V}}| (|\overline{\vec{V}}_g| / |\overline{\vec{V}}|)] \quad (6.5)$$

The total kinetic energy generation was obtained by integrating Eq. (6.5) over the lowest 2.5 km.

The total kinetic energy in the lowest 2.5 km was obtained by integrating over profiles of the kinetic energy per unit mass. Figures 6.2 and 6.3 provide sample profiles for Shreveport, Louisiana, for the winter and summer seasons respectively. The local changes of kinetic energy are simply the differences between the consecutive three hour energy values.

The generation term and tendency term were computed for each of the three land stations. The values were then combined. In order to obtain a smooth curve of the diurnal variation in these terms, the

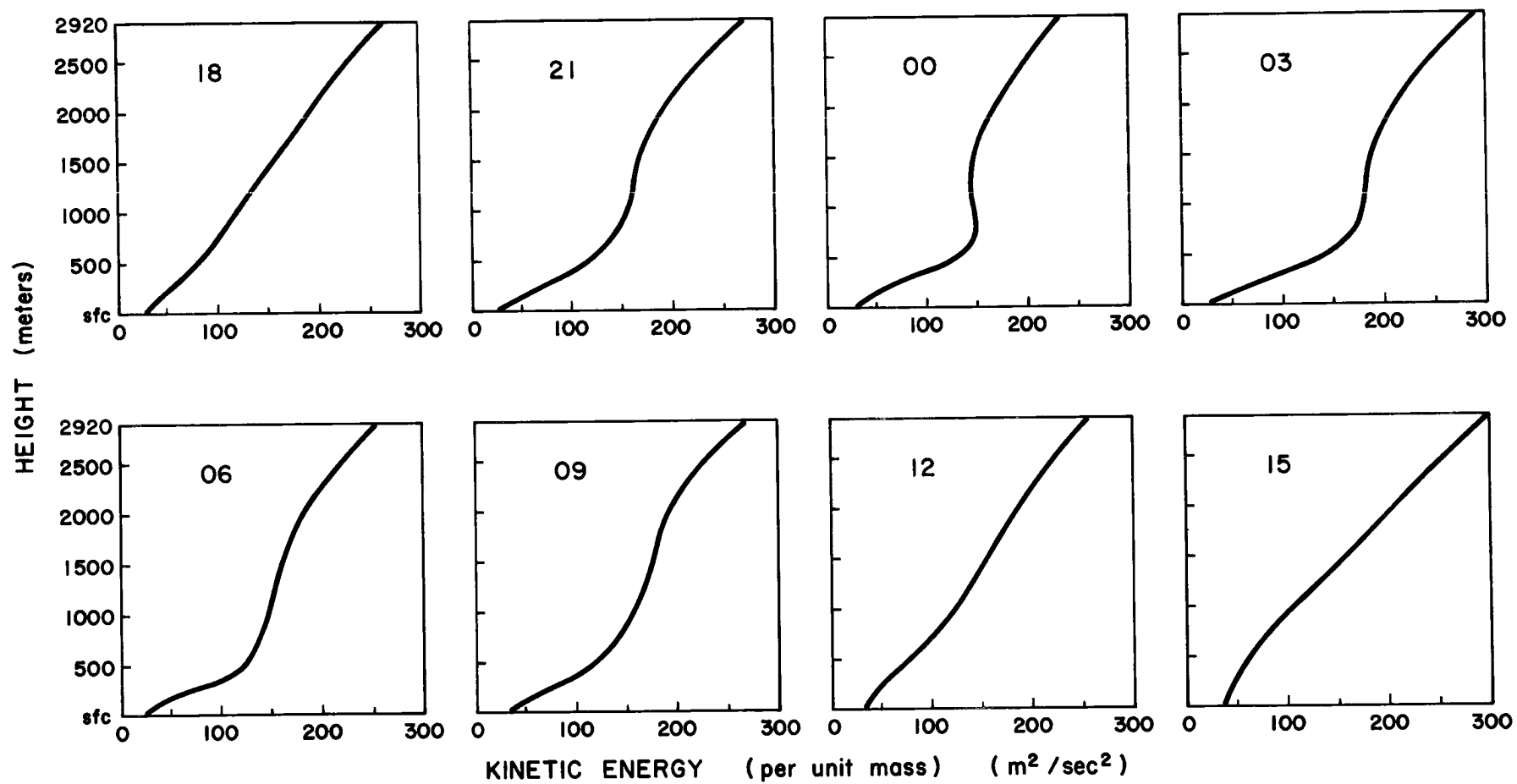


Fig. 6.2. Average diurnal variation in the kinetic energy per unit mass for Shreveport, Louisiana. Season-Winter.

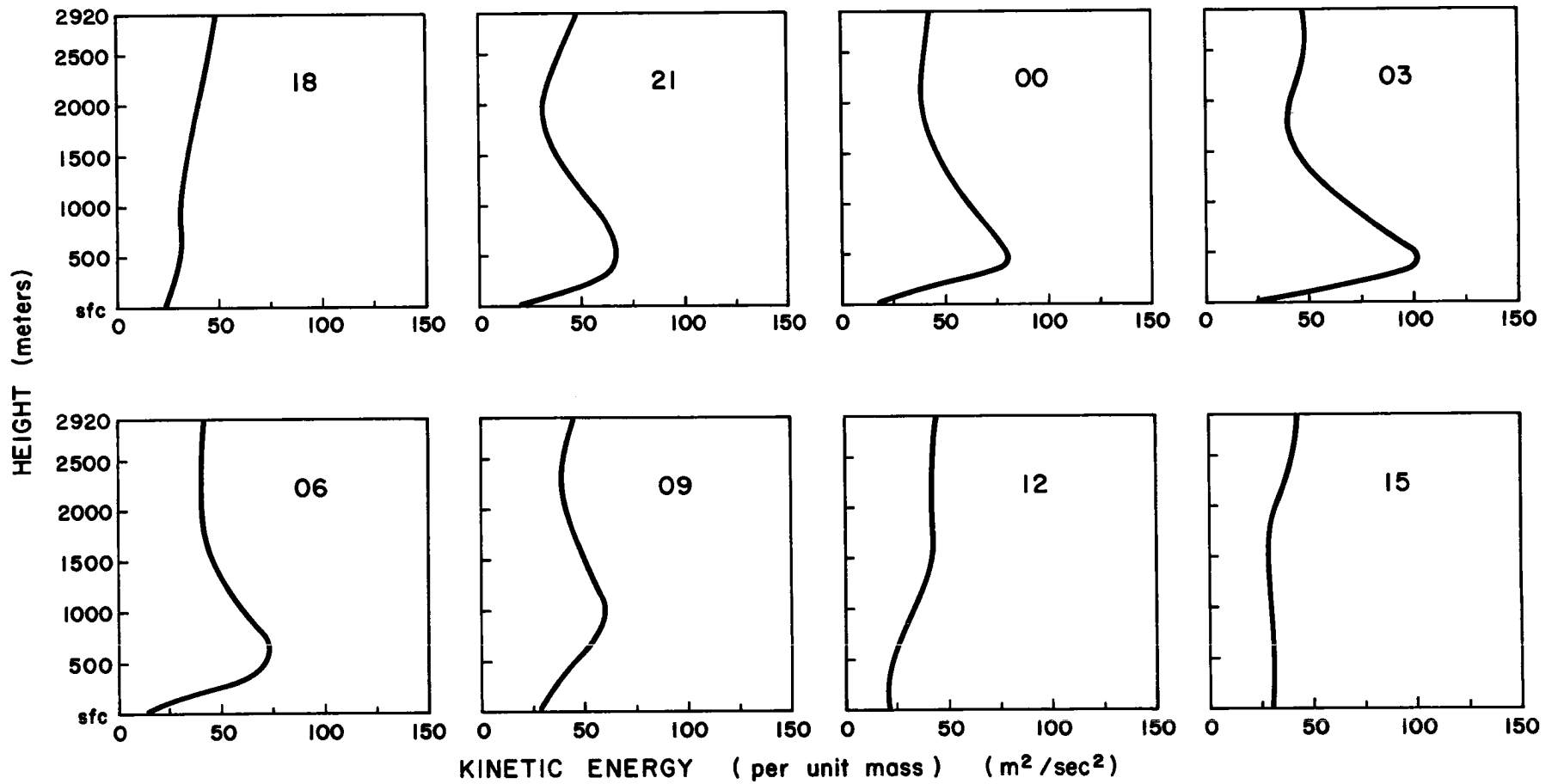


Fig. 6.3. Same as Fig. 6.2. Season-Summer.

eight mean values were subjected to a  $1/4$ ,  $1/2$ ,  $1/4$  smoothing scheme.

Results. The results for each season are plotted in Figs. 6.4 and 6.5. In all seasons, the generation term reaches a maximum near 2100 LT and a minimum near 0700 LT. The flow towards higher pressure in the inertial boundary layer (converting kinetic energy to potential energy) accounts for the negative generation values between 0400 and 1000 LT for the summer and fall seasons.

The local tendency curves indicate that the kinetic energy increases from about 1500 to 0200 LT. The maximum in total kinetic energy therefore occurs about 0200 LT, while the minimum occurs near 1500 LT. This means the kinetic energy variations in the inertial boundary layer dominate over the variations near the surface.

From Eq. (6.2), the difference between the kinetic energy generation and observed change should be equal to the dissipation by turbulent scale processes. The resulting curves for the dissipation are also included in Figs. 6.4 and 6.5. Typically, the dissipation rate reaches a maximum between 1200 and 1500 LT. Minimum values occur between 0000-0600 LT. During the winter season, the diurnal variation in the dissipation curve is suppressed. This is attributed to the dominance of the synoptic scale systems in determining the dissipation rates during winter.

Note that the dissipation curve for the night hours during the summer season becomes slightly positive. This is not physically

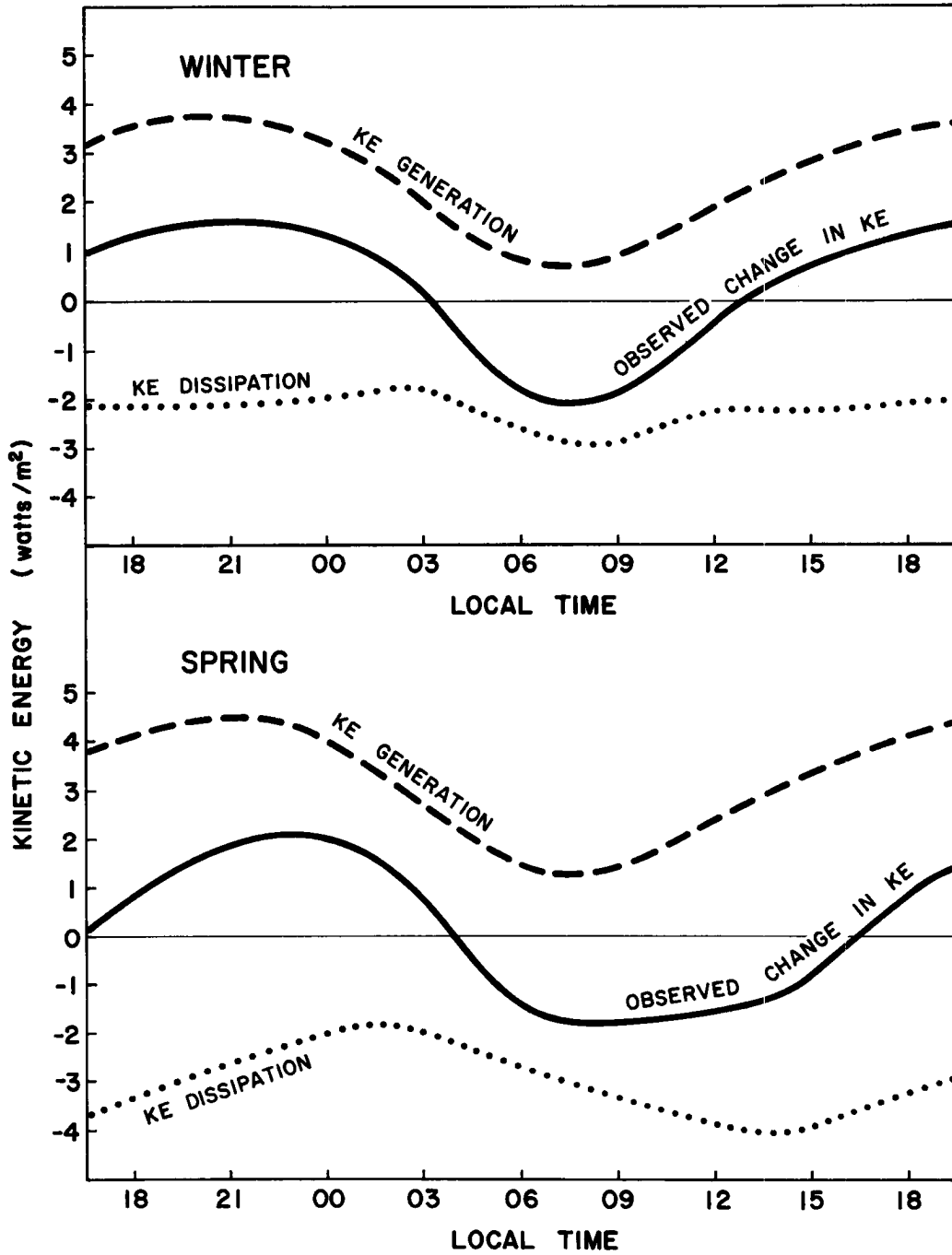


Fig. 6.4. Diurnal variations of kinetic energy generation; kinetic energy dissipation; and change in kinetic energy for the lowest 2.5 km of the atmosphere. Seasons - Winter and Spring.

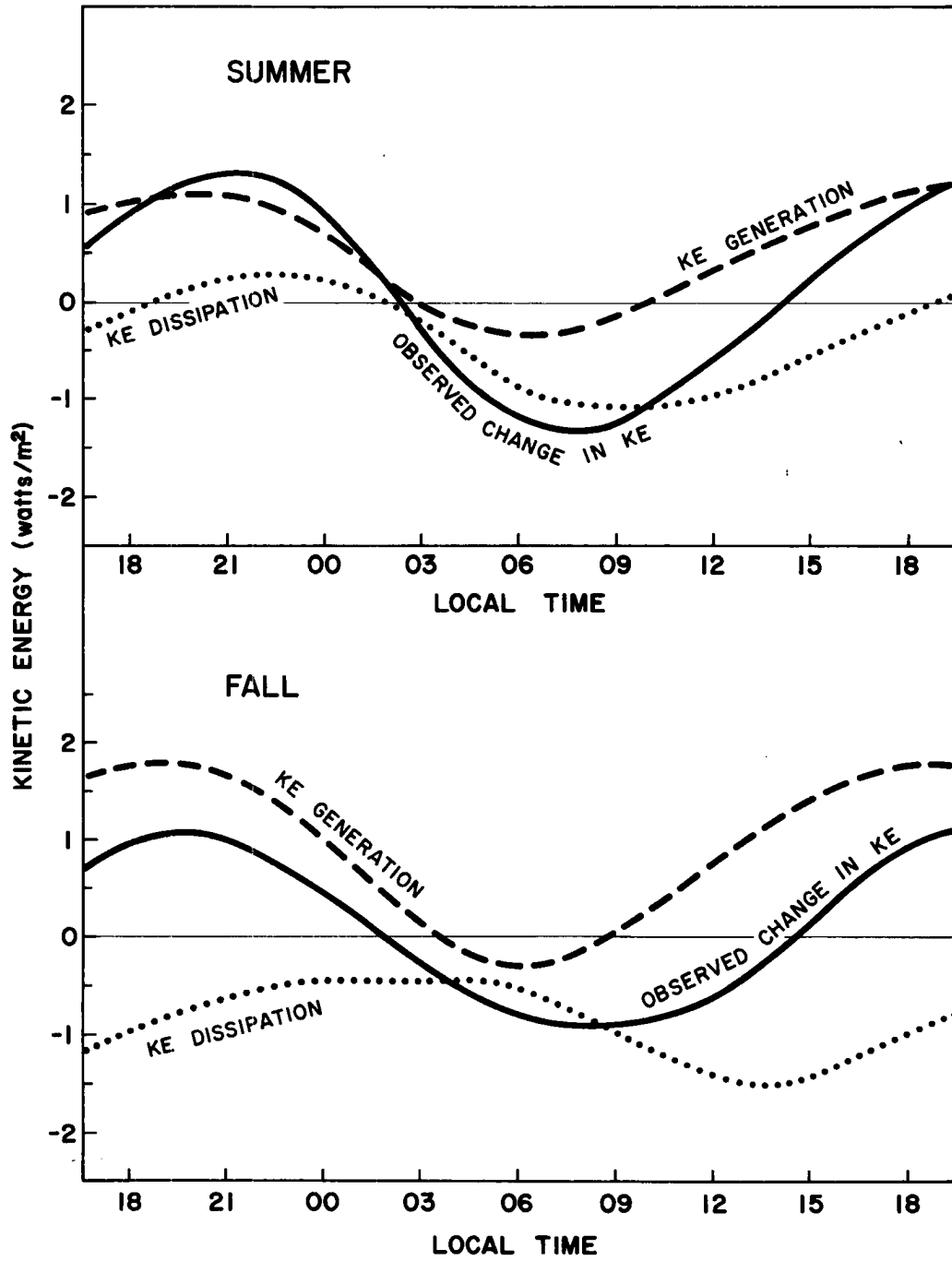


Fig. 6.5. Same as Fig. 6.4. Seasons-Summer and Fall.

realistic. The positive values result from the procedure of computing the dissipation as a residual. In this instance, the computed kinetic energy generation is less than the observed increase in kinetic energy. Remember that the kinetic energy is computed from the individual data values. The kinetic energy generation, however, is obtained from the mean veering and speed curves given in Chapter 5. The inconsistencies in Fig. 6.5 suggest that the mean kinetic energy generation has been underestimated. Indeed, the results given in Chapter 7 (showing the normalized ageostrophic wind component towards lower pressure increasing for higher speeds) support this observation.

While the magnitudes of the generation and dissipation may contain errors, the basic features of the diurnal changes in Figs. 6.4 and 6.5 are believed to be valid.

Figures 6.4 and 6.5 indicate that the often employed assumption of a balance between the kinetic energy generation and dissipation may lead to serious errors. For example, Kung (1967) and (1969) assumed such a balance in his kinetic energy calculations for 00Z ( $\approx$  1800 LT), and 12Z ( $\approx$  0600 LT). The present study shows that the magnitude of tendency term is comparable to the magnitude of the dissipation especially during the period between 0600 and 0900 LT. Only when averaged over the entire day, will the magnitude of the generation and dissipation balance.

### 6.3 Conclusions

The existence of an inertial boundary layer in the night and morning hours amplifies the diurnal variations of both the total kinetic energy generation and the total kinetic energy in the lowest 2.5 - 3 km of the atmosphere. At  $32.5^{\circ}\text{N}$ , the maximum and minimum generation values are observed near 2100 and 0700 LT. The maximum and minimum total kinetic energy is observed near 0200 and 1500 LT. The dissipation and kinetic energy by turbulent scale processes reach a maximum in mid-afternoon and a minimum during the late night hours.

The magnitude of the changes in kinetic energy are comparable to the magnitudes of the total generation and dissipation for much of the day. This means the often employed assumption of the kinetic energy generation being equal to the magnitude of the dissipation is usually not valid.

## 7. EFFECTS OF SPEED ON THE PLANETARY BOUNDARY LAYER WIND PROFILE

Previous studies of the effects of speed variations have considered only the angle between the surface wind and surface isobars. These results are reviewed in Section 7.1. The present study examines the height distribution of both the wind veering and the ageostrophic wind components. These results are presented in Section 7.2.

### 7.1 Previous Results

The dependency of the PBL wind profile on the magnitude of the flow has not received a great deal of attention. Very early, Dobson (1914) stratified observed surface crossing angles according to the magnitude of the wind speed at 650 m. His results, given in Table 7.1, suggested a slight increase of  $\alpha_0$  with increasing wind speed. Recently, Gray (1972), conducted a diagnostic study of wind veering over the ocean areas. His results with regard to speed variations are in Fig. 7.1. With the exception of the tropical areas, he finds larger values of  $\alpha_0$  for higher surface wind speeds.

Table 7.1

Variation of the angle between the surface wind and isobars with speed. Taken from Dobson (1914).

Observed speed at 650 m (m/sec)	0 - 4.5	4.6 - 13	> 13
Surface veering angle (degrees)	13	21.5	20

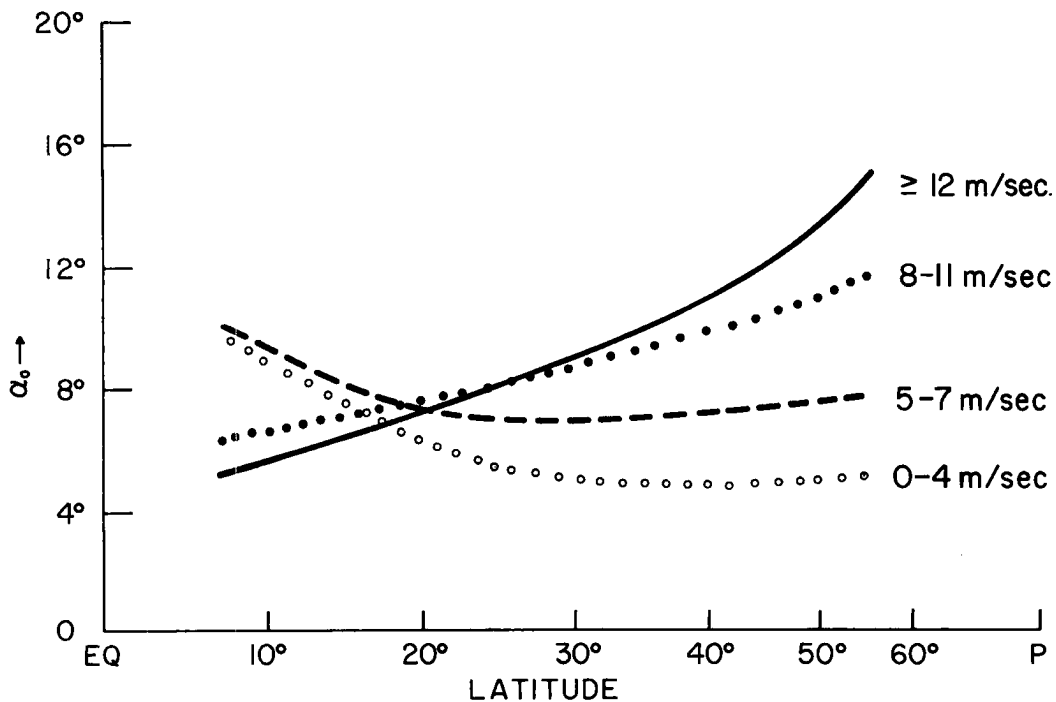


Fig. 7.1. Latitude distribution of the angle between the surface wind and isobars over the oceans for four categories of surface wind speed (taken from Gray, 1972). The averages were obtained by combining all available rawinsonde and pibal data for the period 1949-1964.

Blackadar (1962) has combined the dependence of  $\alpha_0$  on both surface roughness and speed by utilizing the surface Rossby Number—  
 $R_0 = \left| \vec{V}_{g_0} \right| / fz_0$ . Fig. 7.2 portrays the relationship as predicted by Blackadar for neutral conditions. For a constant value of  $z_0$ , this

curve predicts a decrease in  $\alpha_0$  as the value of  $\left| \vec{V}_{g_0} \right|$  increases. However, this decrease is small, amounting only to about  $5^\circ$  for an increase from 5 to 25 m/sec in  $\left| \vec{V}_{g_0} \right|$ . Blackadar also calculated values of  $R_0$  and  $\alpha_0$  from data obtained in several observational studies. These results are also given in Fig. 7.2. Much of the scatter in the observational data can be attributed to thermal wind and

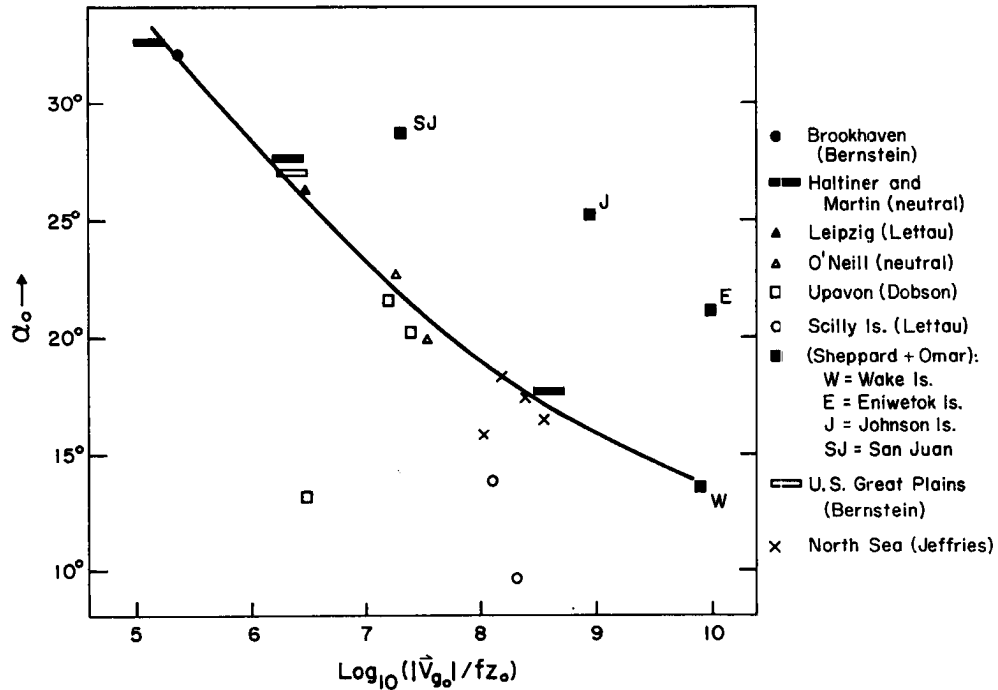


Fig. 7.2. Angle between surface wind and isobars as a function of the surface Rossby number. (Taken from Blackadar (1962)). The source of the various observations included Bernstein (1959), Dobson (1914), Jeffries (1920), Lettau (1950, 1957), Sheppard and Omar (1952) and Blackadar.

stability variations. However, most of the variability in the computed values of  $R_0$  results from changes in  $z_0$ , not  $\left| \vec{V}_{g_0} \right|$ .

## 7.2 Significance of the Speed Parameter (S)

In the present study the speed parameter (S) is the average speed in the lowest 100 mb. This should be a better measure of the magnitude of the flow field, than the observed speed at any one level. In addition, there should be only a small correlation between the value of  $z_0$  and S. (A significant correlation would be expected if the speed parameter was the surface wind speed).

Variations in Wind Veering. Figs. 7.3 and 7.4 show the dependence of the wind veering on the speed as revealed by Stratification B

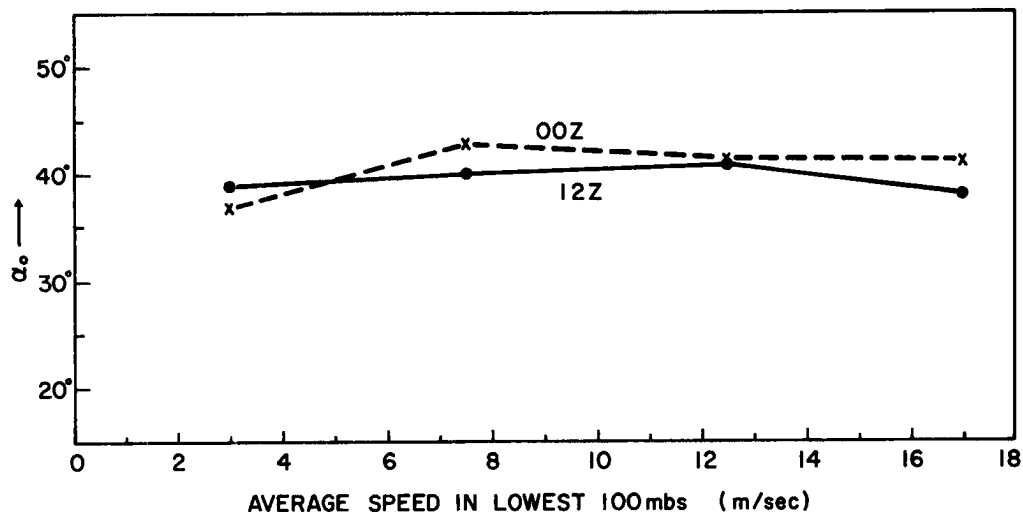


Fig. 7.3. Angle between the surface wind and isobars as a function of the average speed in the lowest 100 mb.

(five speed, three stability and nine baroclinicity categories - geostrophic shear eliminated from the wind data). In Fig. 7.3 the surface crossing angle,  $\alpha_0$ , is plotted as a function of  $S^2$ . No systematic variation is evident, suggesting that no significant relationship exists between  $S$  and  $\alpha_0$ . The combinations from Stratification B which were averaged to yield Figs. 7.3 - 7.4 are listed in Table 7.2.

The profiles of the veering angle vs. height for the four speed categories are shown in Fig. 7.4. Again no great differences are noted. There is a tendency for  $\frac{\partial \alpha}{\partial z}$  to decrease in the lowest 50 mb as the speed increases. Also, the depth of the layer of significant cross isobaric flow increases slightly in the higher speed categories.

Variations in Ageostrophic Winds. Tables 7.3 and 7.4 list the average values of  $|\vec{V}_g|$ ,  $u'' / |\vec{V}_g|$  and  $v'' / |\vec{V}_g|$  for the same

<sup>2</sup>Results for  $S > 20$  m/sec are not shown because of an insufficient number of observations in this category.

Table 7.2

List of categories and number of observations in each category (from Stratification B) which are included in the speed analysis. (See Section 3.3 for a description of the categories).

00Z		Number of Observations			
Categories		Speed Categories			
Stability	Thermal Wind	1	2	3	4
1	1	64	97	33	9
2	1	169	223	92	10
3	1	225	310	135	24
1	2	45	148	73	20
2	2	188	232	95	20
3	2	153	198	62	9
2	3	122	205	88	19
3	3	148	165	61	10
2	4	86	171	46	13
3	4	144	204	99	10
3	5	141	203	58	12
3	6	191	228	64	8
3	7	219	457	237	26
2	8	183	255	90	10
3	8	255	624	336	74
1	9	10	51	59	27
2	9	33	181	235	87
3	9	43	398	405	134

12Z		Number of Observations			
Categories		Speed Categories			
Stability	Thermal Wind	1	2	3	4
1	1	321	335	158	40
2	1	106	169	120	22
1	2	216	323	124	31
2	2	84	123	52	11
1	3	136	255	98	22
2	3	54	86	37	14
2	4	38	101	36	9
2	5	49	156	69	13
2	6	95	235	90	12
3	6	20	78	78	17
1	7	214	334	115	11
2	7	135	363	160	26
3	7	29	211	156	37
1	8	259	429	166	34
2	8	144	322	187	38
3	8	24	126	123	32
1	9	58	336	388	145
2	9	21	240	363	207

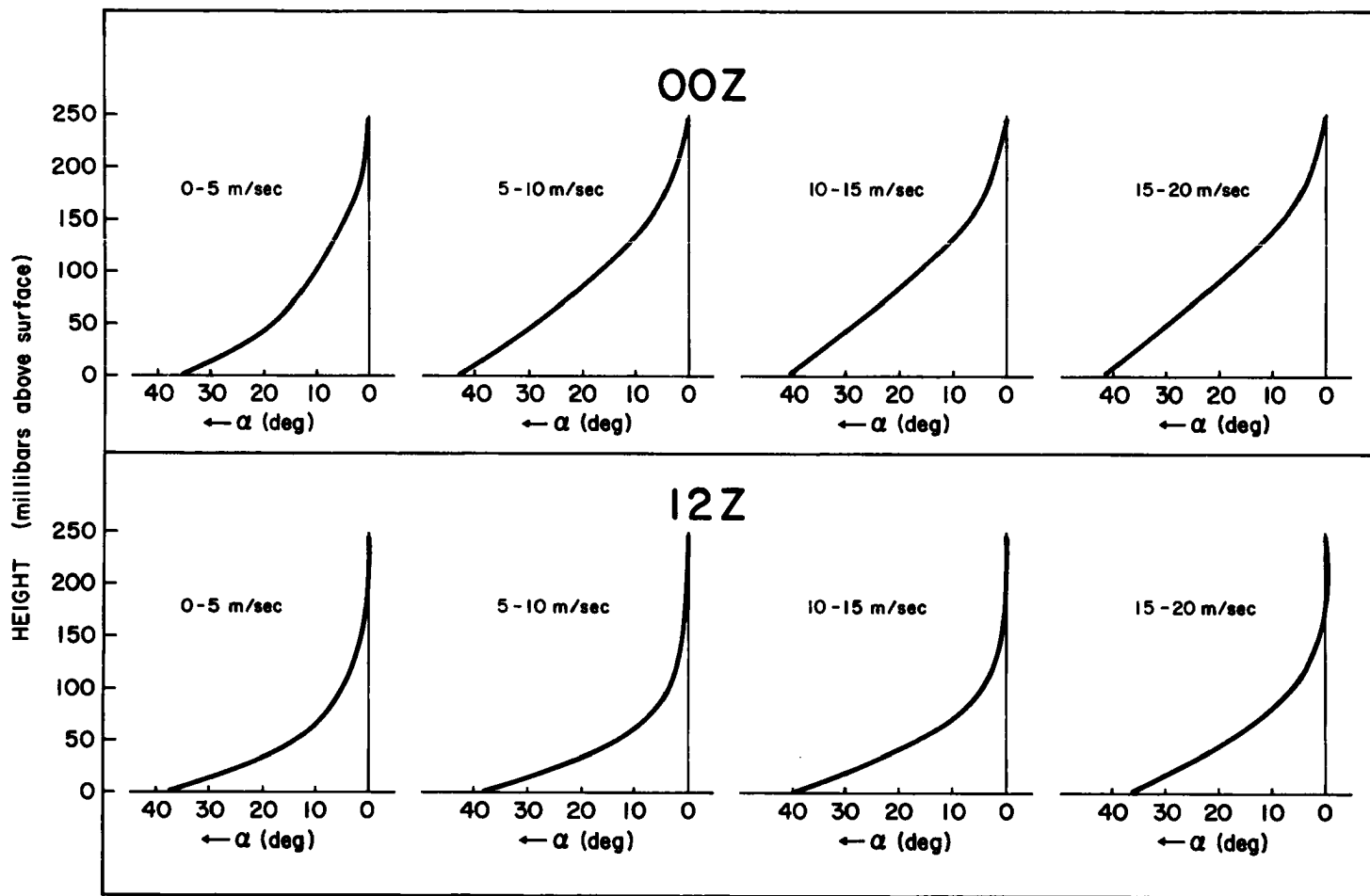


Fig. 7.4. Angle between wind and isobars as a function of height for the four categories of average speed in the lowest 100 mb.

Table 7.3

Average values of the geostrophic wind speed, and the normalized ageostrophic wind components at 00Z, for four wind speed categories.

Height (millibars above surface)

S (m/sec)	Average Geostrophic Wind Speed $ \vec{V}_g $ (m/sec)						
	0	25	50	100	150	200	250
0-4.9	5.4	5.8	6.2	7.0	7.8	8.6	9.4
5.0-9.9	10.0	10.4	10.8	11.4	12.0	12.6	13.2
10.0-14.9	14.4	14.7	15.0	15.7	16.3	16.9	17.5
15.0-19.9	18.4	18.8	19.2	20.0	20.7	21.4	22.0

S (m/sec)	Average Value of $v'' /  \vec{V}_g $						
	0	25	50	100	150	200	250
0-4.9	.35	.33	.27	.17	.08	.01	---
5.0-9.9	.31	.38	.39	.26	.12	.04	---
10.0-14.9	.29	.41	.43	.29	.12	.04	---
15.0-19.9	.31	.45	.48	.33	.14	.03	---

S (m/sec)	Average Value of $u'' /  \vec{V}_g $						
	0	25	50	100	150	200	250
0-4.9	.68	.52	.38	.22	.09	.02	---
5.0-9.9	.70	.47	.30	.12	.05	.02	---
10.0-14.9	.70	.43	.22	.00	-.04	-.01	---
15.0-19.9	.69	.40	.18	-.06	-.09	-.02	---

categories used in Figs. 7.3 and 7.4. Here in the parameters which define the normalized ageostrophic wind, a definite dependence on speed emerges in the layer 25-150 mb above the surface. Since Figs. 7.3 and 7.4 show no significant variations, we again have an example of the failure of the wind veering in defining the cross-isobaric flow.

Fig. 7.5 provides a comparison of the ageostrophic components for light and strong speeds. While the surface values of  $v'' / |\vec{V}_g|$  decrease slightly with increasing values of S, there is a noticeable

Table 7.4

Average values of the geostrophic wind speed, and the normalized ageostrophic wind components at 12Z, for four wind speed categories.

Height (millibars above surface)

S (m/sec)	Average Geostrophic Wind Speed $-\left \vec{V}_g\right $ (m/sec)						
	0	25	50	100	150	200	250
0-4.9	5.4	5.9	6.3	7.2	8.1	9.0	9.9
5.0-9.9	8.2	8.7	9.2	10.2	11.1	12.0	13.0
10.0-14.9	12.4	12.8	13.2	14.1	14.9	15.7	16.5
15.0-19.9	16.3	16.8	17.2	27.9	18.7	19.5	20.4

S (m/sec)	Average Value of $v'' / \left \vec{V}_g\right $						
	0-4.9	.32	.25	.17	.08	.04	.01
5.0-9.9	.33	.32	.25	.08	.03	.01	---
10.0-14.9	.31	.36	.32	.11	.02	.00	---
15.0-19.9	.31	.40	.38	.17	.03	.00	---

S (m/sec)	Average Value of $u'' / \left \vec{V}_g\right $						
	0-4.9	.69	.43	.25	.14	.06	.01
5.0-9.9	.67	.32	.08	-.05	-.03	-.01	---
10.0-14.9	.69	.30	.02	-.16	-.09	-.03	---
15.0-19.9	.67	.29	.00	-.22	-.16	-.05	---

increase in the values at the levels above the surface. The net result is an increase (with increasing speed) in the value of the normalized cross-isobaric flow. The profiles of  $u'' / \left|\vec{V}_g\right|$  show the reverse trend - as the speed increases the values decrease at all levels above the surface. (Remember that  $u''$  is positive when the wind component along the isobar is less than the geostrophic wind speed.)

Fig. 7.6 shows the average profiles of the cross isobaric wind component toward lower pressure for the four speed categories for the

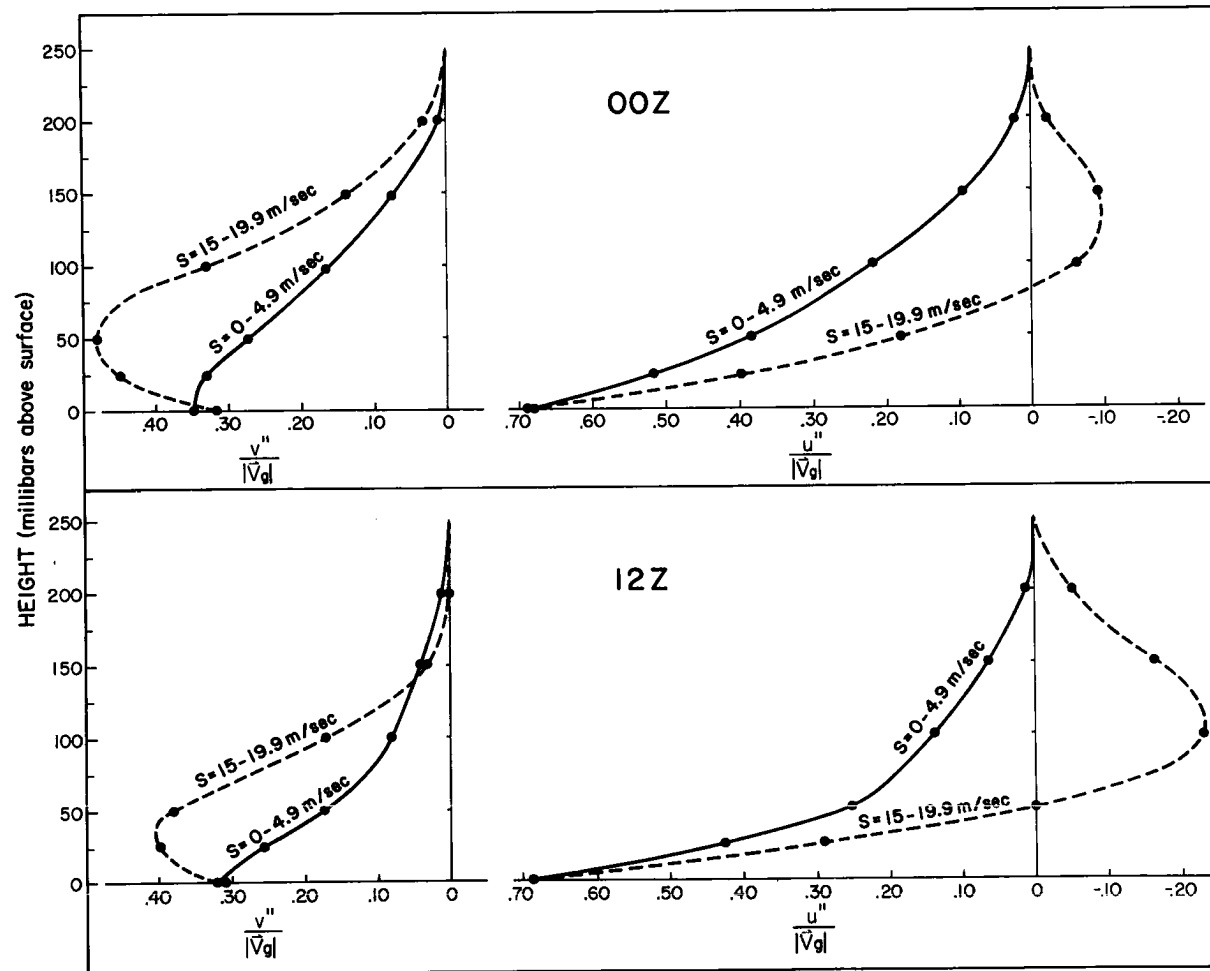


Fig. 7.5. Comparison of the normalized ageostrophic wind components for conditions of weak and strong winds in the lowest 100 mb.

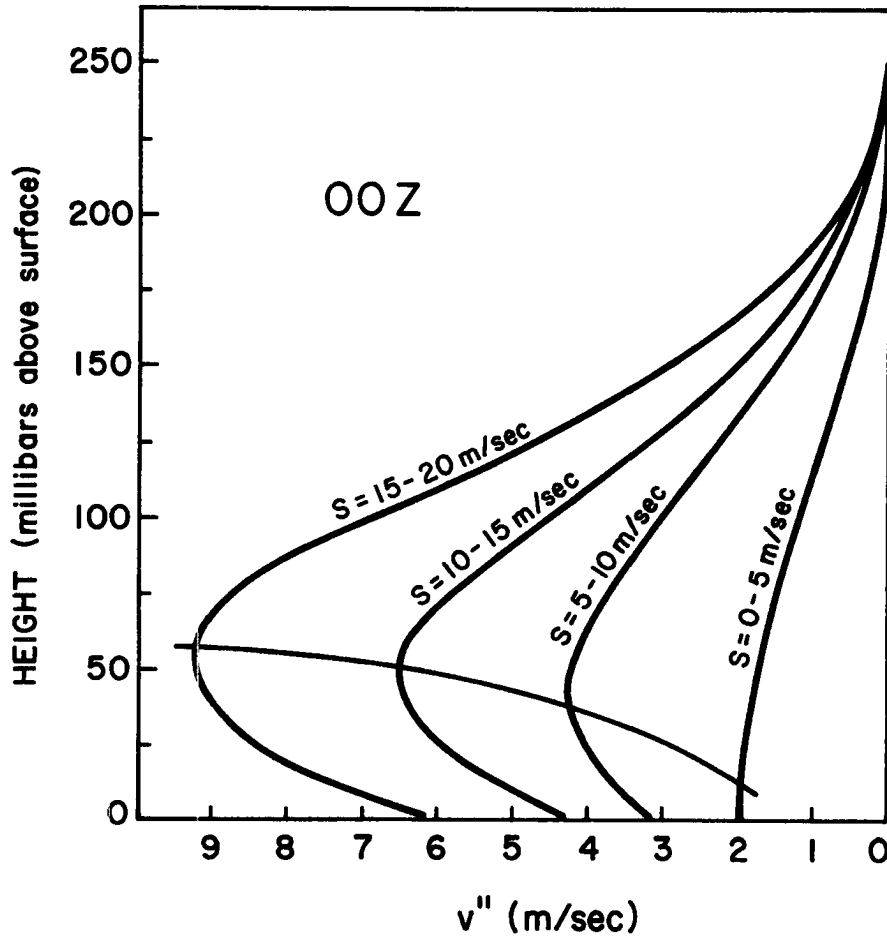


Fig. 7.6. Profiles of the average ageostrophic wind component towards lower pressure for four categories of average speed in the lowest 100 mb.

00Z data. Note that the level of maximum  $v''$  becomes higher as the value of  $S$  increases. Lettau (1962) and Lettau and Dabberdt (1970) have hypothesized that the level of maximum cross-isobaric flow corresponds to the level of maximum  $K_m$  where  $K_m$  is the coefficient of eddy diffusivity. Fig. 7.6 then suggests that the level of maximum  $K_m$  increases with increasing speed. If the depth of the PBL and the angle between surface wind and isobars remain unchanged, this results in an increase of the total ageostrophic flow towards lower pressure as shown in Tables 7.3 and 7.4.

### 7.3 Conclusions

Increasing the average speed in the lowest 100 mb has no significant effect on the angle between wind and isobars at the surface. However, as the speed increases, significant changes are observed in the magnitude of the ageostrophic wind components, especially in the layer 25-150 mb above the surface. In this layer, the normalized ageostrophic wind component towards lower pressure increases with increasing speed, while the ageostrophic component along the isobar decreases.

As the speed increases, the level of maximum cross-isobaric flow increases, implying that the level of maximum eddy diffusivity increases. This changes the characteristics of the stress profile, leading to the variations in the ageostrophic winds.

## 8. EMPIRICAL MODEL OF AGEOSTROPHIC WINDS

In the previous chapters we have examined in detail the way in which various external factors modify the PBL wind profile. In this chapter, these results will be incorporated into relationships defining the variability of the wind profiles. This is done as follows: First, typical or mean profiles of normalized ageostrophic wind components ( $v'' / |\vec{V}_g|$  and  $u'' / |\vec{V}_g|$ ) are defined for the U. S. network during the winter season. Next the observed deviations related to each external factor are approximated mathematically. The actual ageostrophic wind profile then becomes the sum of the mean and deviation profiles. The sign and magnitude of the deviations are defined as linear functions of parameters which are easily obtained from routine radiosonde and surface meteorological data. Once the ageostrophic winds are specified, the method for computing vertical motions in the PBL as outlined in Chapter 2 becomes a straight forward procedure.

### 8.1 Standard Profiles

Fig. 8.1 showed standard profiles of  $v'' / |\vec{V}_g|$  and  $u'' / |\vec{V}_g|$  for the lowest 2.5 km of the atmosphere. These profiles were obtained from the data for conditions of no thermal wind, uniform lapse rate in the lowest 1.5 km of approximately  $5^\circ\text{C}/\text{km}$ , and average speeds in the lowest km of 10 m/sec. The conversion 1 mb  $\approx$  10 m in the lower atmosphere has been used to express the height in meters instead of millibars above the surface. Both 00Z and 12Z data were used in

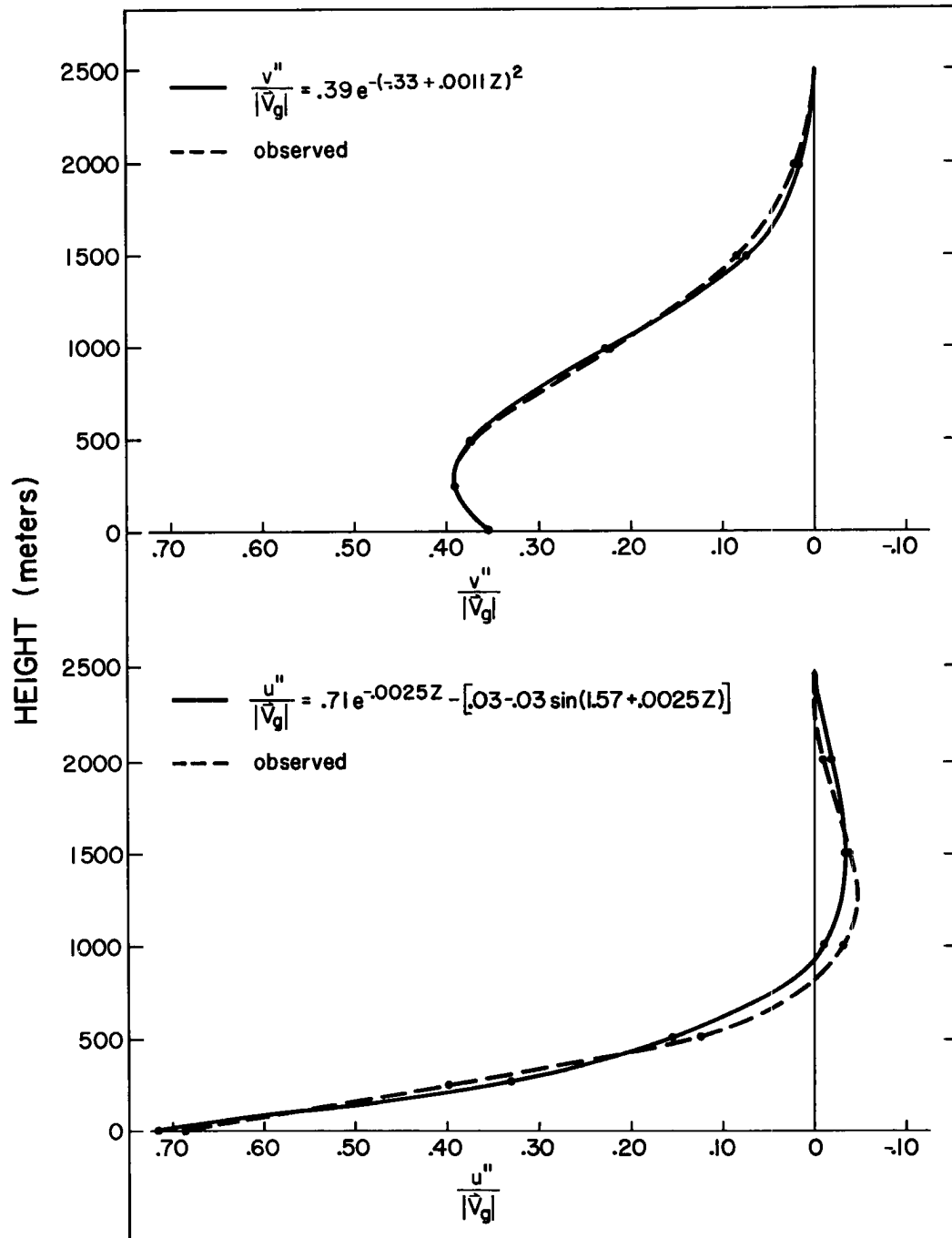


Fig. 8.1. Observed and model profiles of the normalized ageostrophic flow. The profiles are for barotropic conditions; uniform lapse rate of  $5^{\circ}\text{C}/\text{km}$  in the lowest kilometer; and an average speed in the lowest kilometer of  $10\text{ m/sec}$ .

constructing these profiles. Note that the maximum value of  $v'' / |\vec{V}_g|$  is at a height of about 300 m while the maximum  $u'' / |\vec{V}_g|$  occurs at the surface.

The shape of the  $v'' / |\vec{V}_g|$  curve is very close to a one dimensional probability density function of the form

$$v'' / |\vec{V}_g| = Ae^{-(a+bz)^2}, \quad (8.1)$$

where  $A$ ,  $a$ , and  $b$  are constants. At  $z = 300$  m, the equation is satisfied by setting  $A = .39$  and  $a+bz = 0$ . Substituting the observed value of  $v'' / |\vec{V}_g|$  for various values of  $z$  provides several values of  $a$  and  $b$ . When  $z$  is expressed in meters the values which give the best approximation to the curve are  $a = -.33$  and  $b = .0011$ . The empirical expression for the normalized cross-isobaric flow is therefore,

$$v'' / |\vec{V}_g| = .39e^{-(-.33+.0011z)^2}. \quad (8.2)$$

This model curve is also shown in Fig. 8.1. The maximum difference between the observed and model curves is only .01.

The curve for  $u'' / |\vec{V}_g|$  is more complicated, with the occurrence of both positive and negative values. This curve can be approximated by the combination of an exponential curve and a sin curve as follows:

$$u'' / \left| \vec{V}_g \right| = Ae^{-az} - [B - B \sin(b + cz)] \quad . \quad (8.3)$$

Experimentation gave the following relationship,

$$u'' / \left| \vec{V}_g \right| = .71e^{-.0025z} - [.03 - .03 \sin(1.57 + .0025z)] \quad . \quad (8.4)$$

The model curve for  $u'' / \left| \vec{V}_g \right|$  is given in Fig. 8.1. The maximum deviation between the observed and model curve is approximately .03.

## 8.2 Variations Related to Baroclinicity

Fig. 8.2 gives the observed deviations in the ageostrophic wind components existing in baroclinic conditions. These curves are based on the values given in Tables 4.3 and 4.4. The categories of the angle  $\beta$  which yield the maximum positive and negative deviations from the values for negligible thermal winds are shown.

The maximum and minimum values of the cross-isobaric wind component  $v'' / \left| \vec{V}_g \right|$  are associated with  $\beta \approx 270^\circ$  and  $\beta \approx 90^\circ$ , respectively. The deviations are maximum near the surface and decrease to negligible values above 1000 m. The shape of the curves for the deviations due to thermal winds (Dev. T. W.) again suggest a relationship of the form:

$$\text{Dev. T. W. } (v'' / \left| \vec{V}_g \right|) = A_T e^{-(a+bz)^2} \quad . \quad (8.5)$$

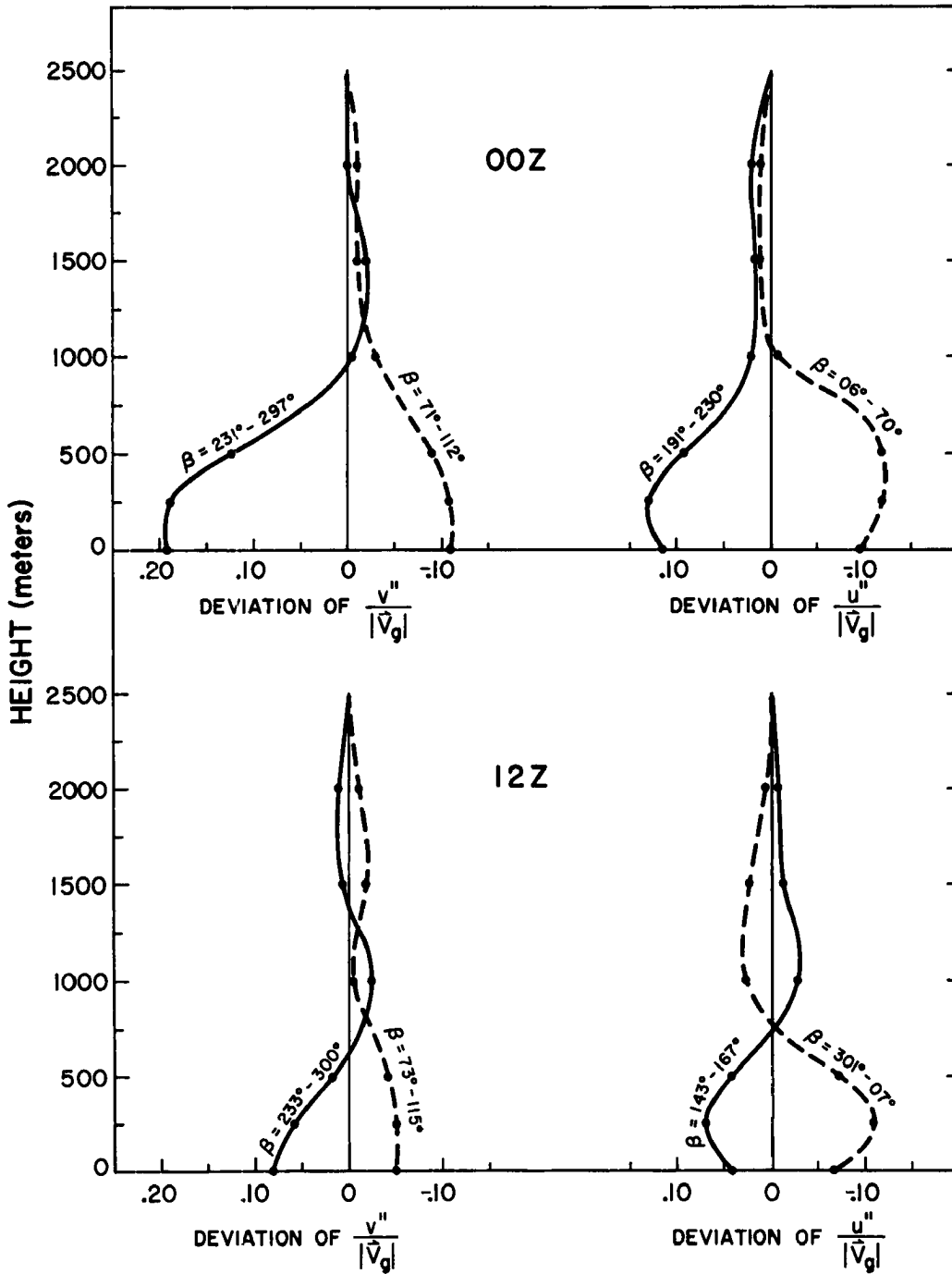


Fig. 8.2. Observed deviations of the normalized ageostrophic wind components related to baroclinicity.

The sign of the deviation is defined by the angle  $\beta$ . The observational results given in Chapter 4 suggests the magnitude is dependent on the stability and the relative magnitude of the thermal wind. Here we will use  $\theta_{1000\text{ m}} - \theta_o$  as the stability parameter and  $|\vec{V}_T|/S$  as a measure of the temperature gradient.

The average conditions at 00Z and 12Z for the values in Fig. 8.2 are given in Table 8.1. The amplitude  $A_T$  can then be approximated by the following expression:

$$A_T \approx .30 (|\vec{V}_T|/S) [1 - .07 (\theta_{1000\text{ m}} - \theta_o)] [\sin(\pi + \beta)]. \quad (8.6)$$

By letting the maximum amplitude exist at 100 m then decreasing to 1/10 of the maximum value at  $z=1000$  m we get the following empirical relationship for the deviation of  $v'' / |\vec{V}_g|$  due to baroclinicity,

---

Table 8.1

Average conditons associated with the observed deviation shown in Fig. 8.2.

Time	$\theta_{1000\text{ m}} - \theta_o$	$ \vec{V}_T /S$	$A_{\text{max}}$
00Z	$\approx 2^\circ\text{C}$	$\approx .5$	.15
12Z	$\approx 9^\circ\text{C}$	$\approx .5$	.06

---

$$\text{Dev. T. W. } (v'' / |\vec{V}_g|) = \left\{ .30 (|\vec{V}_T| / S) [1 - .07 (\theta_{1000 \text{ m}} - \theta_o)] \right. \\ \left. [\sin(\pi + \beta)] \right\} e^{-(-.17 + .0017z)^2}. \quad (8.7)$$

Fig. 8.2 also shows curves of the maximum deviation in the  $u'' / |\vec{V}_g|$  values. We expect the maximum positive and negative values with  $\beta \approx 0^\circ$  and  $\beta \approx 180^\circ$ , respectively. The values of  $\beta$  shown in Fig. 8.2 generally support this hypothesis though the maximum deviations are associated with somewhat different values of  $\beta$  at 12Z as opposed to 00Z.

The maximum deviations occur at 250 m then decrease rapidly with height. The deviations are negligible above 1000 m. The 12Z data shows a tendency for the sign of the deviations to switch between 500 m and 1000 m. However, this tendency is ignored in the development of an empirical relationship so that the distribution can again be modeled by an expression of the form:

$$\text{Dev. T. W. } (u'' / |\vec{V}_g|) = B_T e^{-(a+bz)^2}. \quad (8.8)$$

Assuming the maximum deviations occur for  $\beta = 0^\circ$  and  $180^\circ$  and following Eq. (8.6), the expression for  $B_T$  becomes:

$$B_T = .24 (|\vec{V}_T| / S) [1 - .07 (\theta_{1000 \text{ m}} - \theta_o)] (-\cos \beta). \quad (8.9)$$

Assuming further that the maximum deviation occurs at  $z = 250 \text{ m}$

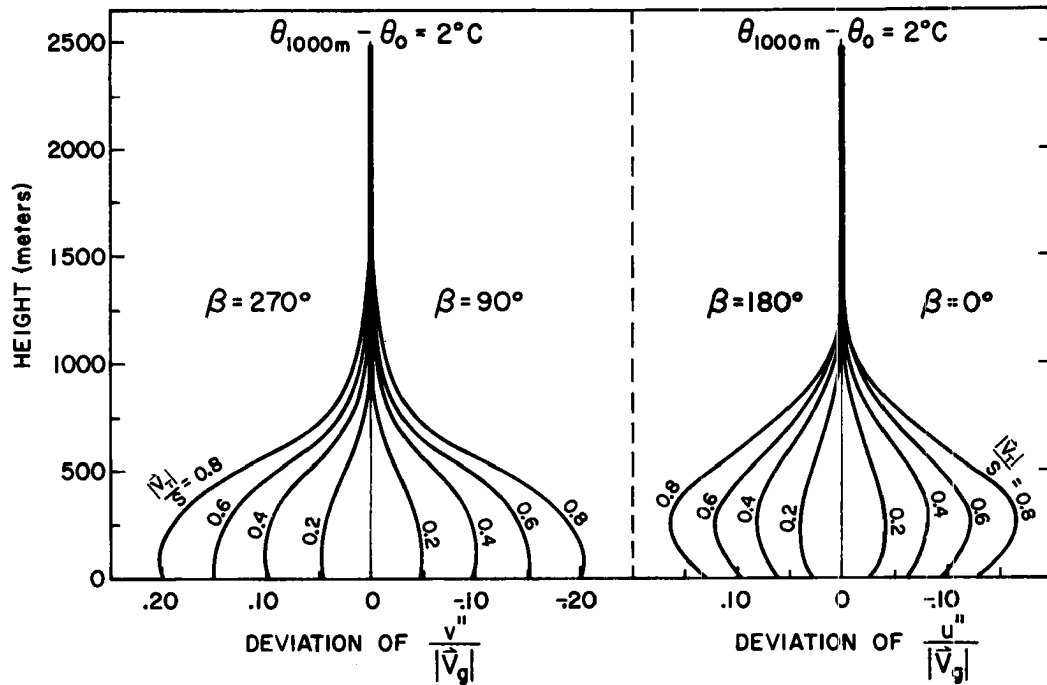


Fig. 8.3. Model profiles of the deviations of the normalized ageostrophic wind components due to baroclinicity.

then decreases to 1/10 of the maximum value at  $z \approx 1000$  m. The deviation of  $u'' / |\vec{V}_g|$  due to thermal wind effects becomes:

$$\text{Dev. T. W. } (u'' / |\vec{V}_g|) = \left\{ .24 (|\vec{V}_T| / S) [1 - .07 (\theta_{1000 \text{ m}} - \theta_0)] \right. \\ \left. (-\cos \beta) \right\} e^{-(-.51 + .0020z)^2}. \quad (8.10)$$

Model curves of the deviations due to baroclinicity as given by Eqs.

(8.7) and (8.10) are shown in Fig. 8.3 for selected values of  $\beta$ ,

$|\vec{V}_T| / S$ , and  $\theta_{1000 \text{ m}} - \theta_0$ .

### 8.3 Variations Related to Stability

General Variations. The observed deviations in the profiles of the normalized ageostrophic wind components due to systematic stability

differences are given in Fig. 8.4. The values were obtained from Tables 5.2 and 5.3. The deviations are differences between the moderate lapse rate values and the values for near adiabatic and very stable conditions, respectively. Fig. 8.4 gives the average of the differences at 00Z and 12Z.

The deviations of  $v'' / |\vec{V}_g|$  related to stability changes (Dev. Stability) can be modeled by a sin function of the form,

$$\text{Dev. Stability}(v'' / |\vec{V}_g|) = A_S + A_S [\sin(a+bz)]. \quad (8.11)$$

The amplitude  $A_S$  will be a function of stability. In Chapter 5 we saw that in cases of strong ground based inversions the profiles were similar regardless of the lapse rates above the inversions. For this reason we have made  $A_S$  a function of two lapse rate parameters. The first  $\theta_{2000\text{ m}} - \theta_o$  is a measure of the overall stability. The second  $\theta_{250\text{ m}} - \theta_o$  includes the effects of shallow ground based inversions. Utilizing the values of Fig. 8.4 the value of  $A_S$  can be modeled as follows:

$$A_S = .05 \left\{ 1 - [(\theta_{250\text{ m}} - \theta_o) \cdot 2] + [(\theta_{2000\text{ m}} - \theta_o) \cdot 1] \right\}. \quad (8.12)$$

For a uniform lapse rate of  $5^\circ\text{C}/1000\text{ m}$  the value of  $A_S$  becomes approximately zero.

Letting the maximum deviation occur at 1000 m and no deviation at 2500 m, Eq. (8.11) becomes:

$$\begin{aligned} \text{Dev. Stability } (v'' / |\vec{V}_g|) &= .05 \left\{ 1 - [(\theta_{250 \text{ m}} - \theta_o) \cdot 2] \right. \\ &\quad \left. + [(\theta_{2000 \text{ m}} - \theta_o) \cdot 1] \right\} \left\{ 1 + \sin(-.53 + .0021z) \right\} \quad . \quad (8.13) \end{aligned}$$

The deviation curves for  $u'' / |\vec{V}_g|$  in Fig. 8.4 are similar in form to the standard profile given in Fig. 8.1. Again we model the deviation as the sum of an exponential curve and a sin curve. The resulting approximation is:

$$\begin{aligned} \text{Dev. Stability } (u'' / |\vec{V}_g|) &= \left\{ 1 - [(\theta_{250 \text{ m}} - \theta_o) \cdot 2] + [(\theta_{2000 \text{ m}} - \theta_o) \cdot 1] \right\} \\ &\quad \left\{ .10e^{-.0015z} - [.02 + .02 \sin(-.53 + .0021z)] \right\} \quad . \quad (8.14) \end{aligned}$$

Model profiles of the deviations due to stability as given by Eqs. (8.13) and (8.14) are shown in Fig. 8.5.

Diurnal Variations. The difference between the winter 00Z and 12Z normalized ageostrophic wind components for the same lapse rates are given in Fig. 8.6. These differences arise from the existence of the inertial boundary layer (as discussed in Chapter 5) during a significant portion of the 12Z observations. Again the height distribution of the deviations due to diurnal oscillations (Dev. Diurnal) can be modeled by the one dimensional probability density function i.e.,

$$\text{Dev. Diurnal } (v'' / |\vec{V}_g|) = A_D e^{-(a+bz)^2} \quad (8.15)$$

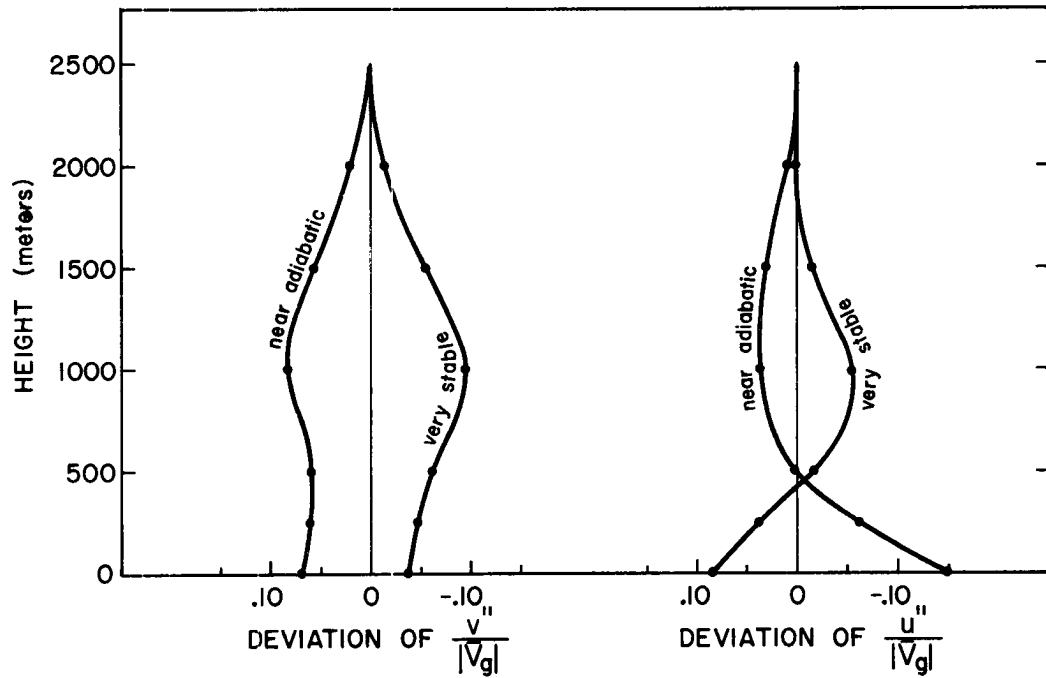


Fig. 8. 4. Observed deviations of the normalized ageostrophic wind components related to variations in the stability of the lowest 1500 m.

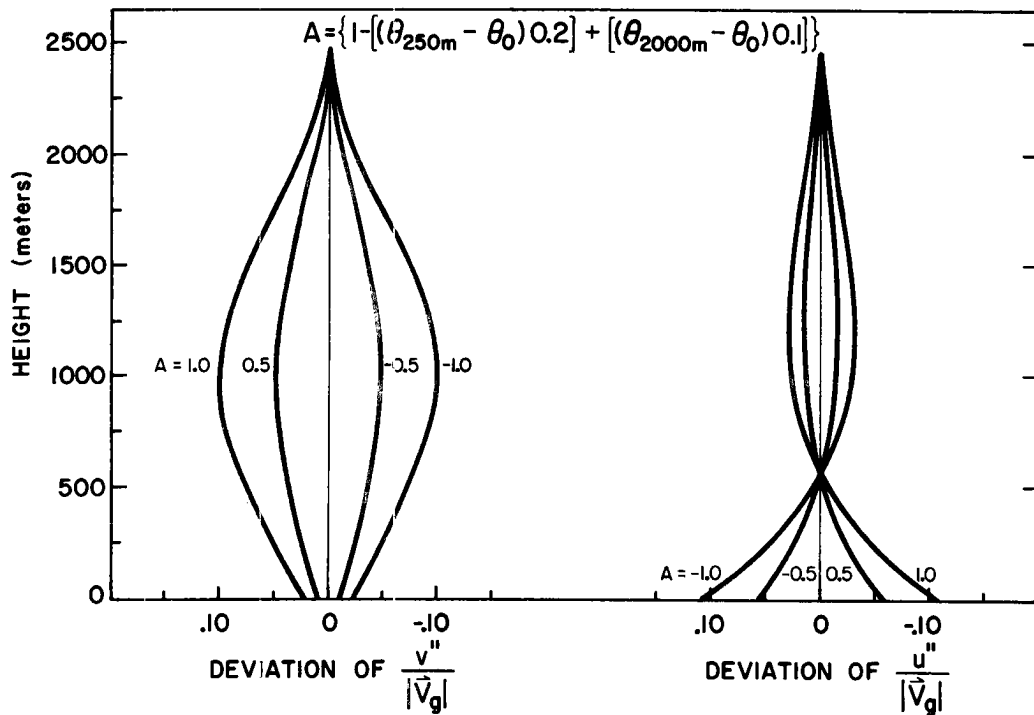


Fig. 8. 5. Model profiles of the deviations in the normalized ageostrophic wind components due to stability variations.

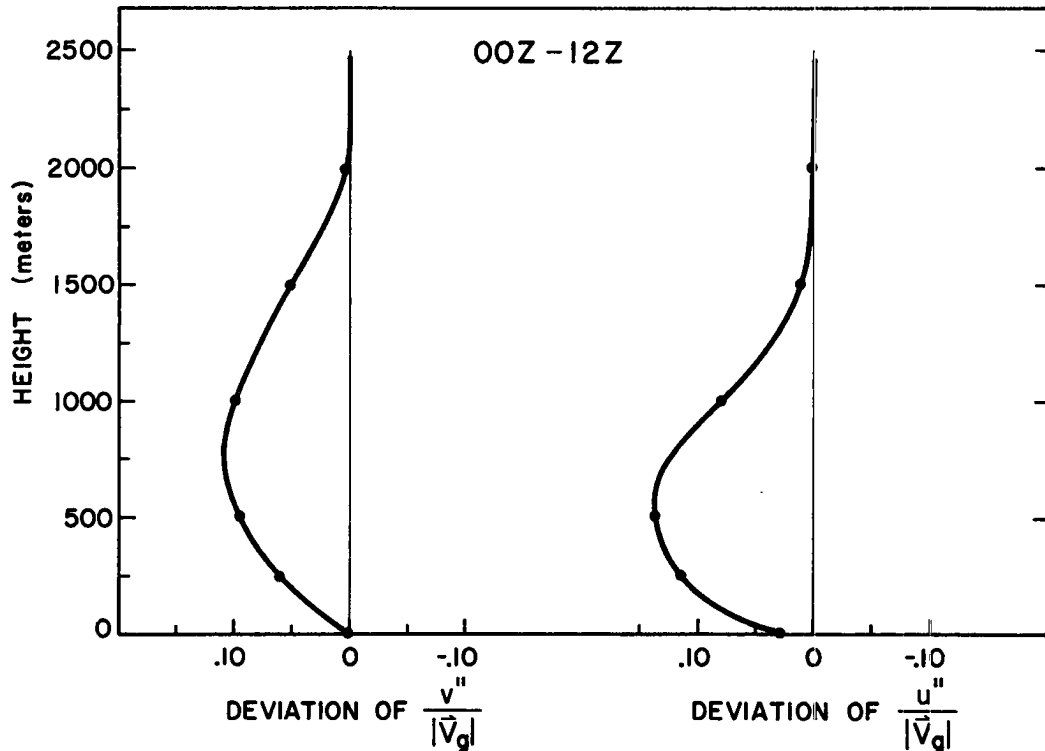


Fig. 8.6. Observed deviations of the normalized ageostrophic wind component attributed to inertial oscillations. The profiles are the difference between the 00Z values and 12Z values (00Z minus 12Z) for the same existing lapse rates.

$$\text{Dev. Diurnal} \left( \frac{u''}{|\vec{V}_g|} \right) = B_D e^{-(c+dz)^2} \quad (8.16)$$

As discussed in Chapter 5 the amplitude and phase of the inertial oscillation should be a function of:

- (1) time
- (2) latitude
- (3) the depth of the momentum boundary layer in the late afternoon
- (4) the rate of low level cooling after sunset.

The period of inertial motions depends only on the latitude which can be specified by the Coriolis parameter ( $f$ ). By defining a time scale ( $t'$ ) based on the elapsed time after the formation of the inertial boundary layer, the amplitudes become a sin function of the form:

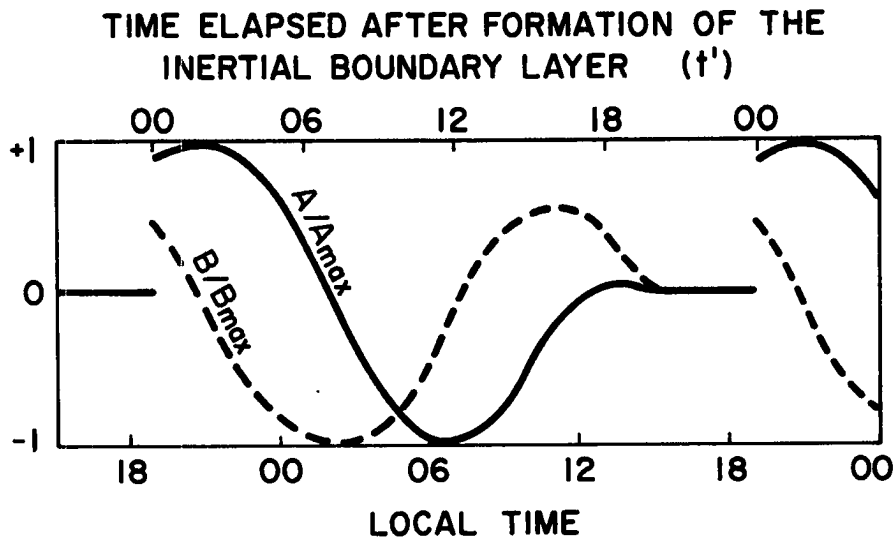


Fig. 8.7. Schematic diagram showing the ratio of the component amplitudes to their maximum amplitudes for inertial motion at  $35^{\circ}\text{N}$ .

$$A_D \propto \sin(e + ft')$$

$$B_D \propto \sin(m + ft')$$

where the phase is defined by the parameters  $e$  and  $m$ .

Following Fig. 5.17,  $t'$  equals zero at 1900 LT. The inertial motion are assumed to exist until 0900 LT ( $t' = 1400$ ). From 0900 - 1500 LT we assume the amplitudes decrease linearly to zero. This assumption is somewhat unrealistic in view of an earlier conclusion that the inertial boundary layer is eliminated from the lowest layers upward. From 1500-1900 LT the amplitudes are assumed to be zero.

Fig. 5.18 showed in schematic form the direction of the ageostrophic wind vector relative to the geostrophic wind vector at the time of the formation of the inertial layer. Fig. 8.7 shows the subsequent variation in the amplitudes at  $35^{\circ}\text{N}$  for these initial conditions. For

the initial orientation defined by Fig. 5.18,  $e = 1.04$  and  $m = 2.62$ . From Fig. 8.7 we conclude that the difference between 00Z and 12Z data in Fig. 8.6 are about 3/4 of the maximum differences that occur.

The depth of the momentum boundary layer during late afternoon is estimated by the parameter  $\Delta\theta$  where,

$$\Delta\theta = \theta_{2000\text{ m}} - \theta_0 \quad . \quad (8.17)$$

Equation (8.17) should be determined from conditions at approximately 1500 LT.

Similarly, the rate of low level cooling is estimated by the parameter  $\Delta T_0$  where,

$$\Delta T_0 = T_0(1500\text{ LT}) - T_0(2100\text{ LT}) \quad . \quad (8.18)$$

$T_0$  is the surface temperature. Average values for both  $\Delta\theta$  and  $\Delta T_0$  are near  $5^\circ\text{C}$ .

From Fig. 8.6, the maximum deviation of  $v'' / |\vec{V}_g|$  is .11 and the maximum deviation of  $u'' / |\vec{V}_g|$  is .14. For true inertial motions the maximum amplitudes should be identical. Averaging the two maximum deviation values and remembering the 3/4 factor obtained from Fig. 8.7 the amplitudes are approximated as follows:

$$\begin{aligned} 1900 - 0900\text{ LT} & \text{ --- } A_D = .15 \left[ 1 + \left( \frac{\Delta T - \Delta\theta}{5} \right) \right] [\sin(1.04 + ft')] \\ 0900 - 1500\text{ LT} & \text{ --- } A_D = .15 \left[ \frac{t' - 1400}{6} \right] \left[ 1 + \left( \frac{\Delta T - \Delta\theta}{5} \right) \right] [\sin(1.04 + ft')] \\ 1500 - 1900\text{ LT} & \text{ --- } A_D = 0 \quad . \quad (8.19) \end{aligned}$$

$$\begin{aligned}
1900 - 0900 \text{ LT} & \quad B_D = .15 \left[ 1 + \left( \frac{\Delta T - \Delta \theta}{5} \right) \right] [\sin (2.62 + ft')] \\
0900 - 1500 \text{ LT} & \quad B_D = .15 \left[ \frac{t' - 1400}{6} \right] \left[ 1 + \left( \frac{\Delta T - \Delta \theta}{5} \right) \right] [\sin (2.62 + ft')] \\
1500 - 1900 \text{ LT} & \quad B_D = 0 .
\end{aligned} \tag{8.20}$$

Letting the maximum deviation occur at a height of 700 m then decreasing to 1/10 this value at  $z = 1500$  m the deviation due to diurnal variations becomes:

$$\text{Dev. Diurnal}(v'' / |\vec{V}_g|) = A_D e^{-(-1.33 + .0019z)^2} \tag{8.21}$$

$$\text{Dev. Diurnal}(u'' / |\vec{V}_g|) = B_D e^{-(-1.33 + .0019z)^2} . \tag{8.22}$$

Model curves for  $35^\circ \text{N}$  as given by Eqs. (8.21) and (8.22) for  $\Delta T = \Delta \theta$  are shown in Fig. 8.8.

#### 8.4 Variations Related to Speed Changes

The deviations of the ageostrophic wind components from the values for  $S = 10$  m/sec are shown in Fig. 8.9. These deviations were obtained from the data in Tables 7.3 and 7.4.

Here strong speeds  $S > 10$  m/sec produce positive deviations for the  $v'' / |\vec{V}_g|$  values but negative deviation values for  $u'' / |\vec{V}_g|$ . Again, the deviation due to speed variations (Dev. Speed) are approximated by a relationship of the form:

$$\text{Dev. Speed}(v'' / |\vec{V}_g|) = A_V e^{-(a+bz)^2} \tag{8.23}$$

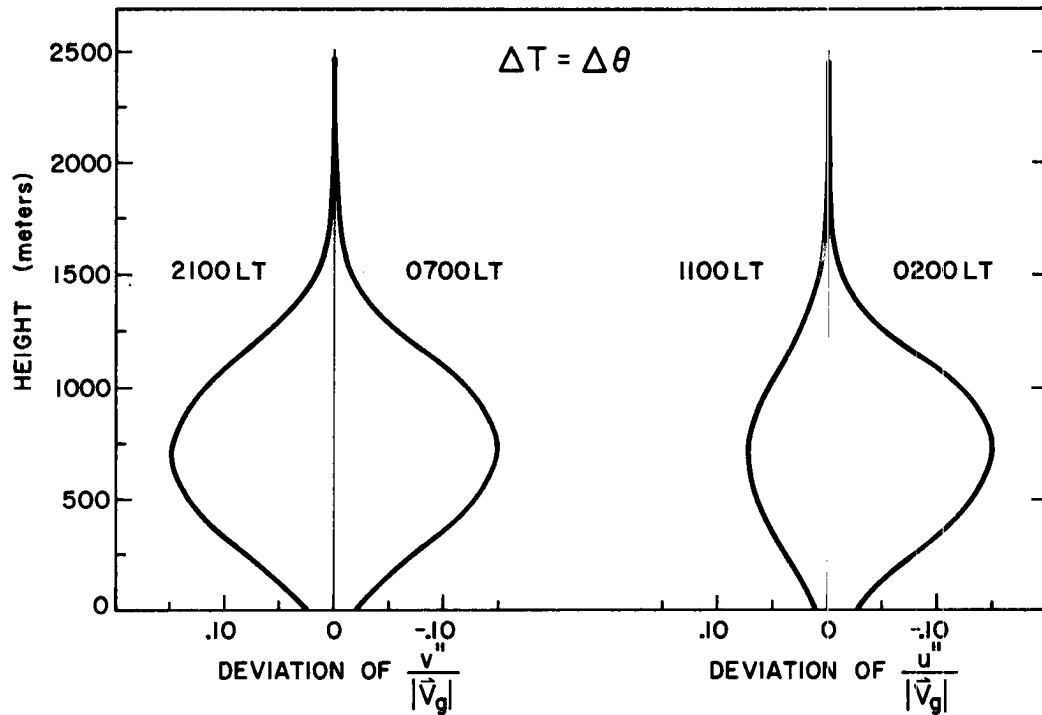


Fig. 8.8. Model profiles of the deviations in the normalized ageostrophic wind components arising from the formation of an inertial boundary layer at 1900 LT.

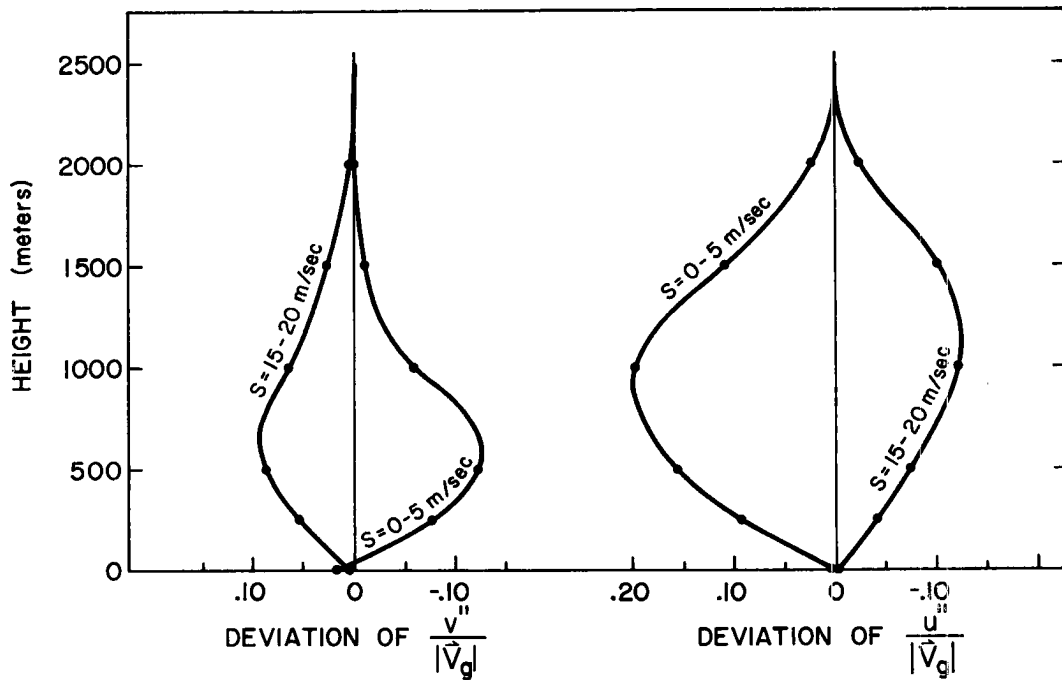


Fig. 8.9. Observed deviations in the normalized ageostrophic wind components related to variations in the average speed in the lowest kilometer.

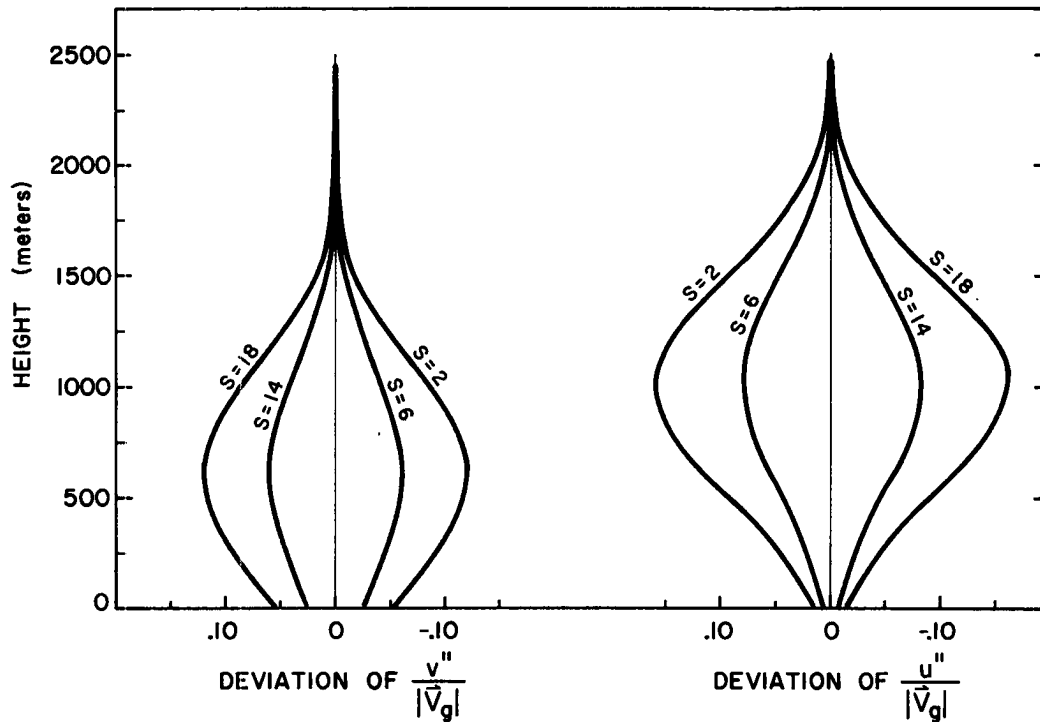


Fig. 8.10. Model profiles of the deviation in normalized ageostrophic wind components related to variations in the average speed in the lowest kilometer.

$$\text{Dev. Speed}(u'' / |\vec{V}_g|) = B_V e^{-(c+dz)^2} . \quad (8.24)$$

The amplitudes  $A_V$  and  $B_V$  are assumed to be only a function of the variable  $S$ . For the  $v'' / |\vec{V}_g|$  deviation the maximum amplitude is approximated by,

$$A_V = \left( \frac{S}{10} - 1.0 \right) .15 . \quad (8.25)$$

Letting the maximum amplitude occur at  $z = 600$  m decreasing to  $1/10$  of this value at  $z=1600$  m the model expression for the speed deviations in  $v'' / |\vec{V}_g|$  becomes:

$$\text{Dev. Speed}(v'' / |\vec{V}_g|) = [.15 (\frac{S}{10} - 1.0)] [e^{-(-.90 + .0015z)^2}] \quad (8.26)$$

Likewise, the maximum value of  $B_V$  can be approximated by

$$B_V = (1.0 - \frac{S}{10}) .20 \quad (8.27)$$

If the maximum deviation in  $u'' / |\vec{V}_g|$  occurs at  $z=1000$  m and decreases to 1/10 the maximum value at  $z = 2000$  m, the deviations of  $u'' / |\vec{V}_g|$  can be approximated as

$$\text{Dev. Speed}(u'' / |\vec{V}_g|) = [.20 (1 - \frac{S}{10})] [e^{-(-1.50 + .0015z)^2}] \quad (8.28)$$

Model curves of the deviation as given by Eqs. (8.26) and (8.28) are given in Fig. 8.10.

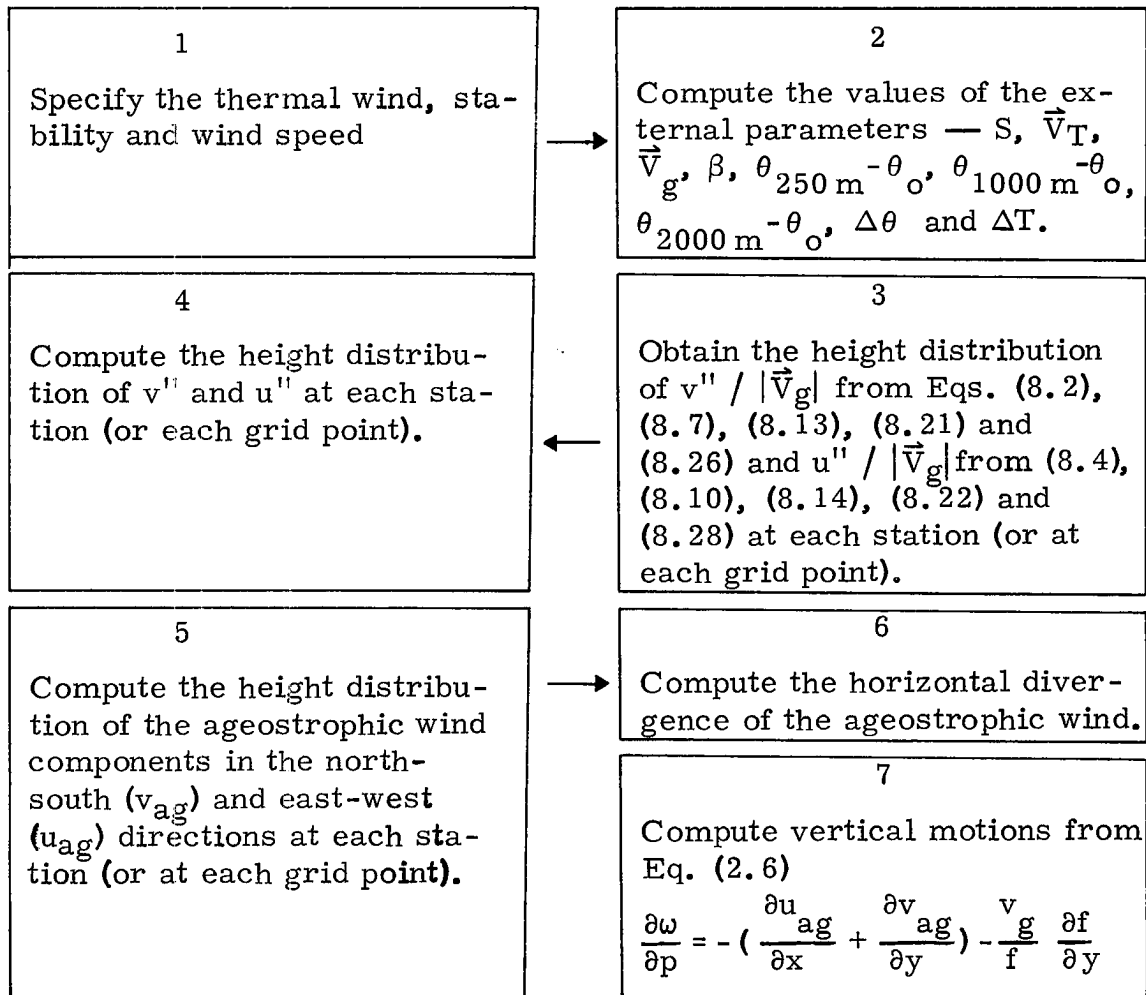
### 8.5 Method for Computing Vertical Motion

The ageostrophic flow (excluding variations in surface roughness, non steady effects and orography) is obtained by adding the deviation profiles to the mean profiles. Thus, the profile of  $v'' / |\vec{V}_g|$  is given by the sum of the right hand side of Eqs. (8.2), (8.7), (8.13), (8.21) and (8.26). Similarly the profile of  $u'' / |\vec{V}_g|$  is given by the sum of Eqs. (8.4), (8.10), (8.14), (8.22) and (8.28).

The list of external parameters includes —  $S$ ,  $\vec{V}_T$ ,  $\beta$ ,  $\theta_{250 \text{ m}} - \theta_o$ ,  $\theta_{1000 \text{ m}} - \theta_o$ ,  $\theta_{2000 \text{ m}} - \theta_o$ ,  $\vec{V}_g$ ,  $\Delta\theta$  and  $\Delta T_o$ . All of these except  $\Delta\theta$  and  $\Delta T$  can be obtained directly from a network of

concurrent radiosonde observations. For diagnostic purposes, the value of  $\Delta\theta$  and  $\Delta T$  can be specified by the latest conditions at 1500 and 2100 LT. Moreover, for prediction purposes all of the external parameters can be specified by existing numerical models.

As indicated in Chapter 2, vertical motion results primarily from the divergence of the ageostrophic wind. We now have an operational method for specifying the ageostrophic wind in the lowest 2.5 km for a wide range of synoptic conditions. The procedures for obtaining the vertical motion at any point in the lowest 2.5 km are presented below in schematic form.



This method of computing vertical motion accounts for much of the variability in planetary boundary layer wind profiles. This or similar methods should be considered by the National Meteorological Center as a possible tool in obtaining more accurate initial, as well as predicted, vertical motion fields.

## 9. SUMMARY

### 9.1 Review

Extensive analyses of conventional rawinsonde and windsonde data have been performed. Selective stratification of these data, for the lowest 2.5 - 3 km of the atmosphere, has revealed the dependence of the PBL wind profiles on variations in baroclinicity, stability and wind speed. Conclusions concerning the physical processes associated with these variations have been made within each chapter. The impact of these variations on several fundamental atmospheric processes has been examined. An empirical model of the height distribution of the ageostrophic wind was developed and a new method for computing vertical motions was outlined.

### 9.2 Results and Conclusions

Role of Baroclinicity. Over the eastern U. S. during winter, the quantity  $|\vec{V}_T|/S$  is greater than 0.2 approximately 83% of the time. Here  $\vec{V}_T$  is the thermal wind vector in the lowest 100 mb of the atmosphere while  $S$  is the average speed in the lowest 100 mb. Barotropic theories for the height distribution of winds in the planetary boundary layer are therefore invalid in a majority of conditions.

In baroclinic conditions, the angle between the wind and isobars; the ageostrophic wind components; the surface stress and the surface wind speed are all functions of the orientation of the thermal wind vector relative to the surface geostrophic wind. (All of these quantities

reach their maximum values in conditions with cold air advection.) These variations are consistent with a mixing length model of turbulent momentum transport. The geostrophic shear existing in baroclinic conditions modifies the turbulent transport of horizontal momentum from that which would exist in barotropic conditions. The magnitude and sign of the deviation in the planetary boundary layer wind profile therefore depends on the direction and magnitude of the thermal wind relative to the direction and magnitude of the surface geostrophic wind.

The magnitudes of the observed deviation over the U. S., during winter, suggest that as much as 50% of the westerly angular momentum which is transferred from the atmosphere to the earth in mid-latitudes, reaches the surface through downward turbulent transport maintained by geostrophic shears.

Role of Stability Changes. The thermal stratification of the lowest kilometer influences the mean wind profile by controlling the height distribution of turbulent momentum transfer. In general, increasing the stability results in the following adjustments in the wind profiles:

- (1) decreased depth of the PBL
- (2) greater angles between the surface wind and surface isobars
- (3) smaller values of the ageostrophic wind towards lower pressure
- (4) increased vertical shears of the horizontal wind
- (5) smaller values of the ratio  $|\vec{V}_o| / |\vec{V}_{go}|$ .

Diurnal changes in the lapse rates for the lowest 2 km under basically clear conditions, typically leads to: an order of magnitude variation in the depth of the momentum or Ekman boundary layer, and

the formation of an inertial boundary layer above 200-300 m shortly after sunset. Through the night and morning hours the PBL is made up of the momentum and inertial boundary layers. The motions in the inertial boundary layer amplify the daily variations in the PBL wind profiles. This eliminates the feasibility of parameterizing the winds in terms of the existing lapse rates. Only in the afternoon hours when the inertial boundary layer is destroyed by turbulent mixing does a balance exist among the Coriolis, pressure gradient and frictional forces. The geostrophic departure method for computing surface stress is likewise valid for the afternoon hours only.

The existence of an inertial boundary layer in the night and morning hours also amplifies the diurnal variations of both the total kinetic energy generation and the total kinetic energy in the lowest 2.5 - 3 km of the atmosphere. At  $32.5^{\circ}\text{N}$ , the maximum and minimum generation values are observed near 2100 and 0700 LT. The maximum and minimum total kinetic energy is observed near 0200 and 1500 LT. The dissipation of kinetic energy by turbulent scale processes reach a maximum in mid-afternoon and a minimum during the later night hours.

The magnitude of the changes in kinetic energy are comparable to the magnitudes of the total generation and dissipation for much of the day. This means the often employed assumption of the kinetic energy generation being equal to the magnitude of the dissipation is not valid.

Role of Speed Variations. Increasing the average speed in the lowest 100 mb ( $\approx 1$  km) produces no significant changes in the angle

between the surface wind and surface isobars. However, as the speed increases, significant changes are observed in the magnitude of the ageostrophic wind components, especially in the layer 25-150 mb above the surface. In this layer, the normalized ageostrophic wind component towards lower pressure increases with increasing speed, while the level of maximum cross-isobaric flow increases. This implies that the level of maximum eddy diffusivity increases, with increasing speed, leading to changes in the characteristics of the stress profile.

### 9.3 Extension of the Present Work

The variation related to two external factors neglected in this analysis, namely surface roughness and horizontal accelerations, should be specified. Modifying the empirical relationships obtained in Chapter 8 for geographical variations in surface roughness appears feasible by the addition of an extra variable to each relationship. An estimate of the form of this variable could be obtained from already existing studies.

The major deficiency of the empirical models developed in Chapter 8 is the absence of any relation specifying the ageostrophic winds resulting from horizontal accelerations. It seems reasonable to hypothesize that vertical gradients in the horizontal acceleration will modify stress profiles in a manner analogous to the geostrophic shear. That is, the modification will be a function of the orientation as well as the magnitude of the vertical shear of the ageostrophic wind vector resulting from horizontal accelerations. Therefore, the ageostrophic

winds resulting from non steady flow cannot simply be added to the ageostrophic flow that would exist in a steady state flow. The resolution and accuracies of wind data from a conventional radiosonde network are not sufficient to specify vertical gradients in the horizontal accelerations. At present, the best research methodology for confirming the above hypothesis appears to be numerical modeling studies like those conducted by Benton et al. (1964) and Mak (1972).

## ACKNOWLEDGEMENTS

The author gratefully acknowledges the guidance and encouragement of Dr. William M. Gray who served as his advisor during the course of this research. Special thanks are also expressed to Drs. Alan K. Betts, Elmar R. Reiter and Virgil A. Sandborn for their review of the manuscript and helpful suggestions.

The efforts of several members of the Department of Atmospheric Science staff are sincerely appreciated. Mr. Edward Buzzell did most of the programming work; Mr. Larry Kovacic drafted the many figures; Mrs. Cheryl Brown aided in the data reduction; Mrs. Beryl Younkin helped in typing the manuscript; and Mrs. Barbara Brumit helped considerably in both the data reduction and typing of the manuscript.

This research was supported by the National Science Foundation under Grant GA-32589 X 1.

## BIBLIOGRAPHY

- Åkerblom, F. A., 1908: Recherches sur les courants les plus bas de l'atmosphère au-dessus de Paris. Societas Scientiarum Upsaliensis, Nova Acta, Ser. VI, 2 (2).
- Benton, G. S., F. B. Lipps and Shih-Yu Tuann, 1964: Structure of the Ekman layer for geostrophic flows with lateral shear. Tellus, 16 (2), 186-199.
- Bernstein, A. B., 1959: The effect of a horizontal temperature gradient on the surface wind. M. S. Thesis, Penn. State Univ.
- Blackadar, A. K., 1957: Boundary layer wind maxima and their significance for the growth of nocturnal inversions. Bull. Amer. Meteor. Soc., 38 (5), 283-290.
- \_\_\_\_\_, 1962: The vertical distribution of wind and turbulent exchange in a neutral atmosphere. J. Geophys. Res. 67 (8), 3095-3102.
- \_\_\_\_\_, 1965: A single layer theory of the vertical distribution of wind in a baroclinic neutral atmospheric boundary layer. AFCRL 65-531, Final Report Contract No. AF(604)-6641, Penn. State Univ., 1-22.
- \_\_\_\_\_, and K. Buajitti, 1957: Theoretical studies of diurnal wind variations in the planetary boundary layer. Quart. J. Roy. Meteor. Soc., 83, 486-500.
- Bonner, W. D., and J. Paegle, 1970: Diurnal variations in boundary layer winds over the south-central United States in summer. Mon. Wea. Rev., 98 (10), 735-744.
- Cattle, H., 1971: The terrestrial low latitude boundary layer. Ph.D. Dissertation, Dept. of Meteor., Imperial College of Science and Tech., 201 p.
- Charney, J. G., and A. Eliassen, 1949: A numerical method for predicting the perturbations in the middle latitude westerlies. Tellus, 1, 38-54.
- \_\_\_\_\_, 1964: On the growth of the hurricane depression. J. Atmos. Sci., 21 (1), 68-75.

## BIBLIOGRAPHY (cont'd)

- Charnock, H., and T. H. Ellison, 1967: The boundary layer in relation to large-scale motions of the atmosphere and ocean. GARP, Report of Study Conference, Stockholm, Sweden, June 28-July 11.
- Ching, J. K. S., 1964: A theory of wind distribution in a single-layered diabatic baroclinic turbulent boundary layer of the atmosphere. M. S. Thesis, Penn. State Univ. 65 pp.
- Clark, R. H., 1970: Observational studies in the atmospheric boundary layer. Quart. J. Roy. Meteor. Soc., 96, 91-114.
- Deardorff, J. W., 1972: Numerical investigation of neutral and unstable planetary boundary layers. J. Atmos. Sci., 29 (1), 91-115.
- Dobson, G. M. B., 1914: Pilot balloon ascents at the central flying school, Upavan during the year 1913, Quart. J. Roy. Meteor. Soc., 40, 123-135.
- Ekman, V. W., 1905: On the influence of the earth's rotation on ocean currents. Arkiv för Matematik, Astronomi och Fysik, 2 (11), 1-52.
- Ellison, T. H., 1956: Atmospheric turbulence. Survey in Mechanics, G. I. Taylor Anniversary Vol., Cambridge Univ. Press, 400-430.
- Findlater, J., T.N.S. Harrower, G. A. Hawkins, and H. L. Wright, 1966: Surface and 900 mb wind relationships. Sci. Paper No. 23, Meteor. Office, London, 41 p.
- Fritsch, J. M., 1969: Objective analysis of a two dimensional data field by the cubic spline technique. Mon. Wea. Rev. 99 (5), 379-386.
- Gordon, A. H., 1952: Angle of deviation between the winds at 50 ft. and 2000 ft. over the North Atlantic ocean. The Meteor. Mag., 81, 59 p.
- Gray, W. M., 1968: Global view of the origin of tropical disturbances and storms. Mon. Wea. Rev., 96 (10), 669-700.
- \_\_\_\_\_, 1972: A diagnostic study of the planetary boundary layer over the oceans. Atmos. Sci. Paper No. 179, Dept. of Atmos. Sci., Colo. State Univ., Ft. Collins, Colo., 95 p.

## BIBLIOGRAPHY (cont'd)

- Holopainen, E. O., 1963: On the dissipation of kinetic energy in the atmosphere. Tellus, 15 (1), 26-32.
- Holton, J. R., 1967: Diurnal boundary layer wind oscillation above sloping terrain. Tellus, 19 (2), 199-205.
- Hsueh, Y., 1970: A note on the boundary layer wind structure above sloping terrain. J. Atmos. Sci., 27 (2), 322-327.
- Jeffries, H., 1920: On the relation between wind and distribution of pressure. Proc. Roy. Soc. London, A, 96, 233-249.
- Jehn, K. H., and S. J. Durie, 1963: Boundary layer wind maxima and associated temperature distributions as observed on the 1400 ft. television tower near Dallas, Texas, 1961-1962. AFCRL 63-738, Elect. Eng. Res. Lab., Univ. of Texas.
- Kovetz, A., J. Neumann and R. Suzi, 1963: Extension of Ekman's spiral to conditions of near-neutral static stability and a constant horizontal temperature gradient. Beitr. Phys. Atmos., 36 (3/4), 201-212.
- Krishna, K., 1968: A numerical study of the diurnal variation of meteorological parameters in the planetary boundary layer. I., Diurnal variations of winds. Mon. Wea. Rev. 96 (5), 269-276.
- Kung, E. C., 1967: Diurnal and long-term variations of the kinetic energy generation and dissipation for a five-year period. Mon. Wea. Rev., 95 (9), 593-606.
- \_\_\_\_\_, 1969: Further study on the kinetic energy balance. Mon. Wea. Rev., 97 (8), 573-581.
- Kurosaki, A., 1968: Numerical calculation of the structure of Ekman boundary layer. Presented at the WMO/IUGG Symposium on Numerical Weather Prediction, Tokyo, Japan.
- Lettau, H., 1950: A re-examination of the "Leipzig wind profile" considering some relations between wind and turbulence in the friction layer. Tellus, 2, 125-129.
- \_\_\_\_\_, 1957: Windprofil, innere Reibung and Energieumsatz in den unteren 500 m über dem Meer. Beitr. Phys. Atmos., 30, 78-96.

## BIBLIOGRAPHY (cont'd)

- Lettau, H., 1962: Theoretical wind spirals in the boundary layer of a barotropic atmosphere. Beitr. Phys. Atmos., 35 (3/4), 195-212.
- \_\_\_\_\_, 1964: Preliminary note on the effect of terrain-slope on low-level jets and thermal winds in the planetary boundary layer. Studies of the Effects of Variations in the Boundary Conditions on the Atmospheric Boundary Layer, Annual Rept., Dept. Meteor., Univ. Wisconsin, 99-115.
- \_\_\_\_\_, 1967: Small to large-scale features of boundary layer structure over mountain slopes. Proc. of the Symposium on Mountain Meteor., E. R. Reiter and J. L. Rasmussen, eds., Atmos. Sci. Paper No. 122, Dept. Atmos. Sci., Colo. State Univ., Ft. Collins, Colo., 1-74.
- \_\_\_\_\_, and W. F. Dabberdt., 1970: Variangular wind spirals. Boundary-Layer Meteor., 1 (1), 64-79.
- MacKay, K. P., 1971: Steady state hodographs in a baroclinic boundary layer. Boundary-Layer Meteor., 1 (2), 161-168.
- Mak, Man-Kin, 1972: Steady, neutral planetary boundary layer forced by a horizontally non-uniform flow. J. Atmos. Sci., 29 (4), 707-717.
- Mendenhall, B. R., 1967: A statistical study of the frictional wind veering in the planetary boundary layer. Atmos. Sci., Paper No. 116, Colo. State Univ., Ft. Collins, Colo.
- Ooyama, K., 1964: A dynamic model for the study of tropical cyclone development. Geof. Intern., 4, 187-198.
- Priestley, C. H. B., 1967: Handover in scale of the fluxes of momentum, heat, etc. in the atmospheric boundary layer. Physics of Fluids, 10 (9) pt. 2, S38-S46.
- Sangster, W. E., 1967: Diurnal surface geostrophic wind variations over the Great Plains. ESSA, Central Region, Tech. Memo. 13, Kansas City, Mo., 11p.
- Sheppard, P. A. and H. H. Omar, 1952: The wind stress over the ocean from observations in the trades. Quart. J. Roy. Meteor. Soc., 78, 583-589.

## BIBLIOGRAPHY (cont'd)

- Sheppard, P. A., H. Charnock and J. R. D. Francis, 1952: Observations of the westerlies over the sea. Quart. J. Roy. Meteor. Soc., 78, 563-582.
- Taylor, G. I., 1915: Eddy motion in the atmosphere. Phil. Trans. Roy. Soc. London, A., 215, 1-26.
- Trout, D. and H. A. Panofsky, 1969: Energy dissipation near the tropopause. Tellus, 21 (3), 355-358.
- United States Navy, 1966: Components of the 1000 mb winds (or surface winds) of the Northern Hemisphere. NAVAIR 50-1C-51 (For sale by the Superintendent of Documents, U. S. Gov. Printing Office, Washington, D. C.).
- Utina, Z. M., 1962: Effect of horizontal temperature inhomogeneity on the structure of the boundary layer of the atmosphere. Glavn. Geofiz. Observ., Trudy, No. 127, 134-144.
- \_\_\_\_\_, 1966: Wind distribution in the boundary layer. Glavn. Geofiz. Observ., Trudy No. 187, 146-148.
- Williams, K. T., 1970: A statistical analysis of satellite-observed trade wind cloud clusters in the western north Pacific. Atmos. Sci. Paper No. 161, Dept. Atmos. Sci., Colo. State Univ., Ft. Collins, Colo.
- Yamamoto, G., N. Yasuda and A. Shimanuki, 1968: Effect of thermal stratification on the Ekman layer. J. of the Meteor. Soc. of Japan, 46 (6), 442-455.
- Zaitsev, A. S., 1966: Effects of non-homogeneity of temperature on the wind field in the boundary layer. Glavn. Geofiz. Observ., Trudy, No. 187, 139-145.



<b>BIBLIOGRAPHIC DATA SHEET</b>	1. Report No. CSU-ATSP-199	2.	3. Recipient's Accession No.
4. Title and Subtitle  VARIABILITY OF PLANETARY BOUNDARY LAYER WINDS		5. Report Date March, 1973	6.
		7. Author(s) Lee Ray Hoxit	
9. Performing Organization Name and Address  Atmospheric Science Department Colorado State University Fort Collins, Colorado 80521		10. Project/Task/Work Unit No.	
		11. Contract/Grant No. NSF GA-32589 x 1	
12. Sponsoring Organization Name and Address  National Science Foundation Washington, D. C. 20550		13. Type of Report & Period Covered Project Report	
		14.	
15. Supplementary Notes			
16. Abstracts  Systematic stratifications and analyses of low level radiosonde and windsonde data are performed for portions of the eastern half of the United States. Changes in the planetary boundary layer wind profiles resulting from variations in baroclinicity, stability and speed are specified. Interpretations and conclusions concerning the physical processes responsible for the observed variations are presented. An empirical model of the height distribution of the ageostrophic wind is developed for the lowest 2.5 km of the atmosphere.			
17. Key Words and Document Analysis. 17a. Descriptors  Planetary Boundary Layer Winds Turbulence Diurnal Variations Vertical Motions  17b. Identifiers/Open-Ended Terms  17c. COSATI Field/Group			
18. Availability Statement		19. Security Class (This Report) UNCLASSIFIED	21. No. of Pages 157
		20. Security Class (This Page) UNCLASSIFIED	22. Price

